IVW - Schriftenreihe Band 166
Leibniz-Institut für Verbundwerkstoffe GmbH Kaiserslautern

Munehiro Chijiiwa

Experimental investigation and numerical modeling of time dependency of contact angle on laser micro-structured stainless steel

Bibliografische Information Der Deutschen Bibliothek

Die Deutsche Bibliothek verzeichnet diese Publikation in der Deutschen Nationalbibliografie; detaillierte bibliografische Daten sind im Internet über <http://dnb.dnb.de> abrufbar.

Bibliographic information published by Die Deutsche Bibliothek

Die Deutsche Bibliothek lists this publication in the Deutsche Nationalbibliografie; detailed bibliographic data is available in the Internet at <http://dnb.dnb.de>.

Herausgeber: Leibniz-Institut für Verbundwerkstoffe GmbH
Prof. Dr.-Ing. Ulf Breuer
Erwin-Schrödinger-Straße 58
67663 Kaiserslautern
http://www.ivw.uni-kl.de

Verlag: Leibniz-Institut für Verbundwerkstoffe GmbH

Druck: pri-me Printservice & Medienservice
Barbarossastraße 1
67655 Kaiserslautern
D-386

© Leibniz-Institut für Verbundwerkstoffe GmbH, Kaiserslautern 2025

Alle Rechte vorbehalten, auch das des auszugsweisen Nachdrucks, der auszugsweisen oder vollständigen Wiedergabe (Photographie, Mikroskopie), der Speicherung in Datenverarbeitungsanlagen und das der Übersetzung.

Als Manuskript gedruckt. Printed in Germany.
ISSN 1615-021X
ISBN: 978-3-944440-63-7

Experimental investigation and numerical modeling of time dependency of contact angle on laser micro-structured stainless steel

Vom Fachbereich Maschinenbau und Verfahrenstechnik
der Rheinland-Pfälzischen Technischen Universität Kaiserslautern-Landau
zur Erlangung des akademischen Grades

Doktor-Ingenieur (Dr.-Ing.)
genehmigte
Dissertation

von
Herrn
MSc.-Ing. Munehiro Chijiiwa
aus Kagoshima

Datum der wissenschaftlichen Aussprache 22.04.2024
Prüfungsvorsitzender: Prof. Dr.-Ing. Paul Ludwig Geiß
1. Berichterstatter: Prof. Dr.-Ing. Peter Mitschang
2. Berichterstatter: Dr.habil. J.A. L'huilier

D-386

Contents

Kurzfassung iii

Abstract v

List of Abbreviations vii

1 Introduction 1

2 Theory and Modeling 3

2.1 Laser micro-structure . . . 3

2.1.1 Basic of Laser process . . . 3

2.1.2 Basic of surface morphology . . . 7

2.1.3 State of the art: Mechanism for growth of sponge-like structure 10

2.2 Basic theory for CA . . . 13

2.3 State of the art and challenge . . . 17

2.4 The model for time dependency: developed in this work . . . 22

2.4.1 The model for relationships between CA and multiple chemical components . . . 22

2.4.2 The model for analysis of time development . . . 29

3 Experimental setup and techniques 31

3.1 Material . . . 31

3.2 Experimental setup for laser micro-structuring . . . 31

3.3 Post-process and Storage conditions . . . 32

3.4 Characterization of physical properties . . . 33

3.4.1 SEM . . . 33

3.4.2 Confocal microscope . . . 34

3.4.3 Cross-section image . . . 36

3.5 Characterization of surface chemistry . . . 37

3.5.1 XPS . . . 37

3.6 Characterization of wettability . . . 39

3.6.1 Contact angle 39

4 Physical properties by USP laser processing 41
4.1 Experiment 42
4.2 Results and discussion 42
4.3 Conclusion 48

5 Chemical properties by USP laser processing 49
5.1 The chemical effect immediate after laser processing 49
5.1.1 Experiments 50
5.1.2 Results and discussion 52
5.2 The chemical effect for long term 60
5.2.1 Experiment 60
5.2.2 Results and discussion 60
5.3 Conclusion 68

6 Application example 69
6.1 The effect of wettability on controlling friction 69
6.1.1 Experiments 70
6.1.2 Results and discussion 73
6.2 The effect of sponge-like structure on joining 74
6.2.1 Experiment 76
6.2.2 Results and Discussion 80

7 Conclusion and Outlook 83

8 Appendix 87

Bibliography 91

Publication and conference contribution 101

Curriculum Vitae 105

Kurzfassung

Bei der Oberflächenfunktionalisierung wird einer Oberfläche durch eine physikalische oder chemische Behandlung eine Funktionalität (Änderung der Benetzbarkeit, Änderung der Reibung) verliehen. In den letzten Jahren hat die Oberflächenfunktionalisierung durch Lasermikrostrukturierung in vielen Anwendungen an Bedeutung gewonnen. Eines der großen Probleme der laser-mikrostrukturierten Oberfläche von Edelstahl ist beispielsweise die Langzeitstabilität der Benetzbarkeit. Diese lässt sich durch den Kontaktwinkel (CA) der Flüssigkeit auf der Oberfläche nach der Lasermikrostrukturierung beschreiben. Der CA auf der mikrostrukturierten Metalloberfläche ändert sich im Laufe der Zeit von einem hydrophilen zu einem hydrophoben Zustand, und es ist schwierig, den hydrophilen Zustand beizubehalten. CA hängt von den physikalischen (topologischen) und chemischen Effekten ab. Die Topographie der mikrostrukturierten Oberfläche ändert sich im Laufe der Zeit nicht. Daher ist der chemische Effekt höchstwahrscheinlich der Grund für die zeitliche Veränderung von CA. Trotz verschiedener Studien über die Langzeitstabilität der Benetzbarkeit ist die Auswirkung chemischer Komponenten jedoch nicht gut bekannt. Eines der Probleme besteht darin, dass es keine anderen Studien gibt, die den Effekt chemischer Komponenten quantitativ diskutieren, da es bisher kein Modell gibt, das CA auf laser-mikrostrukturierten Oberflächen vorhersagen kann. Daher wurde in dieser Studie zunächst zur Analyse der chemischen Wirkung ein Modell entwickelt, das mit mehreren Chemikalien arbeitet. Dann wurden die Methoden zur Vorhersage der CA von verschiedenen Arten von Flüssigkeiten auf der lasermikrostrukturierten Oberfläche entwickelt. Darüber hinaus wurde mit Hilfe dieses Modells die zeitliche Veränderung des CA analysiert. Darüber hinaus wurde vor den Experimenten zu den chemischen Effekten auch ein Merkmal der physikalischen Eigenschaften der Lasermikrostrukturierung untersucht. Im Ergebnis liefert diese Studie Leitlinien für die Gestaltung der physikalischen und chemischen Eigenschaften der Oberfläche zur Steuerung der Benetzbarkeit durch Lasermikrostrukturierung.

Abstract

Surface functionalization is the process of imparting a function (wettability change, friction change) to a surface by giving it a physical or chemical treatment. In recent years, surface functionalization by laser micro-structuring has been getting attention in many applications. One of the big issues of the laser micro-structured surface of stainless steel is, for instance, the long-term stability of the wettability. This can be described by the contact angle (CA) of liquid on the surface after laser micro-structuring. CA on the micro-structured metal surface changes over time from a hydrophilic state to a hydrophobic state, and it is difficult to maintain the hydrophilic state. CA depends on the physical (topological) and chemical effects. The topography of the micro-structured surface does not change over time. Therefore, the chemical effect is the most probably the reason for the change of CA over time. However, despite various studies about the long-term stability of wettability, the effect of chemical components is not well known. One of the problems is that there are other studies that quantitatively discuss the effect of chemical components since there is no model which can predict CA on laser micro-structured surfaces, up to now. Therefore, in this study, at first, as an analysis of the chemical effect, a model that deals with multiple chemicals was developed. Then, the methods for predicting CA of different kinds of liquids on the laser-micro-structured surface were developed. In addition, by using this model, the change of the CA over time was analyzed. Moreover, prior to this chemical effect experiments, a feature of the physical properties of laser micro-structuring is also investigated. As a result, this study gives the guidelines for designing the physical and chemical of the surface for controlling wettability by laser micro-structuring.

List of Abbreviations

Abbreviation	Description
CA	Contact angle
PTFE	Polytetrafluoroethylene
USP	Ultra short pulse
ps	pico second
fs	femto second
LIPSS	Laser-induced periodic surface structure
SFE	Surface free energy
XPS	X-ray photoelectron spectroscopy
SEM	Scanning electron microscope
FIB	Focus ion beam
Al	Aluminum
FRP	Fiber reinforced polymer.
PA6	Polyamide 6
PP	Polypropylene
TP-FRPC	Glass fiber-reinforced thermoplastics composites
GF	Glass fiber

Latin variables	Unit	Description
R	-	Reflectivity
T	-	Transmittance
A	-	Absorptivity
I_z	W/m^2	Intensity
e	C	Elementary charge
N	m^3	Density of free electron
m^*	kg	Effective electron mass
c_e	$J/(KgK)$	Electron specific heats
c_i	$J/(KgK)$	Lattice specific heats

T_e	K	Electron temperature
T_i	K	Lattice temperature
Q	J	Energy released in the electron subsystem
E_p	J	Energy of irradiated laser beam
E_{abl}	J	Energy that need to ablation (evaporate the material)
E_v	J	Energy that used for the kinetic and thermal energy in vapor
E_{res}	J	Residual heat
$T_{x_c,y_c}^{s.p.}$	K	Temperature from single pulse
c	J/(KgK)	Material-specific heat capacity
f_{rep}	1/s	Repetition rate of laser
N	-	Number of pulses
r	-	Structure parameter that indicates the increase of interfacial contact area compared to a flat surface
f	-	Fraction of wetted area
a_i	-	Area ratio of the surface of each chemical components
W_A	mN/m	Adhesion force
W_{Ai}	mN/m	Adhesion force for each chemical component
W_{Ac}	mN/m	Effective adhesive force
S_p	$(\text{mN/m})^{(1/2)}$	Coefficient of polar part for solid at the equation.
S_d	$(\text{mN/m})^{(1/2)}$	Coefficient of dispersive part for solid at the equation
R^P	$(\text{mN/m})^{(1/2)}$	Polar parts of the residual squared sum
R^D	$(\text{mN/m})^{(1/2)}$	Dispersive parts of the residual squared sum
k_i	(mN/m)	Coefficient of each chemical components for C_m
C_m	-	Value for calculating effective CA θ_{0c}
$D_{m(i)}$	°	Angle from the effect of each chemical component between different days on θ_{0c}
d_n	day	Day of measured variables
d_m	day	Day of measured variables
N_a	-	Number of pulses per area
$F_{thN_a=1}$	J/cm^2	Damage threshold at a single pulse
$F_{th,N_a\to\infty}$	J/cm^2	Damage threshold at high numbers of pulses per area
PO	%	Spatial pulse overlap

Greek variables	Unit	Description
α_{ab}	1/m	Absorption coefficient
ω_p	1/s	Plasma frequency
ϵ_0	-	Relative permittivity in vacuum

ϵ	-	Total relative permittivity
ϵ_b	-	Relative permittivity from interband transition
ω	$1/s$	Frequency of laser in vacuum
Γ	$1/s$	Inverse of the average scattering time of electrons
ϵ_1	-	Real part of total relative permittivity
ϵ_2	-	Imaginary part of total relative permittivity
κ_e	$W/(mK)$	Electron thermal conductivity
κ_i	$W/(mK)$	Lattice thermal conductivity
η_{res}	-	Ratio for calculating residual heat from irradiated laser beam
ρ	kg/m^3	Density of material
κ	m^2/s	Thermal diffusivity
θ_0	°	CA at flat surface
σ_S	mN/m	SFE of solid surface
σ_L	mN/m	Surface tension of liquid surface
σ_{SL}	mN/m	Interfacial tension between solid and liquid
θ_W	°	CA at Wenzel state
θ_{CB}	°	CA at Cassie-Baxter state
θ_{0c}	°	Effective CA for a flat but chemically heterogeneous surface
σ_{effS}	mN/m	Effective SFE of solid
σ_{Si}	mN/m	SFE of each chemical components at solid
σ_{SiL}	mN/m	Interfacial tension between each chemical components at solid and liquid
σ	mN/m	Total SFE
σ^P	mN/m	Polar part of the SFE
σ^D	mN/m	Dispersive part of the SFE
σ_S^P	mN/m	Polar part of SFE for solid
σ_S^D	mN/m	Dispersive part of SFE for solid
σ_L^P	mN/m	Polar part of SFE for liquid
σ_L^D	mN/m	Dispersive part of SFE for liquid
σ_i	mN/m	Total SFE for each chemical component
σ_i^P	mN/m	Polar part of the SFE for each chemical component
σ_i^D	mN/m	Dispersive part of the SFE for each chemical component
σ_{Si}^P	mN/m	Polar part of SFE for the solid of each chemical component
σ_{Si}^D	mN/m	Dispersive part of SFE for the solid of each chemical component
α	$1/m$	Absorption coefficient during pulse train
α_0	$1/m$	Initial absorption coefficient
β	cm^2/J	Coefficient for the pulse induced change of absorption coefficient
γ	cm^2/J	Coefficient for the pulse induced change of critical energy density

Chapter 1

Introduction

The surface functionalization is the process of imparting a function to a surface by giving it a physical or chemical treatment. The function includes wettability control, friction control, gloss control, and so on. This surface functionalization is expected to use in technical applications. For example, in medical applications, guide wires in surgeons should have special surface properties for friction force reduction. Another example is that in the manufacturing industry, a part of the material should have special surface properties for joining different materials such as stainless steel and composite material.

There are various technologies to achieve such surface functionalization (wettability). One of the techniques to control wettability is achieved by polytetrafluoroethylene (PTFE) coatings of the surface. While this technology is widely used, it also has the challenge that the coated PTFE could peel off, which should not happen in surgeons. One of the techniques to control wettability is achieved by plasma etching. For example, this technology is expected to be used in the edge surface of the cable of optical fiber. However, it has disadvantages such as time-consuming, and the limitation of materials for plasma processing.

In recent years, surface functionalization by laser micro-structuring has been getting attention in many applications [1, 2]. The advantages of laser technology are that no coating needs to be applied for surface functionalization, partial processing is possible, and furthermore, almost any material can be processed. However, there are several disadvantages of laser micro-structuring. One of the problems of laser micro-structured surface functionalization that has not been solved even at present is the long-term stability of the surface wettability after laser micro-structuring. For instance, the measured contact angle (CA) between water and metal surfaces, which is one of the indications of wettability, changes from day to day after laser structuring and only reaches a stable value after a long time [3, 4, 5].

The change of CA on a metal surface is realized by changing the physical (to-

pography) and chemical components of the material surface by ultra-short pulse (USP) laser. However, regarding the change of CA, several researchers showed that the topography of the laser micro-structured surface was not changed over time. Therefore, the change of chemical properties over time is considered the reason for the change of the CA at laser micro-structured surfaces over time.

Despite various studies about the long-term stability of wettability on laser micro-structured surface, there are still challenges. Regarding laser micro-structuring, the sponge-like structure is of interest because CA on sponge-like structures can be super-hydrophobic. However, the boundary of the growth mechanism (debris or heat accumulation) of a bumpy structure is not well known. Therefore, in this study, to know the boundary of this growth mechanism of sponge-like structures, the heat accumulation was controlled by changing the time interval between laser pulses (1 µs, 2.5 µs, and 25 µs) and their peak fluence (pulse energy), while maintaining a constant spatial pulse overlap. Regarding chemical effect, for understanding the effect of multiple chemical components, the issue in previous studies is that few models in previous studies have considered the effects of multiple chemical components. Therefore, this study develops a model that shows the relationship between CA and multiple chemical components on laser micro-structured surfaces. This model can treat multiple chemicals and is usable for predicting different kinds of liquids on the laser-micro-structured surface. And, by using this model, the change of the CA over time was analyzed.

Moreover, the created laser micro-structured surface was applied to applications such as friction properties of stainless wire in medical applications and joining properties between stainless steel and composite material.

As a result, this study contributes one of the guidelines for designing the physical and chemical of the surface for controlling wettability by laser micro-structuring.

Chapter 2

Theory and Modeling

The change of CA on a metal surface is realized by changing the physical (topography) and chemical components. To change the topography and chemical components of the sample surface, the laser micro-structuring technique was used in this study.

Therefore, at first, in this chapter, the basics of the laser process and the state-of-the-art formation mechanism of micro-structure on the sample are explained.

In addition, to investigate the CA on laser micro-structure, the basic theory of CA will be explained. Then, state-of-the-art researchers on the change of CA are described. The challenge here is the basic model cannot deal with multiple chemical components' effects. Therefore, to investigate the change of CA overtime on the laser micro-structured surface, the research strategy is first to identify the relationship between CA and multiple chemical components, and then use this relationship to discuss how CA changes over time. Therefore, the theory of dealing with multiple chemical components was developed in this work and is explained.

2.1 Laser micro-structure

2.1.1 Basic of Laser process

The laser process begins when the energy of the laser is absorbed by the material. Therefore, the laser process is outlined in terms of energy. When the laser beam is irradiated on the surface, a portion of the energy of the laser beam is initially reflected at the material interface. This rate of reflectivity is described by R which depends on the complex refractive index. The remaining part of the energy of the laser beam penetrates the material and is absorbed or transmitted. The transmitted ratio is described by the transmittance T, and the absorbed ratio by the absorptivity A. Due to the conservation of energy, the following eq. (2.1) is required. The

schematic image of laser beam energy is in the fig. 2.1

$$1 = R + T + A \tag{2.1}$$

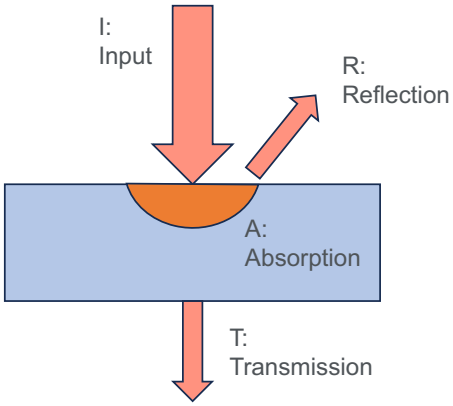

Figure 2.1: Energy of irradiated beam, reflected beam, absorption, and transmitted beam

The behavior of the absorption of laser energy in the material can be described with the help of the absorption coefficient α_{ab} by Beer's absorption law [6] in the eq. (2.2).

$$I_z = I_{z=0} exp(-\alpha_{ab} z) \tag{2.2}$$

where I is the intensity of the laser beam, which is energy density per second (W/m^2), z is the depth of the laser in the material. The optical penetration depth z_{opt}, defined as the length after which the initial intensity has been reduced to its $1/e$, corresponds to the reciprocal of the absorption coefficient. If z_{opt} is very smaller than the thickness of the material, then the transmitted portion of the light can be neglected. For example, metals' optical penetration depth for visible light is around 10 nm. This absorbed energy drives the laser structuring (material removal and surface shape change).

To consider the details of the laser process, the elementary processes of how this absorbed energy changes the structure of the material is explained in the next section.

The laser micro-structuring mechanisms occurring with USP laser are difficult and therefore still part of many discussions [7, 8, 9, 10, 11, 12, 13, 14]. Fig. 2.2 shows the time evolution of elementary processes while the laser process is happening.

First, due to differences in the energy band of metals, semiconductors and dielectrics, each kind of material has different mechanisms of laser absorption. In

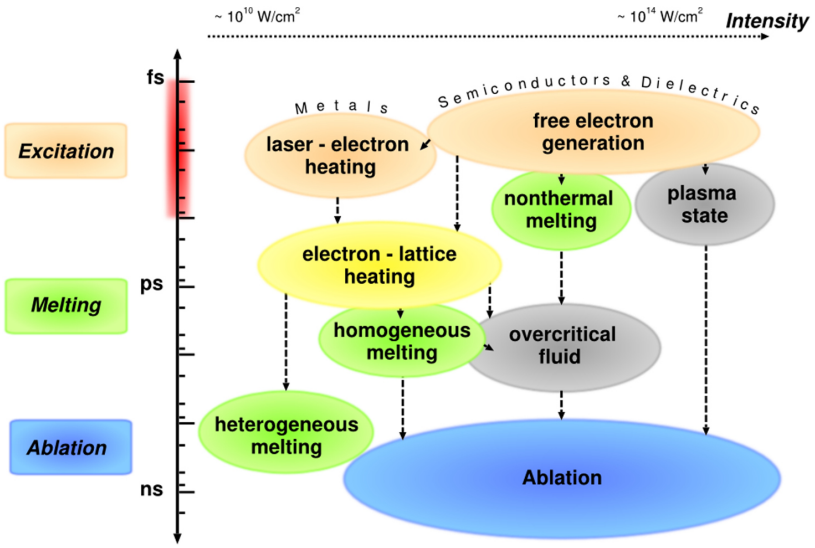

Figure 2.2: Time development of the elementary processes for laser processing [7]

this study, metal will be processed, so the laser process for metals is discussed. In metals, the energy of the laser beam is mainly absorbed in the free electron and the free electrons are heated in the range of femtosecond (laser electron heating in fig. 2.2). Due to this light and electron interaction, the reflection of light or absorption coefficient is defined. The most common model for describing the motion of free electrons while the laser is irradiated is Durde approach [15]. This model treats metal as a lattice with free electrons. From this model, complex permittivity is derived as shown in eq. (2.3) to eq. (2.6).

$$\omega_p = \sqrt{\frac{e^2 N}{\epsilon_0 m^*}} \tag{2.3}$$

$$\epsilon = \epsilon_b + \frac{\omega_p^2}{\omega^2 - i\Gamma\omega} \tag{2.4}$$

$$\epsilon_1 = \epsilon_b - \frac{\omega_p^2}{\omega^2 + \Gamma^2} \tag{2.5}$$

$$\epsilon_2 = \frac{\omega_p^2 \mathrm{T}}{\omega(\omega^2 + \Gamma^2)} \tag{2.6}$$

where ω_p is plasma frequency, e is elementary charge, N is density of free electron, ϵ_0 is relative permittivity in vacuum, m^* is effective electron mass. ϵ is total relative permittivity, ϵ_b is relative permittivity from interband transition, ω is frequency of light in vacuum, Γ is inverse of the average scattering time of electrons. ϵ_1 is real part of total relative permittivity, ϵ_2 is imaginary part of total relative permittivity.

Since this complex permittivity depends on the angular frequency of light and parameters of materials, the absorption coefficient depends on the material and the laser wavelength as it is shown in fig. 2.3.

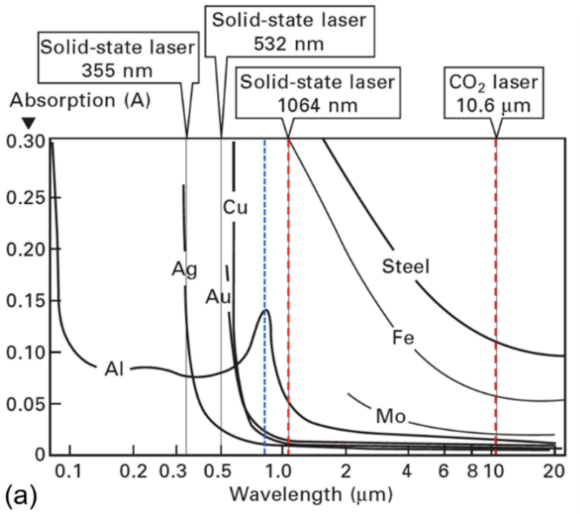

Figure 2.3: Absorption coefficient of metal: image is taken from referenced book [16]

Then, the excited electron can interact with the lattice, and energy is transported from the electron to the lattice, and the lattice can have energy within around a few picoseconds (ps) depending on the material [17] (electron lattice heating in fig. 2.2). For this phenomenon, the two-temperature model [7], which calculates the temperature of electrons and lattice, is used for discussion as shown in eq. (2.7), eq. (2.8).

$$c_e \frac{\partial T_e}{\partial t} = \mathrm{div}(\kappa_e \nabla T_e) - \alpha(T_e - T_i) + Q \tag{2.7}$$

$$c_i \frac{\partial T_i}{\partial t} = \mathrm{div}(\kappa_i \nabla T_i) + \alpha(T_e - T_i) \tag{2.8}$$

where c_e, c_i are the electron and lattice specific heats. T_e, T_i are the electron and lattice temperatures, κ_e and κ_i are thermal conductivities of the electron and phonon subsystems. Q is the energy released in the electron subsystem due to laser radiation absorption.

While this happens, the electron can also diffuse spatially and the energy of the lattice can also conduct spatially by heat conduction. Therefore, a few picoseconds (ps) after energy input, material states become different states (phase transitions), such as heterogeneous melting, homogeneous melting, overcritical fluid, and ablation in fig. 2.2. In this time region, molecular dynamics simulation [18, 19] or hydrodynamic simulation [11] were used to study the process numerically. This different phase transition depends on the intensity (energy density $\mathrm{W/cm^2}$) according to fig. 2.2. After phase transitions take place and part of the irradiated material expands and separates from the rest of the material.

Since the above process happens very quickly and with high local energy densities, at the outside of material, shock wave, plasma [20, 21], droplets or debris, can also be generated, which further influence the ablation process as you can see on the fig. 2.4. And also, the inside of the material, mechanical shock waves [22, 8], remaining overheated liquid [23] in material can also be generated. This shock wave and remaining heat can also change the melt flow and solidification, then affect to the surface morphology modification.

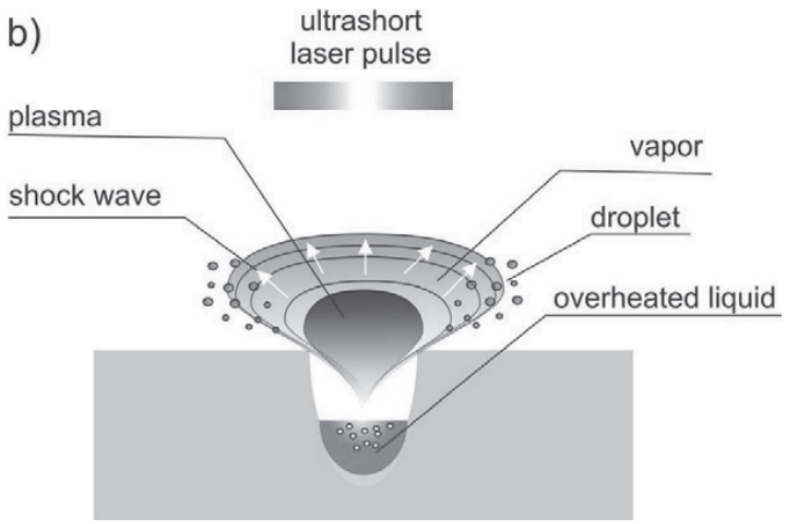

Figure 2.4: The several byproducts while material expands [24]: plasma, shock wave, vapor, droplet or debris, overheated liquid.

2.1.2 Basic of surface morphology

For many industrial applications, the laser process is applied to a larger area than the spot size of the laser beam. In order to make the large area, the laser spot must be scanned over the entire surface to be processed. As it described in the previous section, the phenomenon of prior laser pulse ablation will affect to the next laser pulse ablation. For example, plasma at the outside of material, debris, can decrease the laser energy and distort the wavefront of the laser. In addition, the crater or the deposited debris can change the reflectivity and absorption coefficients. Moreover, the residual heat can change the absorption coefficient of the laser and change the process or time of solidification of the material. Therefore, the scanning method (spatial pulse overlap, time interval of pulse to pulse and pulse, energy as you can see on fig. 2.5) changes the surface structure.

When the laser is irradiated in the same spot, then it can make micro-sized structures such as holes, and dimple structures as shown in fig. 2.6a. While the laser is

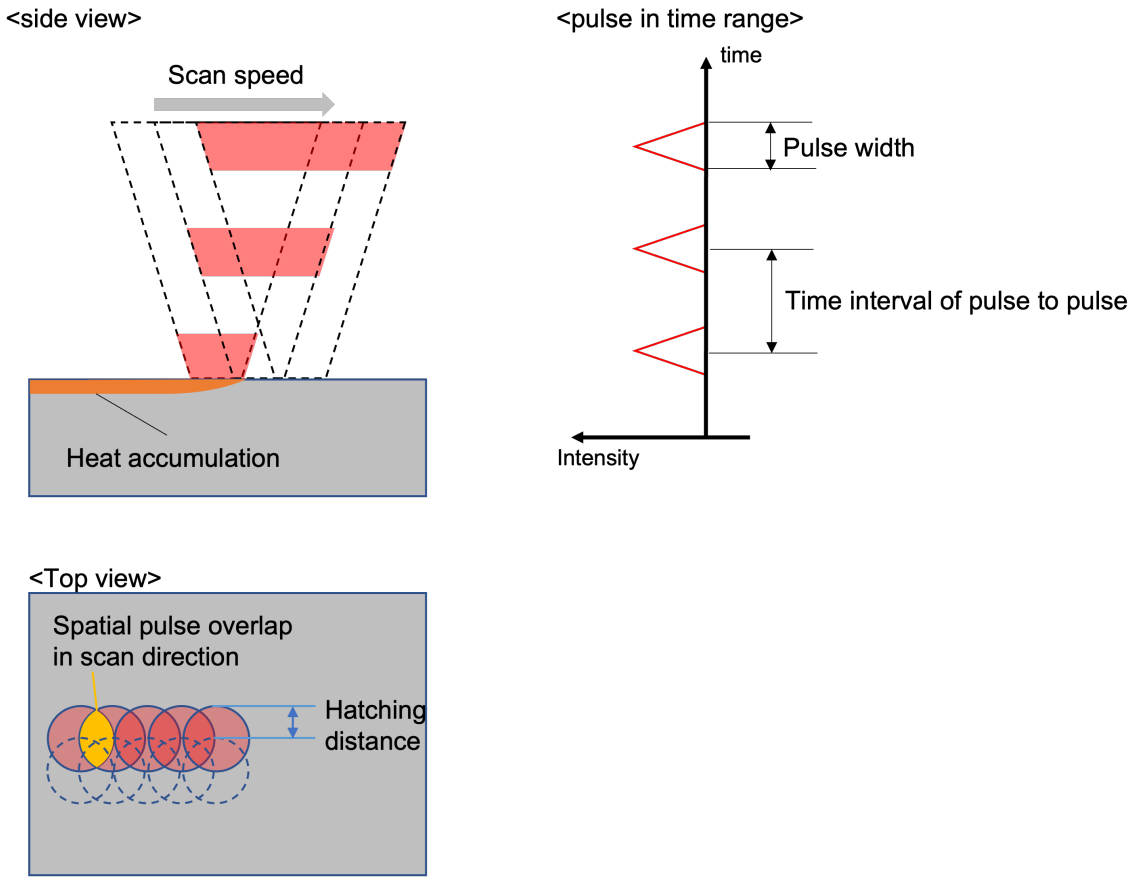

Figure 2.5: laser process parameters: scan speed, pulse width, time interval of pulse to pulse, spatial pulse overlap.

not only for creating micro-sized structures but also can create self-organized structure. There are many types of surface laser-induced structures reported [25, 26]. One of the self-organized structures is laser-induced periodic surface structure (LIPSS) whose periodic pattern is typically shorter than the wavelength of the laser beam, as it can be seen in fig. 2.6b. This kind of structure is interesting for friction reduction and also for surface colorings. Another self-organized structure is microgrooves [27, 28] which are formed parallel to the laser polarization with a period significantly larger than the laser wavelength are indicated. Another self-organized structure is called the bumpy [29] / sponge-like [30] / Coral-like [26] structure whose morphology has micro-scale holes and pillars on the surface and nano-scaled substructure on each surface as it can be seen in fig. 2.6c.

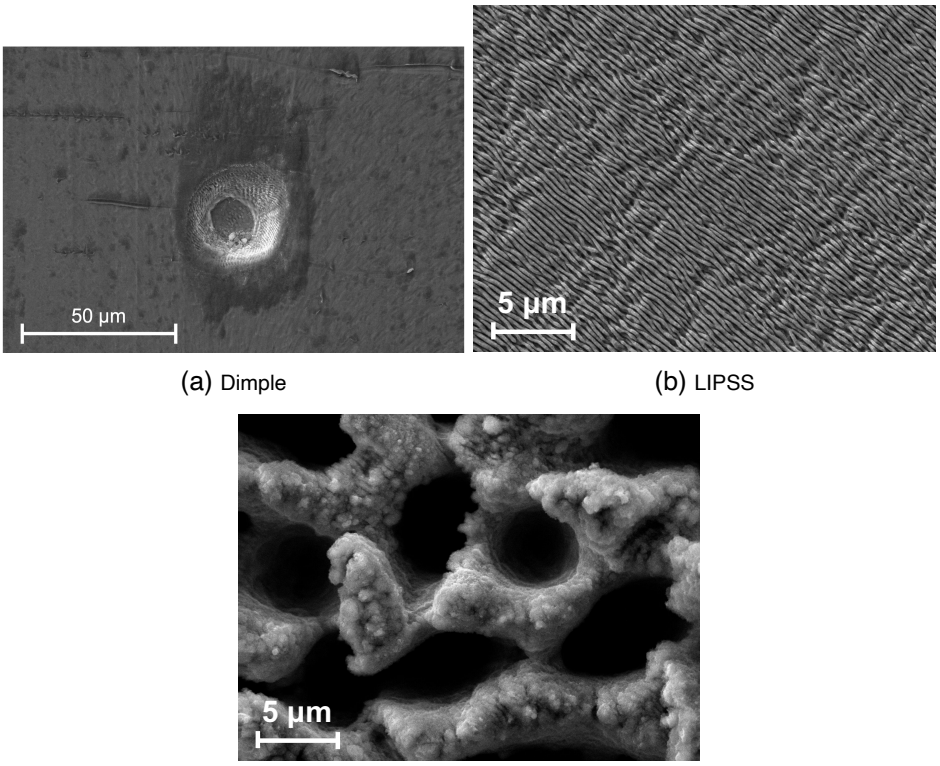

(a) Dimple (b) LIPSS

(c) Bumpy/Sponge-like structure

Figure 2.6: The structure which can be created by USP laser

Regarding the relationships between surface morphology and CA, according to S.moradi et al. [31], a bumpy/sponge-like structure is expected to have a superhydrophobic. And also according to Kietzig et al. [3], the CA of bumpy/sponge-like structure change over time from super-hydrophilic to super-hydrophobic. Therefore, in this study, the sponge-like structures are interesting since they realize the extreme change of CA otherwise sensitive for chemical surface properties changes and has merit for industrial usage.

2.1.3 State of the art: Mechanism for growth of sponge-like structure

Since there are lots of process parameters for creating morphology by laser process, to create sponge-like structure, the growth mechanism of sponge-like structure is important. However, this laser-induced surface structure formation mechanism is complex and therefore still part of many discussions [25, 26, 27, 28, 29, 30].

Regarding the growth mechanism of a sponge-like structure, the existing models may be roughly divided into two groups. One growth mechanism is that the structure or debris deposition affects the reflection and absorption of subsequent laser pulses, expanding the previous structure [32, 33] as shown in fig. 2.7a. Another growth mechanism is that heat accumulation causes grooves to grow through convection mechanisms, leading to the formation of bumps [23, 26, 29, 32, 34] as shown in fig. 2.7b.

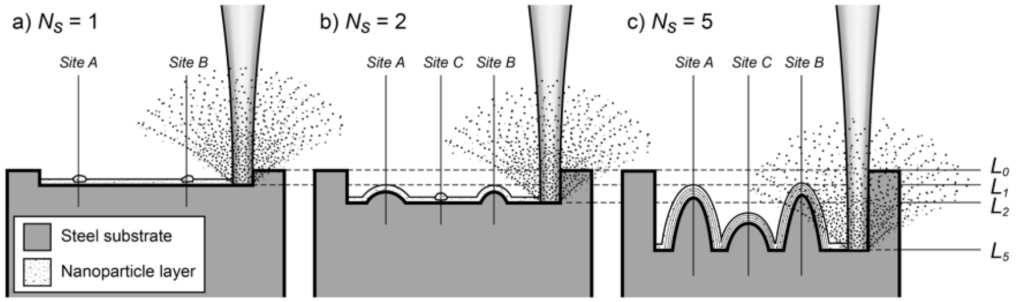

(a) Model of structure or debris deposition affects the reflection and absorption:image was taken from the paper [33]

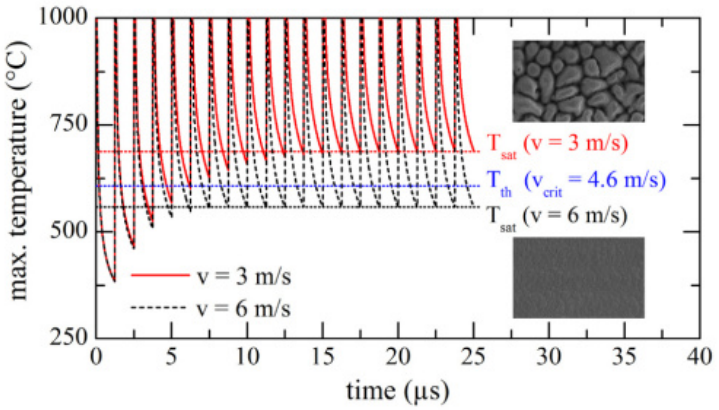

(b) Model of Heat accumulation temperature: image was taken from the paper [23]

Figure 2.7: Two types of growth mechanism of sponge-like structure

Regarding the boundary of the growth mechanism of a sponge-like structure, Zuhlke et al. [32] suggest that laser fluence (J/cm^2) is one of the indicators. This is because when the laser fluence is high with the same repetition rate of the laser, heat accumulation is more likely to happen. However, the heat accumulation can

be low even if in the high fluence when the pulse repetition rate is low. Thus, the boundary of the growth mechanism of sponge-like structures is not-well known yet. For creating sponge-like structures in industrial applications (e.g., wires for medical devices, etc.), heat accumulation is important to prevent the bending of the sample. Therefore, it is important to know the boundary of this growth mechanism of sponge-like structures and process windows for sponge-like structures. To know the boundary of this growth mechanism of sponge-like structures, heat accumulation is varied by changing the time interval of pulses with the same spatial pulse overlap. This will be discussed in Chapter 4.

The model of heat accumulations

For the estimation of the heat accumulation, heat accumulation is calculated by the heat conduction model. According to Bauer et al. [23], within the laser energy absorbed by the material, the energy not used for ablation and kinetic energy of material removal contributes to an increase the temperature of the material.

$$AE_p = E_{abl} + E_v + E_{res} \tag{2.9}$$

$$E_{res} = \eta_{res} E_p \tag{2.10}$$

where A is the ratio of absorption in eq. (2.1), E_p is the Energy of irradiated laser beam, E_{abl} is the energy that need to ablation, E_v is the energy that used for the kinetic and thermal energy in vapor, E_{res} is residual heat, η_{res} is ratio for calculating residual heat from irradiated laser beam. Before this residual energy is reduced via heat conduction, when the next laser pulse is irradiated, it causes heat accumulation in the material. The residual energy is expressed as shown in eq. (2.10). For the calculation of the residual heat, the heat dissipation after the laser pulse is determined by the heat conduction equation. For a single pulse of a Gaussian-profiled heat source with the radius w_0 of the laser spot on the semi-infinite solid, the temperature raised inside an infinite homogeneous solid at position x, y, z at time t is given by eq. (2.11).

$$T^{s.p.}_{x_c,y_c}(x,y,z,t) = \frac{2E_{\text{res}}}{\pi\rho c\sqrt{\pi\kappa t}(8\kappa t + w_0^2)} \cdot e^{\frac{(x-x_c)^2+(y-y_c)^2}{4\kappa t}\left(\frac{w_0^2}{8\kappa t+w_0^2}-1\right)} \cdot e^{-\frac{z^2}{4\kappa t}} \tag{2.11}$$

where $T^{s.p.}_{x_c,y_c}(x,y,z,t)$ is temperature from single pulse. The center of single pulse is $(x_c, y_c, 0)$. t is the time elapsed after the instantaneous heating pulse. c is the material-specific heat capacity. ρ is the density and κ is the thermal diffusivity.

$(x - x_c), (y - y_c)$ and z represent the respective distances from the centre $(x_c, y_c, 0)$ of the Gaussian distribution.

A new pulse is applied after $\Delta t_{p-p} = 1/f_{\text{rep}}$ (f_{rep} is the repetition rate of laser) and is hence superposed onto the temperature distribution of the previous pulse. Also, the spatial displacement $v\Delta t_{p-p}$ of the subsequent pulses resulting from the scanning speed v is accounted for by adjusting the center coordinates of the Gaussian distribution. The temperature distribution after N pulses is thus given by

$$T(x, y, z, t) = \sum_{i=0}^{N} T^{s.p.}_{x_{c_i}, y_{c_i}} \left(x, y, z, t + i \cdot \Delta t_{p-p}\right) \tag{2.12}$$

where $x_{c_i} = i \cdot v\Delta t_{p-p}$ for scanning in x-direction and starting at the origin. Another assumption of this simulation is that the phase change is not included, the thermal physical properties of stainless steel are not dependent on temperatures, the heat transfer to air is not included, and fluid dynamics is not included. Even though this assumption, this analytical calculation already represents a valuable tool to estimate the heat accumulation in the scanning of ultra-short pulses [23]. The thermodynamic properties of the materials (stainless steel 304) were referenced from the literature [35, 36]. They are summarized in tab. 2.1

Table 2.1: simulation input data

parameter	value
density	7.9 Kg/m^3 [35]
heat capacity	500 J/(KgK) [35]
Thermal diffusivity	3.8 m^2/s [35]
Melting temperature	1673.15 K [36]
boiling temperature	2773.15 K [36]

After conducting the simulation, the time profile of the heat accumulation temperature is obtained as it is shown in fig. 2.7b. As it is described in the literature [23], considering the lower envelope of the temperature values reached directly before the subsequent pulse is applied in fig. 2.7b, a saturation value T_{sat} can be defined. In the model, when the saturation temperature exceeds the critical threshold temperature, then the stochastic structure appears. Additionally, according to [23], this critical threshold temperature was set by comparing the results of the T_{sat} calculations with measurements of the shape of the surface after processing, and was set at 607°C as it can be seen on fig. 2.7b.

2.2 Basic theory for CA

Wettability is one of the surface properties and shows the ability of a liquid to spread over a surface. It is described as hydrophobic in the case of water-repellent or hydrophilic in the case of water-permeable. The wettability is characterized by the contact angle (CA) at the edge of the liquid drop on the material surface as it is shown in fig. 2.8. In addition, the wettability state is called differently depending on the angle of the CA. When CA is less than $10°$, between $10°$ and $90°$, between $90°$ and $150°$, and greater than $150°$, it is referred to as super hydrophilic, hydrophilic, hydrophobic, and superhydrophobic, respectively [37, 38, 39].

This stable CA is determined when the system containing the liquid and the solid is at equilibrium with minimum energy. The most used models to calculate the CA is called Young's equations [40] as shown in eq. (2.13) and fig. 2.8. In this model, at the edge of the liquid drop in fig. 2.8, CA is determined when three forces are balanced. These forces come from (a) the liquid surface trying to minimize the surface to reduce the system energy, and (b) the interfacial surface of the liquid and solid also trying to minimize the surface to reduce the system energy, (c) the solid surface trying to reduce the energy by covering the liquid surface.

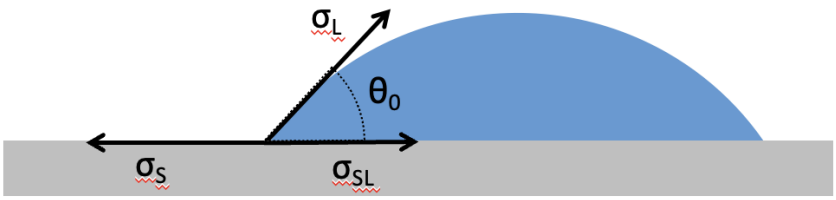

Figure 2.8: Young's model: the model of CA for flat surface

$$\cos\theta_0 = \frac{\sigma_S - \sigma_{SL}}{\sigma_L} \tag{2.13}$$

where θ_0 is the CA. σ_S is the surface free energy (SFE) or surface tension of solid surface. σ_L is the SFE or surface tension of liquid surface. σ_{SL} is interfacial tension between solid and liquid.

The model of Young is used for the flat surface and chemically homogeneous surface. However, laser micro-structured surface has rough surface and also the aged surface has a chemically heterogeneous surface due to contaminations. C. Elif Cansoy et al. [41], B.H. Luo et al. [42], or M. H. Kwon et al. [43] showed that

this CA depends on physical (topographical) properties. Therefore, to discuss the CA on the laser micro-structured surface, the effect of topography on CA is needed think. Additionally, as we can see σ_S, and σ_{SL}, on eq. (2.13), the CA also depends on chemical properties of the solid surface and interfacial tension between the liquid and solid. Therefore, to discuss the effect of chemicals, the basic model of chemical properties will be described.

The model of the effect of topography

Regarding the physical part of the surface, a laser micro-structured surface can be interpreted as artificial roughness. In this case, the CA measured on a laser micro-structured surface differs from the CA on a flat surface as calculated by eq. (2.13). Most descriptions of the CA on a rough surface are based on the Wenzel model [44] as the equation is shown in eq. (2.14), and the Cassie-Baxter model [45] as the equation is shown in eq. (2.15). Wenzel model represents CA when the liquid covers all rough structured surfaces as it is shown in fig. 2.9a. In this case, the interfacial surface (orange-colored area) at the rough surface is larger than that of the flat surface. Since the increase in surface per unit area (r in eq. (2.14)) is the increase in force per this unit area of σ_S, and σ_{SL}, the expression of Wenzel model is shown in eq. (2.14). On the other hand, the Cassie-Baxter model shows the CA when the liquid contact only the protuberance of the rough surface (yellow-colored area) as it is shown in fig. 2.9b. In this case, the average in force per this unit area of σ_S, and σ_{SL} is determined by the ratio of the contact area to the air area. The CA in the air region is considered $180°$. Therefore the expression of Cassie-Baxter model is shown in eq. (2.15). H.Hu et al. [46] shows Cassie-Baxter model can explain the state of the hydrophobic and super hydrophobic states. Therefore, when the measured CA is in a super-hydrophilic and hydrophilic state, the Wenzel equation is used and when the measured CA is in a hydrophobic and super-hydrophobic state Cassie-Baxter equation is used. In this research, when the measured CA is over $120°$ then the Cassie-Baxter equation is used.

$$\begin{aligned} \cos\theta_W &= \frac{r(\sigma_S - \sigma_{SL})}{\sigma_L} \\ &= r\cos\theta_0 \end{aligned} \tag{2.14}$$

$$\begin{aligned} \cos\theta_{CB} &= f(\cos\theta_0) + (1-f)\cos(180°) \\ &= f(\cos\theta_0 + 1) - 1 \end{aligned} \tag{2.15}$$

where θ_W and θ_{CB} are the CA for the Wenzel equation or Cassie-Baxter equation, respectively. θ_0 is the CA for a flat surface, r is the structure parameter that indicates the increase of interfacial contact area compared to a flat surface, and f is

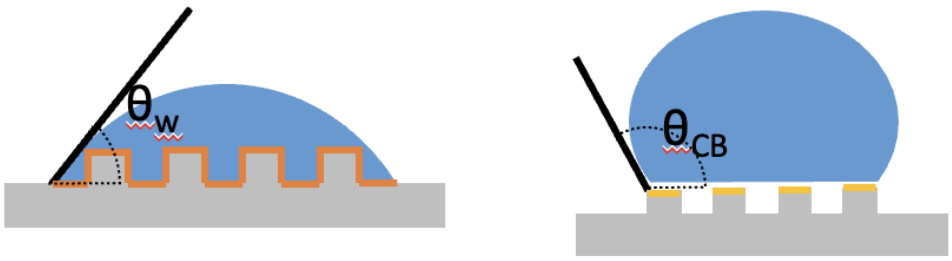

(a) Wenzel model (b) Cassie-Baxter model

Figure 2.9: CA models at rough surface

the fraction of wetted area. Therefore, the rough surface is represented by these structure parameters (r, f) and these values convert the CA on rough surface from CA on a flat surface. How these structure parameters (r, f) are obtained at real structure is explained in section 3.4.2 and 3.4.3.

The models of the effect of chemical

The effect of chemical properties of solid surface is expressed in the terms (σ_S and σ_{SL}) in eq. (2.13). To reduce the variants, the term of interfacial tension (σ_{SL}) is needed to be described by the term of SFE for solid (σ_S) by using the equations of adhesion force between liquid and solid. The equation for adhesion force from the point of view of the total energy of the system is searched by Dupre [47] and shown in eq. (2.16). The image of the concept is shown in fig. 2.10. The left side of the fig. 2.10 is the state where the liquid and solid are connected with adhesive force (state A) and the right side of the fig. 2.10 shows the state where the liquid and solid are apart from each other (state B). Since state B has more surface than state A, the total energy of the system of state B is higher than state A. To change from state A to state B, energy which is same amount of adhesion work is needed to put into the state A. This relationship is shown in eq. (2.16)

$$W_A = \sigma_S + \sigma_L - \sigma_{SL} \tag{2.16}$$

where W_A is the adhesion force.

In order to describe the term of interfacial tension (σ_{SL}) by the term of SFE for solid (σ_S), another description of adhesion force from a different point of view is needed. The adhesion force which is described from the intermolecular force is shown in the model from Owen and Wendt [48]. According to Owen et al. [48], this intermolecular force is divided into the dispersive part and polar part as shown in

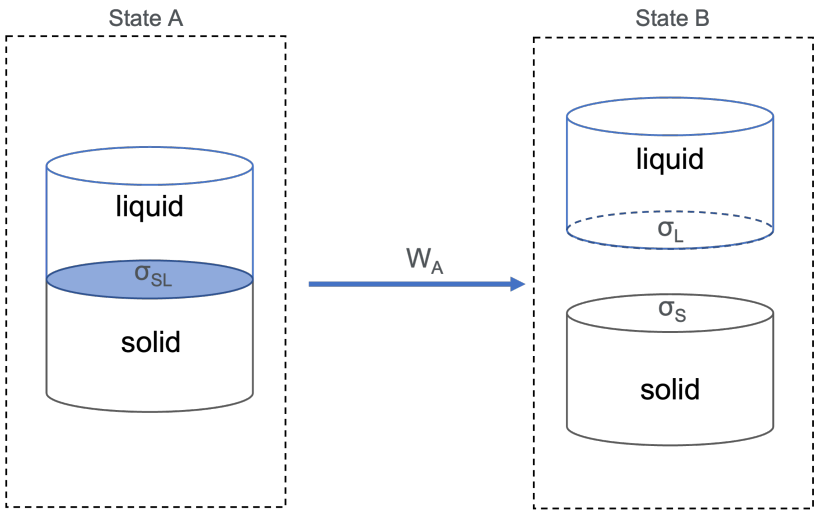

Figure 2.10: Dupre's model: The model for adhesion force from thermodynamics

eq. (2.17). The dispersive part comes from the interaction of London dispersive force [49]. The polar part comes from the interaction of the metallic bond or the hydrogen bond. According to Owen et al. for these forces only interact with each part of SFE: the polar part of liquid only interacts with the polar part of solid as shown in fig. 2.11. Therefore, it is important to calculate the adhesion force to obtain the dispersive part and polar part of the surface. The total adhesion force is expressed by the geometric mean as shown in eq. (2.18) [48].

$$\sigma = \sigma^P + \sigma^D \tag{2.17}$$

$$W_A = 2\left(\sqrt{\sigma_S^P \sigma_L^P} + \sqrt{\sigma_S^D \sigma_L^D}\right) \tag{2.18}$$

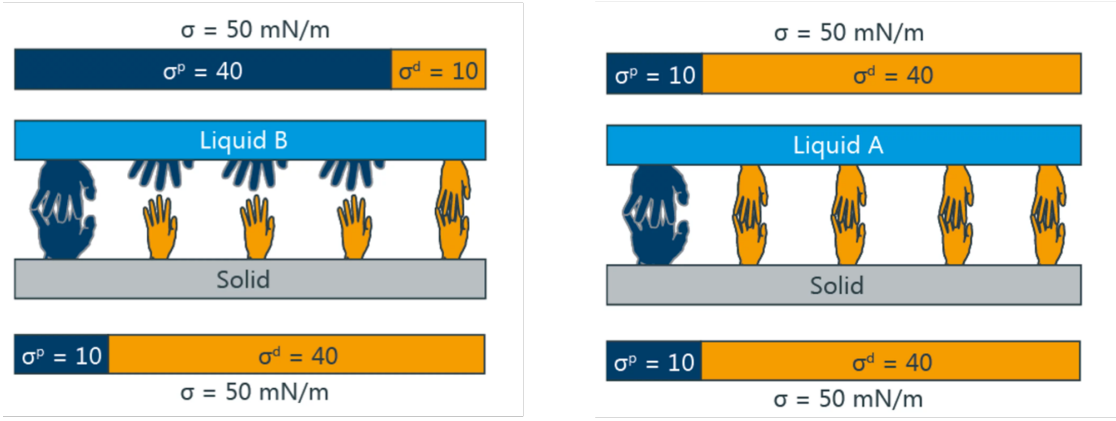

Figure 2.11: Owen and Wend's model: The models for adhesion force from polar and dispersive SFE (referenced from webpage of Krüss [50])

where W_A is the adhesion force. σ, σ^P, σ^D are the total SFE and the polar part and dispersive part of the SFE, respectively. σ_S^P, σ_S^D are the polar part and dispersive

part of SFE for solid, respectively. σ_L^P and σ_L^D are the polar part and dispersive part of the SFE of the liquid.

In the end, by using eq. (2.16), and eq. (2.18), the interfacial tension σ_{SL} is expressed only with the SFE of solid and the SFE of liquid as shown in eq. (2.19).

$$\begin{aligned}\sigma_{SL} &= \sigma_S + \sigma_L - W_A \\ &= \sigma_S + \sigma_L - 2\left(\sqrt{\sigma_S^P \sigma_L^P} + \sqrt{\sigma_S^D \sigma_L^D}\right)\end{aligned} \tag{2.19}$$

With using this equation and eq. (2.13), the CA at a flat surface can be described by the chemical properties of liquid and solid as shown in eq. (2.20).

$$\frac{\sigma_L\,(cos\theta_0 + 1)}{2\sqrt{\sigma_L^D}} = \sqrt{\sigma_S^P}\frac{\sqrt{\sigma_L^P}}{\sqrt{\sigma_L^D}} + \sqrt{\sigma_S^D} \tag{2.20}$$

Generally, to obtain SFE of a solid, the liquids whose surface tension are already known is used. For example, water, or diiode-methane. Then once the SFE of a solid is known, CA at a flat surface can be predicted from this eq. 2.20. The issue of this model is that it can treat the effect of the total SFE of solid but it cannot treat the effect of each chemical component. However, a laser micro-structured surface has a chemically heterogeneous surface by contaminations. One of the challenges of my Ph.D. thesis is to develop a model for a chemically heterogeneous surface. This will be described in the section 2.4.

2.3 State of the art and challenge

Many researchers are currently investigating the control of the wettability of stainless steel surfaces by laser processes [51, 52, 53]. One requirement for material surface wettability in industrial applications is long-term stability for keeping the surface function while the device is stored after its production. In this study, especially the phenomena of the change of CA over time at laser micro-structured surfaces are focused on. The CA on the laser micro-structured metal surface changes from day to day after laser structuring and only reaches a stable value after a long time as shown in fig. 2.12.

The change of ”stable” CA from no laser micro-structured flat surface is realized by changing the topography and chemical components of the material surface by an ultra-short pulse (UPS) laser [41, 42, 43]. However, regarding the ”change” of CA over time, Kietzig et al. [3] C.V. Ngo. et al. [52] showed that the topography

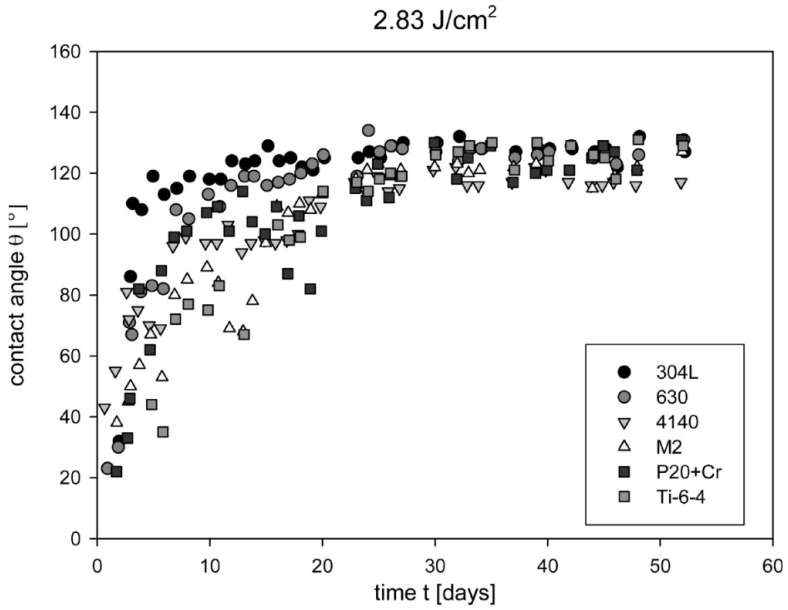

Figure 2.12: The change of CA over time: image is taken from referenced paper [3]

of the laser micro-structured surface was not changed over time. Therefore, the change of chemical properties over time is considered the reason for the change of the CA at laser micro-structured surfaces over time.

In order to investigate the stability of wettability, the effect of chemical properties on the change of CA needs to be understood. However, even the relationship between CA at laser micro-structured surface and chemical properties is not well known. One of the reasons for this is that the surface of a laser micro-structured surface is not chemically homogeneous and there are few models for a chemically heterogeneous surface that directly describe the chemical components' effect on CA. Therefore, many researchers (C.V.Ngo. et al. [52], F.H. Rajab [54], G.Giannuzzi et al. [55]) discuss indirectly chemical components' effects on CA which means without using models but by only comparing a ratio of the chemical components and CA.

Kietzig et al. [3] described the value of stable CA from one chemical components. They created dual-scale roughness structures on different metal surfaces using a femtosecond (fs) laser and measured the CA of water for 30 days. For the discussion of chemical effect, X-ray photoelectron spectroscopy (XPS) analysis was performed on the stainless steel before laser irradiation, immediately after irradiation, and 52 days after irradiation. They showed the XPS results suggest that the observed change in stable CA can be attributed to a certain extent to the presence of carbon and its compounds on the laser-irradiated surfaces as shown in fig. 2.13.

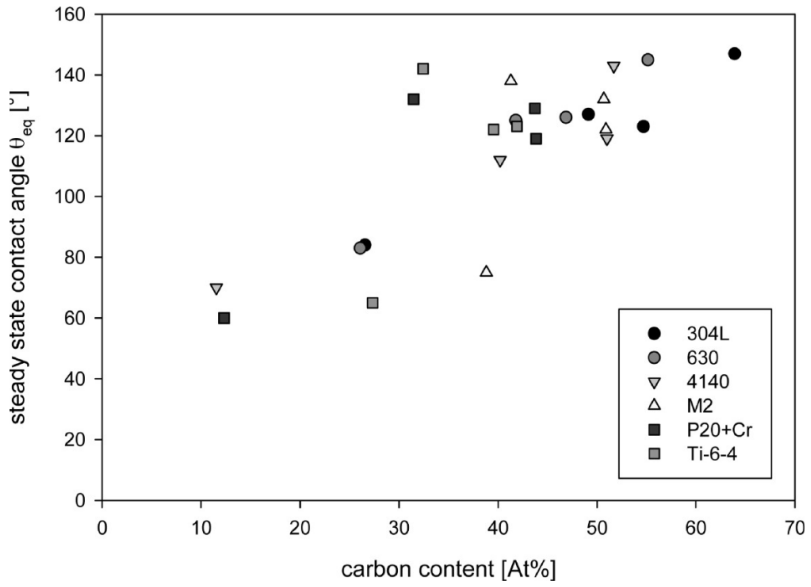

Figure 2.13: The linear relationships between stable CA and carbon: image was taken by the paper [3]

While C. Sciancalepore et al. [56] showed transition of CA by carbon and also oxide metal. They created several types of surface structures on stainless steel and CA measurements were carried each 7days for 120days after the laser treatment. To evaluate the chemistry behavior of the surfaces, XPS measurements were performed on the selected samples immediately after the laser treatment as well as 1, 3, 10 and 30 days later. Fig. 2.14 shows the comparison between the evolution in time of the static CA on each measured day and the Carbon and Oxygen contents. They said that the connection between the evolution of the CA with the chemical state of the surface is quite straightforward. About ten days after the laser texturing process, the CA values begin to stabilize followed by an increase of Carbon content which starts to take place on the steel surface.

However, Pou et al. [53] showed nitrogen and oxygen and iron are the one of the effective variants for CA change. They studied the role of the processing atmosphere (O2, Air, CO2, N2, Ar) in controlling the wettability of commercial AISI 304 by laser texturing. The surface chemical composition differences were quantitatively studied by XPS measurements. Since metal oxides and nitrides increased the polar component of the surface energy, they used ratios of oxygen and nitrogen on iron to explain their the influence on the CA of water [53] as it is shown in fig. 2.15.They found that there is a correlation between this ratio and CA. The environment of laser process changes the surface chemical properties and the effective variants for CA (nitrogen, oxygen, iron) is different from other research conclusions. Thus, there is a challenge to treat the multiple chemical component's effects on CA

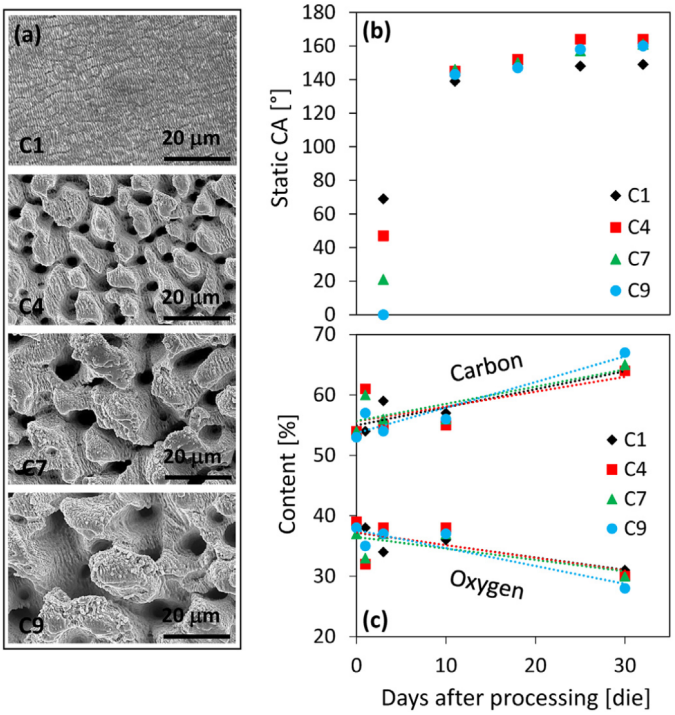

Figure 2.14: The research example of the stable CA over time and chemical components over time: image was taken by the paper [56]

in any environments.

While Becker et al. [57] proposed the quantitative equation for the relationships between CA and chemical components. They studied the ability of the cleaning agents such as cyclohexane, acetone, isopropanol and hydrogen peroxide to remove oil from technical steel. They showed a simple empirical model using two parameters to describe intrinsic CA (CA at a flat surface) to give better results than other models, including linear functions of the chemical concentrations as it is shown as eq. (2.21).

$$\cos\theta_0 = A_1 + A_2\frac{x_C^p}{x_C^{np}} + A_3\frac{x_O}{x_C^p} \tag{2.21}$$

where x_C^p,x_C^{np},x_O are the concentration of polar carbon, non-polar carbon, and organic oxygen, respectively. The values of coefficient A_1, A_2, and A_3 are -0.27, 0.72, 0.12 respectively. This model shows a nice correlation between CA and chemical components and can describe the value of stable CA for two variants. However, there is a challenge in treating the other kinds of chemical components' effects on the CA. In addition, since this model is adjusted to water CA, therefore the model is not available to predict any other kinds of liquids' CA.

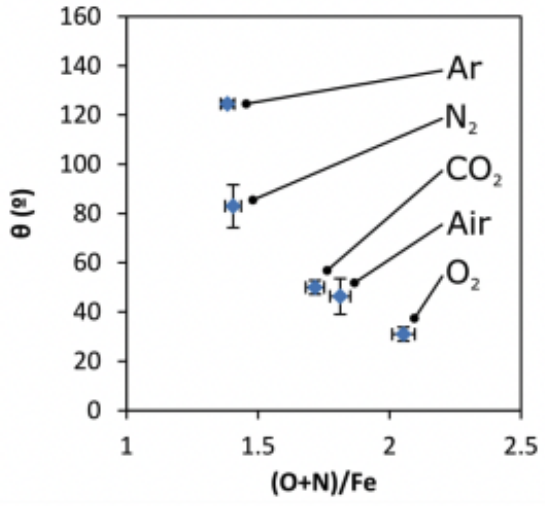

Figure 2.15: The relationships between stable CA and nitrogen and oxygen: the image was taken from the paper [53]

In summary, despite various studies, several challenges exist for the investigation of the stability of wettability. One of the issues in previous studies is that few models in previous studies have considered the effects of multiple chemical components. Therefore, the challenge of this work is, in order to investigate the reason for the change of CA, first, to create a relational equation that directly relates CA (or SFE) to multiple chemical components. The summary of the difference between state-of-the-art research is shown in tab. 2.2

Table 2.2: Summary of the difference between each method and this study.

method	Quantitative discussion of CA	Applicability to chemically heterogeneous surface	Applicability to various liquids	Challenge
comparison [52, 54, 55]	×	-	-	The quantitative discussion is difficult.
one variant [3, 53]	△ [a]	△ [a]	×	The discussion of the effect of multiple chemicals is difficult.
two variants [57]	○	△ [b]	×	The discussion of the effect of other chemicals not chosen here is difficult.

[a] One variant is used.

[b] 2 or 3 variants are used. Also, the variants of the equation need to be thought of every time.

2.4 The model for time dependency: developed in this work

2.4.1 The model for relationships between CA and multiple chemical components

The challenge of this work is, in order to investigate the reason for the change of CA, first, to create a relational equation that directly relates CA (or surface free energy) to multiple chemical components. Therefore, this section describes how the equations relating CA to various chemical components are constructed and how time evolution is considered. The ideas of this model are as follows.

- For the chemical part, unlike other conventional studies, consider the influences of a variety of chemical components.
  - Extend the equations for adhesion force and SFE to be used with a variety of chemical components.
  - Experimentally obtain SFE and the ratio of each chemical component.
  - Extract the influence of various chemical components through multiple regression analysis.
- After obtaining the influence of each chemical component, calculate the amount of the effect of each chemical component in the time difference of CA.

The governing equation for the model treating chemically heterogeneous surfaces is the equation of Cassie [58] as it is shown in eq. (2.22). Cassie expressed the total energy of a chemically heterogeneous surface by using the area ratio of the energy of each chemical component. With this total energy, the total effective CA at the flat surface is calculated. The image of this equation is shown in fig. 2.16.

$$\begin{aligned} \sigma_L \cos\theta_{0c} &= a_1(\sigma_{S1} - \sigma_{S1L}) + a_2(\sigma_{S2} - \sigma_{S2L}) + \cdots \\ \cos\theta_{0c} &= a_1 \cos\theta_1 + a_2 \cos\theta_2 + \cdots \end{aligned} \tag{2.22}$$

where θ_{0c} is CA at a flat and chemically heterogeneous surface (hereafter it calls the effective CA), a_i is the area ratio of each chemical component. σ_{Si} is SFE of the solid of each chemical component. σ_{SiL} is the interfacial tension of the solid and liquid of each chemical component. θ_i is the CA of the flat and chemically homogeneous surface of each component.

The problem here is there are too many variables since σ_{Si} and σ_{SiL} are unknown. To calculate the CA from the effect of each chemical component, reducing

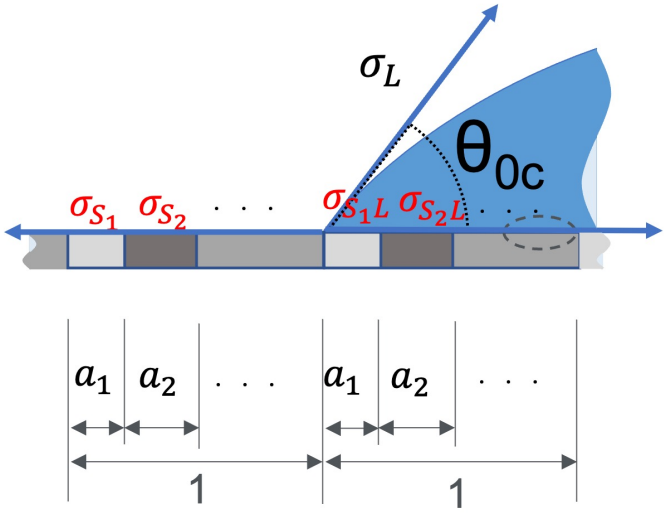

Figure 2.16: Image of Cassie's model: Each color in solid show the ratio of each chemical component.

the variables is needed by replacing σ_{SiL} with σ_{Si}. To replace these, the same methodology was used as the conventional way, which is using the model of Dupre [47] and model from Owen et al. [48]. However, the challenge here is that there is no expression of adhesive force for the chemically heterogeneous surface on the model of Dupre and Owen et al. since both equations are used in chemically homogeneous surfaces. Therefore, in this study, the expression of adhesive force for chemically heterogeneous surfaces is considered.

At first, the expression of SFE of chemically heterogeneous (effective SFE) of solid was considered. The idea is since the effective energy is derived from the area ratio of the energy of each chemical component in the equation of Cassie [58], and the interface of different chemical components' surface is perpendicular to the surface where contact to liquids, in this study, the effective SFE is expressed as eq. (2.23).

$$\sigma_{effS} = \sum_{i}^{n} a_i \sigma_{Si} \tag{2.23}$$

where σ_{effS} is effective SFE of solid.

Then, the expression of adhesion force for chemically heterogeneous surface is considered. At first adhesion force for each chemical is re-expressed. Then how to combine each chemical components is explained.

For adhesion force for each chemical is written by using the model of Dupre [47] and the model of Owen et al. [48] as shown in eq. (2.24), eq. (2.25), and eq. (2.26).

$$W_{Ai} = \sigma_{Si} + \sigma_L - \sigma_{SiL} \tag{2.24}$$

$$\sigma_i = \sigma_i^P + \sigma_i^D \tag{2.25}$$

$$W_{Ai} = 2\left(\sqrt{\sigma_{Si}^P \sigma_L^P} + \sqrt{\sigma_{Si}^D \sigma_L^D}\right) \tag{2.26}$$

where W_{Ai} is the adhesion force for each chemical component. σ_i, σ_i^P, σ_i^D are the total SFE and the polar part and dispersive part of the SFE for each chemical component, respectively. σ_{Si}^P, σ_{Si}^D are the polar part and dispersive part of SFE for the solid of each chemical component, respectively.

The idea for combining the adhesion force of each chemical components is using the idea from Fowkes [49], who introduces geometric mean to the dispersive part of SFE. Fowkes showed that the potentials from the elements below the interaction surface are summed up for calculating the energy of interaction, and this energy of interaction is in inverse proportion to the square of the distance. Since the horizontal contact area between solid and liquid is mm order and lateral effective area for SFE is several layers of molecules [49], therefore, in this study, the interaction forces in the vertical direction are only considered as shown in fig. 2.17.

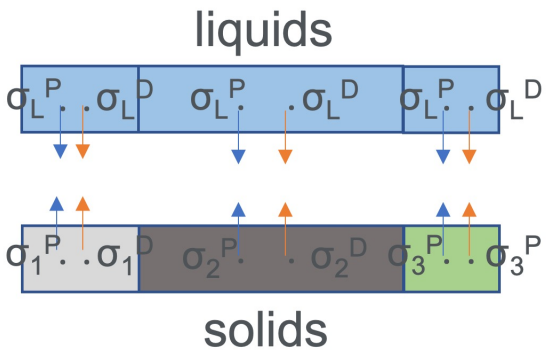

Figure 2.17: Image of the interface of heterogeneous surface: the different colors in solid shows different chemical components, the blue arrow shows force of polar part of each chemical components, the orange arrow shows force of dispersive part of each chemical components

In the end, the total adhesive force of a chemically heterogeneous surface is expressed in eq. (2.27).

$$W_{Ac} = \sum_i^n a_i W_{Ai} = \sum_i^n 2a_i \left(\sqrt{\sigma_{Si}^P \sigma_L^P} + \sqrt{\sigma_{Si}^D \sigma_L^D}\right) \tag{2.27}$$

where W_{Ac} is the effective adhesive force.

From eq. (2.22) and eq. (2.24), the effective CA (θ_{0c}) is expressed by the term of adhesion force and SFE of liquid as shown in eq. (2.28). From eq. (2.27), the term of adhesion force is expressed by the dispersive and polar part of SFE as shown in eq. (2.29).

$$\sigma_L \cos\theta_{0c} = \sum_i^n a_i W_{Ai} - \sigma_L \tag{2.28}$$

$$= \sum_i^n 2a_i \left(\sqrt{\sigma_{Si}^P \sigma_L^P} + \sqrt{\sigma_{Si}^D \sigma_L^D} \right) - \sigma_L \tag{2.29}$$

In the end, the relationship between the effective CA and the effect of chemical components is expressed in eq. (2.30) to eq. (2.32).

$$\frac{\sigma_L \, (cos\theta_{0c} + 1)}{2\sqrt{\sigma_L^D}} = \sum_i^n a_i \sqrt{\sigma_{Si}^P} \frac{\sqrt{\sigma_L^P}}{\sqrt{\sigma_L^D}} + \sum_i^n a_i \sqrt{\sigma_{Si}^D} \tag{2.30}$$

$$S_p \equiv \sum_i^n a_i \sqrt{\sigma_{Si}^P} \tag{2.31}$$

$$S_d \equiv \sum_i^n a_i \sqrt{\sigma_{Si}^D} \tag{2.32}$$

where S_p and S_d show the coefficient of the polar part and dispersive part for solid, respectively.

In eq. (2.30) to eq. (2.32), parameters of chemical components of material surface are expressed in S_p, S_d, a_i and square roots of the particular SFE for solid ($\sqrt{\sigma_{Si}^P}$,$\sqrt{\sigma_{Si}^D}$). The SFE is expressed in the form of a square root because this expressed value is linearly combined with S_p, S_d. Because of the linear combination with S_p, S_d, multiple regression analysis can be used to estimate the square root SFE. This will be expressed in next session.

To predict CA from chemical components by using this model, S_p, S_d, a_i, and square roots of SFE for solid are needed to evaluate. The image of the relationships of this model is shown in fig. 2.18. This figure shows that the measured CA (θ_W, or θ_{CB}) on the laser-textured surface is affected by both the topography and the chemical components. The topography effect is described by the Wenzel equation and Cassie-Baxter equation. Then measured CA is transformed to the CA at the flat surface (the effective CA (θ_{0c})). This CA at a flat surface is related to the chemical components via eq. 2.30. In this figure, the green color variables depend on

the liquid, and they are already known, the blue color variables are obtained from experiments, and red color variables are difficult to obtain from experiments then they are obtained from a multiple regression analysis.

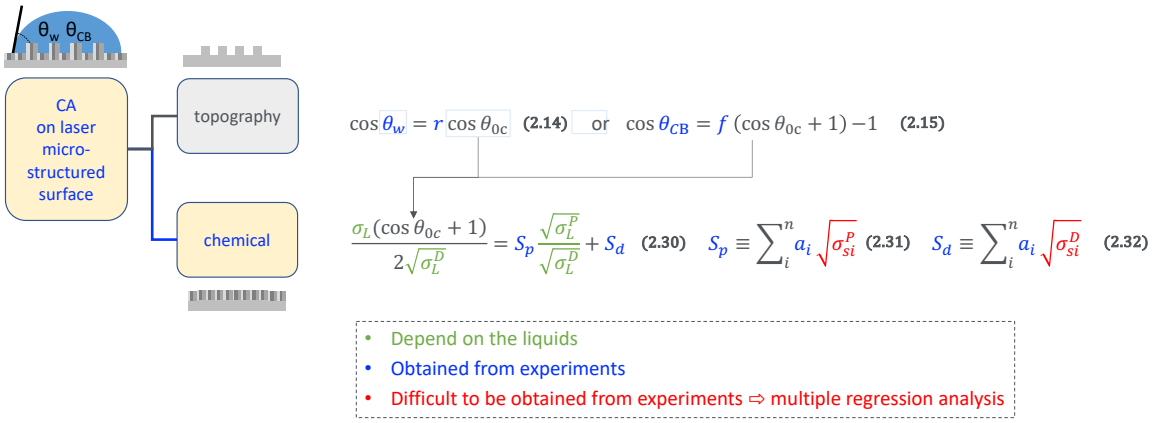

Figure 2.18: The sketch of the model: CA on laser structured surface is divided into topography effect and chemical effect: the green variables depend on the liquid, and they are already known, the blue variables are obtained from experiments, and red variables are difficult to obtain from experiments then they are obtained from a multiple regression analysis.

The value of S_p and S_d can be obtained by measuring the CA of different liquids on laser micro-structured surfaces and calculating CA for flat surfaces from eq. (2.14) or eq. (2.15) since the dispersive and polar parts of SFE of some liquids are already known. In this study, water and diiodo-methane are used as for the liquids. Since the diiodo-methane has only dispersive part as it is described in subsection 3.6.1, the coefficient of polar part in eq. (2.30) (S_p) becomes zero. Then S_p and S_d are obtained by solving the simultaneous equations. The image of these experiments and the equations are shown in fig. 2.19.

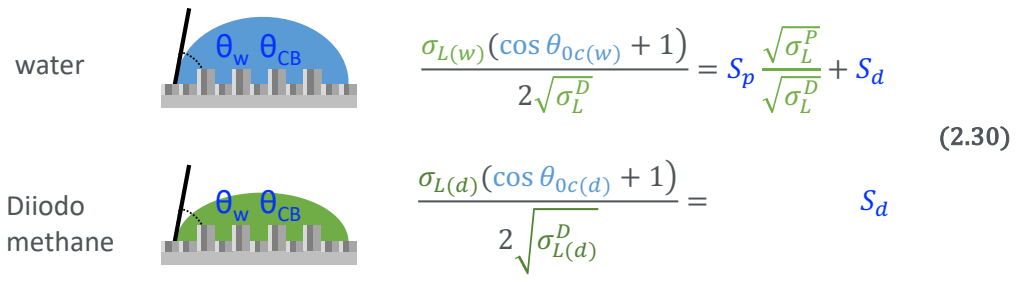

Figure 2.19: Image of the experiments for obtaining S_p, S_d:The green variables are known value from liquid. The w,d in subscript brackets indicate water and diiodo-methane. The blue variables are obtained from experiments.

The values of a_i can be obtained by measuring the concentrations of chemical components on the surface by XPS. The image of the experiments is shown in fig.

2.20. The height in the figure indicates the height per unit area of the structure. The colors in the figure indicate different chemical species. The width of the color in the figure indicates the percentage of that chemical species per unit area.

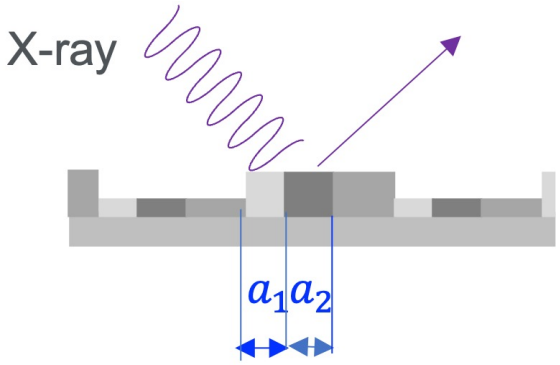

Figure 2.20: Image of the experiments for obtaining a_i :The height in the figure indicates the height per unit area of the structure.The colors in the figure indicate different chemical species. The width of the color in the figure indicates the percentage of that chemical species per unit area.

However, the values of square roots of the particular SFEs for solid are difficult to get from experiments. Therefore, a statistical approach is needed. Since S_p and S_d can be expressed as a linear sum of the square roots of the particular SFEs for solid as shown in eq. (2.31) and eq. (2.32), multiple regression analysis to approximate the square roots of the particular SFEs for solid was able to used.

Multiple regression analysis is a statistical technique that analyzes how multiple explanatory variables affect an objective variable. Specifically, it can analyze the relationship between multiple explanatory variables and one objective variable. Multiple regression analysis uses regression equations to model the relationship between the objective and explanatory variables. The regression equation represents the objective variable as a linear combination of the explanatory variables. This allows one to predict changes in the objective variable with changes in the explanatory variables. For multiple regression analysis, the equation of residual squared sum was used, as shown in eq. (2.33) and eq. (2.34). The image of the data set for the residual squared sum is shown in fig. 2.21.

$$R^p = \sum_j^k \left(S_{p(j)} - \left(a_{1(j)} \sqrt{\sigma_{S1}^P} + a_{2(j)} \sqrt{\sigma_{S2}^P} + \cdots + a_{n(j)} \sqrt{\sigma_{Sn}^P} \right) \right)^2 \tag{2.33}$$

$$R^d = \sum_j^k \left(S_{d(j)} - \left(a_{1(j)} \sqrt{\sigma_{S1}^D} + a_{2(j)} \sqrt{\sigma_{S2}^D} + \cdots + a_{n(j)} \sqrt{\sigma_{Sn}^D} \right) \right)^2 \tag{2.34}$$

where R^p, R^d are the polar and dispersive parts of the residual squared sum. The indicator j shows the number of the experimental data set.

$$R^P = \sum_j^k \left(S_{p(j)} - \left(a_{1(j)}\sqrt{\sigma_{s1}^P} + a_{2(j)}\sqrt{\sigma_{s2}^P} + \cdots + a_{n(j)}\sqrt{\sigma_{sn}^P} \right) \right)^2 \quad (2.33)$$

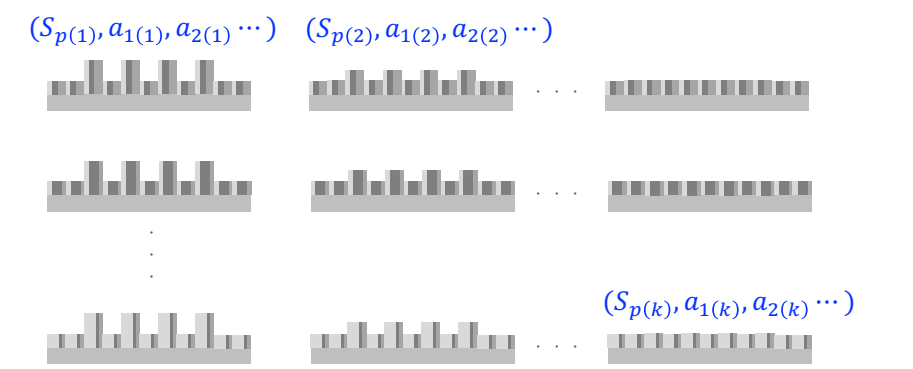

Figure 2.21: Image of the data set for the residual squared sum: Each image shows the various structures and the proportions of the various chemical components. The blue variables are obtained from the experiment. The red variables will obtained from multiple regression analysis.

To get the approximate value of the square roots of the particular SFEs, partial differentiation of the residual squared sum with respect to each square root of the particular SFEs is required to be small, as shown in eq. (2.35) and eq. (2.36).

$$\frac{\partial R^p}{\partial \sqrt{\sigma_{Si}^P}} = 0 \quad (2.35)$$

$$\frac{\partial R^d}{\partial \sqrt{\sigma_{Si}^D}} = 0 \quad (2.36)$$

To obtain approximate square roots of SFE, simultaneous equations of partial differentiation of residual squared sum need to be solved as shown in eq. (2.37) and eq. (2.38).

$$\begin{pmatrix} \sum_j^k a_{1(j)}^2 & \cdots & \sum_j^k a_{1(j)}a_{i(j)} & \cdots & \sum_j^k a_{1(j)}a_{n(j)} \\ \vdots & & \vdots & & \vdots \\ \sum_j^k a_{1(j)}a_{i(j)} & \cdots & \sum_j^k a_{i(j)}^2 & \cdots & \sum_j^k a_{i(j)}a_{n(j)} \\ \vdots & & \vdots & & \vdots \\ \sum_j^k a_{1(j)}a_{n(j)} & \cdots & \sum_j^k a_{n(j)}a_{i(j)} & \cdots & \sum_j^k a_{n(j)}^2 \end{pmatrix} \begin{pmatrix} \sqrt{\sigma_{S1}^P} \\ \vdots \\ \sqrt{\sigma_{Si}^P} \\ \vdots \\ \sqrt{\sigma_{Sn}^P} \end{pmatrix} = \begin{pmatrix} \sum_j^k a_{1(j)}S_{p(j)} \\ \vdots \\ \sum_j^k a_{i(j)}S_{p(j)} \\ \vdots \\ \sum_j^k a_{n(j)}S_{p(j)} \end{pmatrix} \quad (2.37)$$

$$\begin{pmatrix} \sum_j^k a_{1(j)}^2 & \cdots & \sum_j^k a_{1(j)}a_{i(j)} & \cdots & \sum_j^k a_{1(j)}a_{n(j)} \\ \vdots & & \vdots & & \vdots \\ \sum_j^k a_{1(j)}a_{i(j)} & \cdots & \sum_j^k a_{i(j)}^2 & \cdots & \sum_j^k a_{i(j)}a_{n(j)} \\ \vdots & & \vdots & & \vdots \\ \sum_j^k a_{1(j)}a_{n(j)} & \cdots & \sum_j^k a_{n(j)}a_{i(j)} & \cdots & \sum_j^k a_{n(j)}^2 \end{pmatrix} \begin{pmatrix} \sqrt{\sigma_{S1}^D} \\ \vdots \\ \sqrt{\sigma_{Si}^D} \\ \vdots \\ \sqrt{\sigma_{Sn}^D} \end{pmatrix} = \begin{pmatrix} \sum_j^k a_{1(j)}S_{d(j)} \\ \vdots \\ \sum_j^k a_{i(j)}S_{d(j)} \\ \vdots \\ \sum_j^k a_{n(j)}S_{d(j)} \end{pmatrix} \tag{2.38}$$

In the end, once the approximate value of square roots of SFE is obtained, CA at laser micro-structured surface will be predicted by using the concentrations of chemical components. To conduct this multiple regression analysis, the limit of this method is that the number of samples should be larger than the number of variables. Therefore, several numbers of samples are need to be laser processed and several wettability and chemical components should be measured.

In the end, for the first challenge (to identify the relationship between wettability (CA) and multiple chemical components), by extending the adhesive force, the equation which shows relationship between CA and multiple chemical components was developed. For using this equation to estimate the effect of each chemical component, the methods to obtain variables in the equations was suggested such as wettability experiments, XPS analysis, and statistical analysis (multiple regression analysis).

2.4.2 The model for analysis of time development

In the previous section, the equation for the relationships between CA and multiple chemical components was developed. In this subsection, in order to evaluate the change of CA over time, this relationship was used at different time points. Then the time development of CA and chemical components was discussed. The idea of this model is that CA is changed by chemical effects. Therefore, to see the effect of chemical components on CA, the effective CA(θ_{0c}) shown in eq. (2.30) was organized in terms of the ratio of chemical components (a_i) described as eq. (2.39).

$$\begin{aligned}\theta_{0c} &= \arccos\left\{\frac{2}{\sigma_L}\left(S_p\sqrt{\sigma_L^P}+S_d\sqrt{\sigma_L^D}\right)-1\right\}\\ &= \arccos\left\{\frac{2}{\sigma_L}\left(\sqrt{\sigma_{S0}^P}\sqrt{\sigma_L^P}+\sqrt{\sigma_{S0}^D}\sqrt{\sigma_L^D}\right)a_0\right.\\ &\qquad +\frac{2}{\sigma_L}\left(\sqrt{\sigma_{S1}^P}\sqrt{\sigma_L^P}+\sqrt{\sigma_{S1}^D}\sqrt{\sigma_L^D}\right)a_1\\ &\qquad \left.\cdots-1\right\} \qquad (2.39)\\ &= \arccos\left(k_0a_0+k_1a_1+k_2+\cdots-1\right)\\ &= \arccos\left(C_m\right)\end{aligned}$$

where

$$k_i \equiv \left(\sqrt{\sigma_{Si}^P}\sqrt{\sigma_L^P}+\sqrt{\sigma_{Si}^D}\sqrt{\sigma_L^D}\right) \qquad (2.40)$$

$$C_m \equiv k_0a_0+k_1a_1+k_2+\cdots-1 \qquad (2.41)$$

where i is the number for kinds of chemical components. Here, k_i shows the strength of the effect of each chemical component; for example, when k_i is bigger than k_j then, the the effect of chemical i on CA is more effective than chemical j. C_m is the sum of the effect from all chemical components.

Next, to consider the effect of the chemical components on the change of CA over time, the time differences in these variables ($\Delta\theta_{0c}$, Δa_i, ΔC_m) were considered. This is because the difference in variables reduces the change in scale. To estimate the effect of a certain chemical species (a_i) in the CA difference ($\Delta\theta_c$), D was defined as shown in eq. (2.42). D is the CA difference ($\Delta\theta_c$) multiplied by the fraction of the effect of certain chemical components ($k_i\Delta a_i$) in the sum of the effect of all chemical components (ΔC_m). This provides a quantitative estimation of the contribution of each chemical species in CA.

$$D_{m(d_n-d_m)(i)} \equiv \Delta\theta_{0c(d_n-d_m)}\frac{k_i\Delta a_{i(d_n-d_m)}}{\Delta C_{m(d_n-d_m)}} \qquad (2.42)$$

where d_n and d_m show the measured day of each value. By using this model, the difference of CA is compared with different days. In addition, the effect of each chemical component is described quantitatively.

Chapter 3

Experimental setup and techniques

3.1 Material

In this study, mainly stainless steel sheets (SUS 304L, Hans-Erich Gemmel & Co. GmbH) with a dimension of 50x50 mm^2 and a thickness of 1 mm were used. The chemical composition of stainless steel is given in tab. 3.1. The surfaces were polished to optical quality (mirror-polished surface). To reduce contaminations from the air on the sample, every sample was cleaned with isopropanol in an ultrasonic bath for 15 minutes and rinsed with distilled water before the laser process.

Table 3.1: Chemical components of SUS 304 [59]

chemical components	C	Cr	Ni
ratio (%)	0.06	17.50	8.5

3.2 Experimental setup for laser micro-structuring

The samples were micro-structured with an ultra-short pulse (USP) laser system (Hyper-Rapid 25, Coherent Kaiserslautern GmbH) with a pulse duration of 10 ps and a wavelength of 532 nm. The laser system was integrated into a high-precision 5-axes micro-machining workstation equipped with a galvanometric scanner system. For the experiments, a telecentric F-Theta optic with a focal length of 100 mm was used, resulting in a spot diameter in the focal plane is 9.2 μm. The laser processing was done in ambient air. The system image is shown in fig. 3.1

To generate large-area morphology since the laser beam spot size is small, the laser beam was scanned over the surface with a galvanometric scanner system. The scanning strategy was a raster scan with a hatching distance. The scanning

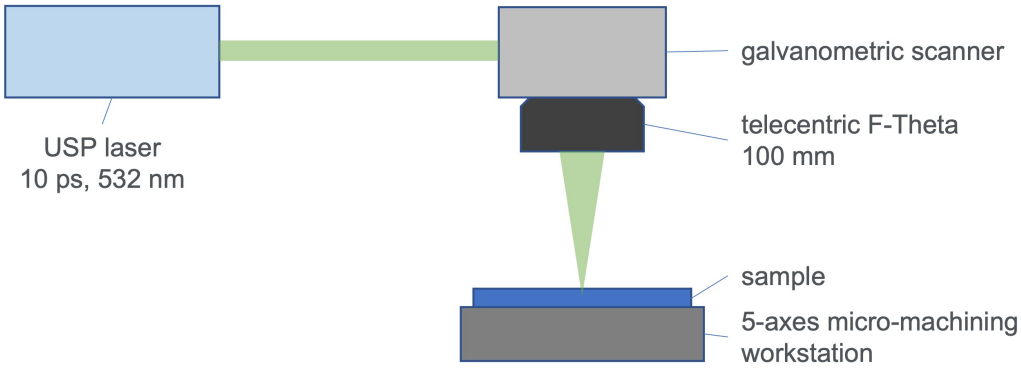

Figure 3.1: The experimental setup for laser micro-structuring

direction was changed by 90 ° for each single surface scan. The scan strategy is shown in fig. 3.2. The experimental conditions e.g.laser beam power, spatial pulse overlap, time interval of pulse to pulse, and scan number, were adjusted for each structure.

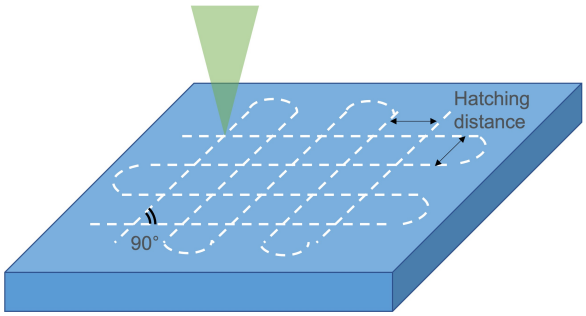

Figure 3.2: The image of the scan field: the white dashed line is the laser scanned line, the distance between parallel lines is the hatching distance.

3.3 Post-process and Storage conditions

For considering the chemical properties effect, different post-processes and storage conditions were examined since several researchers showed [3, 54] that the different post-processes lead to different CA of water, which means different chemical properties. In this study, 2 different post-processes and 2 different storage conditions for each structure were examined.

First, all samples were air-blow cleaned immediately after laser processing. Regarding post-processing, Ngo et al. [60] reported a hydrophilic transition on an aluminum surface by boiling water treatment. They suggested highly polar AlOOH and Al_2O_3 created by boiling can make a super hydrophilic surface on the aluminum. For stainless steel, Rajab et al. [54] showed that when the stainless steel sample was boiled, the CA of water kept a low degree for a long term. Therefore, to change

the chemical properties to be hydrophilic, half of the samples were boiled in hot distilled water for 8 hours. To see the effect of the post-process, half of the samples were not boiled.

Regarding store conditions, Al foil is said to be able to adsorb water, organic, and inorganic matter [61, 62]. It could prevent the absorption of hydrocarbon from ambient air which is one of the reasons for the increase of CA [55]. Therefore, half of the samples were covered with aluminum (Al) foil to prevent air contamination. To see the difference of the storage condition, half of the samples were stored in ambient air. The summary of the post-process and storage conditions of samples is shown in tab. 3.2.

Table 3.2: Combination of post-processing and conservation conditions

No.	post-process	store conditions
No.1	Air blow	Al foil
No.2	Air blow	ambient air
No.3	boiling	Al foil
No.4	boiling	ambient air

3.4 Characterization of physical properties

As it is explained in section 2.2, the laser micro-structured surface is a rough surface. The stable CA on this rough surface is different from the stable CA on the flat surface. This effect of the rough surface is calculated by the structure parameters r, f as shown in eq. (2.14) and eq. (2.15). Therefore the characterization of a laser-structured surface is needed.

3.4.1 SEM

As it is shown in section 2.1.2, laser micro-structured surface has nano- and micro-structures. To know the surface morphology (flat or hierarchical (nano- micro-) structure) at laser processed surface, since the scanning electron microscope (SEM) has a high resolution in the horizontal direction (less than nm), SEM (EVO MA10, Zeiss) was used. An SEM is a type of electron microscope that produces images of a sample by scanning the surface with a focused beam of electrons. The electron beam is scanned in a raster scan pattern, and the position of the beam is combined with the intensity of the detected signal to produce an image. The example of the SEM image is shown in fig. 3.3.

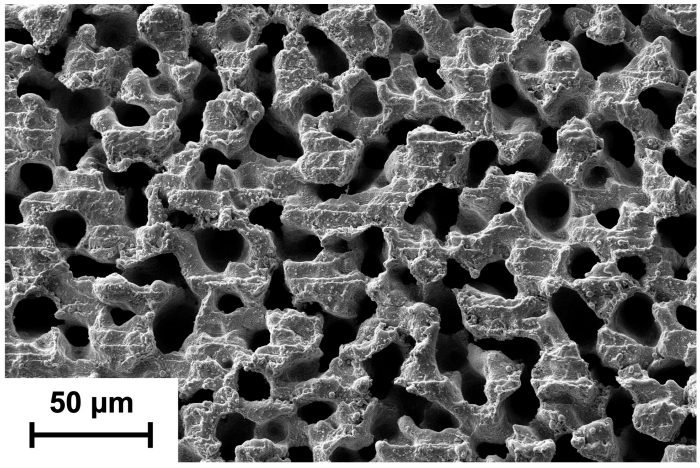

Figure 3.3: The SEM image of surface morphology of sponge-like structure

However, the depth of field of SEM depends on the acceleration voltage, NA of lens, and magnification, and is large compared to other techniques e.g. optical microscopes. For example, at a magnification of 1000 and acceleration voltage of 10kV, the depth of field is around 100 μm. Therefore, to obtain the structure parameters such as r and f, other techniques were also used.

3.4.2 Confocal microscope

Confocal microscopy is an optical imaging technique for increasing the optical resolution and contrast of a micrograph by means of using a spatial pinhole to block out-of-focus light in image formation. Capturing multiple two-dimensional images at different depths in a sample enables the reconstruction of three-dimensional structures within an object. With these systems, vertical and horizontal resolutions in the range of 0.1 μm are achieved in a wide horizontal area, for example, 200x200 μm^2. Therefore, to have a structure parameter r value of the surface a confocal microscope (Zeiss smart proof 5, Carl Zeiss AG) was used. The image of the confocal microscope is shown in fig. 3.4. From these confocal microscope measurements, R_a, RS_m values were obtained. r represents the ratio of increased area to projected area. Here, to calculate the increased area ratio, the roughness on a relatively flat surface was approximated as a triangular waviness. The length of the bottom triangular waviness was assumed to be RS_m, and the height was assumed to be $2R_a$. The area of increase was therefore calculated using the following eq. (3.1).

$$r = \frac{\sqrt{(2R_a)^2 + (\frac{RS_m}{2})^2}}{\frac{RS_m}{2}} \tag{3.1}$$

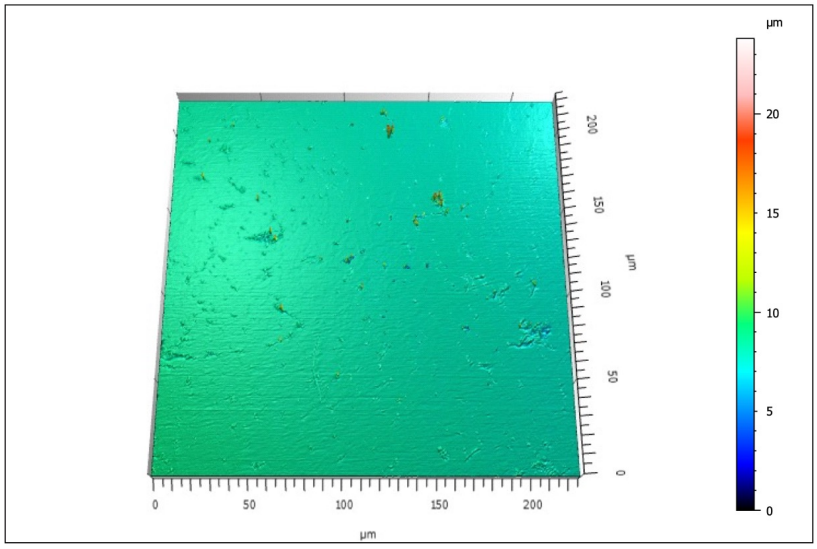

Figure 3.4: The example of a confocal microscope image of reference surface

Since this technique uses the reflection of light (laser) from the surface, the reflection signal from deep holes or mushroom-like pillars cannot be detected. For example, to measure the depth of the bottom of the hole, sufficient light must reach the bottom of the hole and the reflected light must return. Therefore, for example, if the hole diameter of a sponge-like structure is about 10 μm and NA is about 0.5, the limit is limited to about 20 μm at most. Fig. 3.5a shows the cross-section image of the sponge-like structure by focus ion beam (FIB).

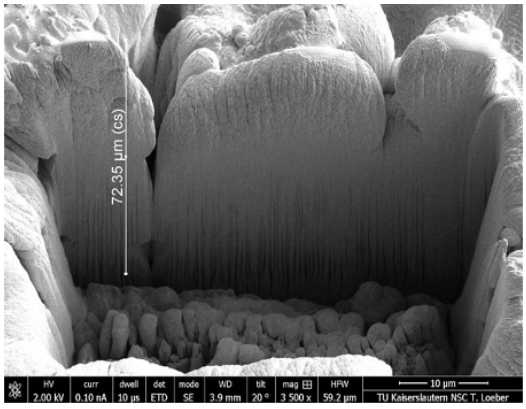

(a) SEM image after cut by FIB

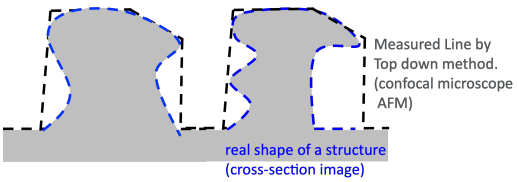

(b) Scketch of cross-section

Figure 3.5: The cross-section image of sponge-like structure: ((b) blue dashed line shows real shape of structure, black dashed line shows measured shape by top-down measurement methods (e.g. confocal microscope))

According to this, the sponge-like structure has more than 50um hole depth. In addition, the sponge-like structure has mushroom-like pillars, therefore top-down measurements are not suitable for measuring hole surface area. Therefore this technique was used only on a relatively smooth surface compared to a laser micro-

structured surface.

3.4.3 Cross-section image

To know the topography of the structure, especially very complex structures like a sponge-like structure, the cross-section image technique is used. However, FIB has a limit to having a large area and is also a time-consuming method, therefore other methods were considered. To obtain a cross-section image, the sample was cut into small pieces by laser, then small pieces were embedded in hardened resin. Then, the cut surface was polished with the polishing machine until it had a mirror-like surface. Then, a cross-section image was obtained by optical microscope. An optical microscope has a horizontal resolution around an order of μm in a wide area (for example 1x1mm^2). By using the image processing software (Image-J [63]), the outline of the structure is obtained as shown in fig. 3.6a, fig. 3.6b. From this outline, the structure parameter r, f for the complex structure surface was calculated. r is calculated by the length of the counter structure (blue line in fig. 3.6b) divided by the length of the flat surface (green line in fig. 3.6b). f is calculated by the length of the top of the pillars (orange line in fig. 3.6b) divided by the length of the flat surface. (green line in fig. 3.6b) In this, study, the orange line was the circumference of the point of maxima among the pillars at least 90% of the height of the tallest pillar.

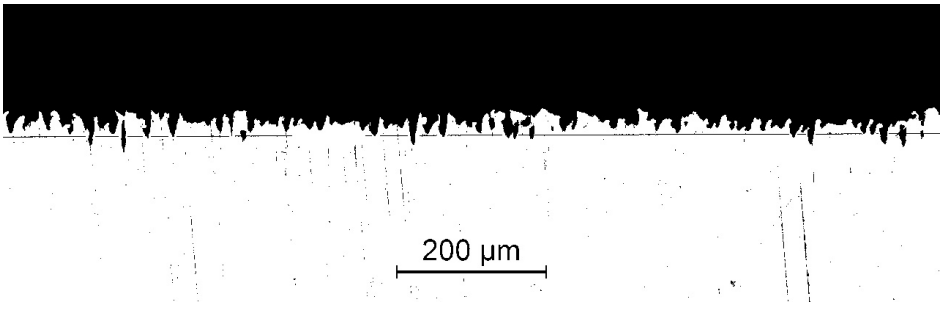

(a) The binary image of sponge-like structure

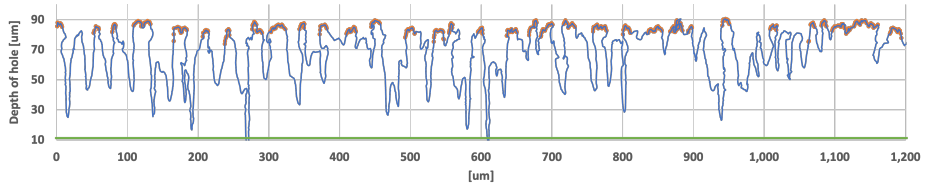

(b) The outline of sponge-like structure: the blue line is the contour of stochastic structure, the green line is the length of the flat surface, the orange line is the length of the top of the pillars.

Figure 3.6: The cross-section image of sponge-like structure

The summary of characterization techniques is shown in fig. 3.3.

Table 3.3: The comparison of the measurements methods for physical properties

method	SEM	confocal microscope	cross-section image + optical microscope
resolution (xy)	few nm	0.2 0.4 μm	0.5 μm
resolution (z) or depth of focus	- few 100 μm	0.1 μm -	- few μm
aim of use	to see the nano- micro- structure	to obtain 3D profile of micro- structure	to obtain complex micro- structure

3.5 Characterization of surface chemistry

As it is explained in section 2.2, the laser-structured surface is a chemical heterogeneous surface. This chemical components' effect is one of the reasons for the change of CA. Therefore the characterization of laser-structured surfaces over time is needed.

3.5.1 XPS

It is said that wettability is affected by the chemical components of the outermost of the surface. Therefore, a technique that can measure the surface chemical components is needed. Among the several measurement techniques as shown in the tab. 3.4, the X-ray Photoelectron Spectroscopy (XPS) can measure the outermost of the chemical components on the surface (detection depth is oder of nm). Therefore, for the chemical properties evaluation, XPS (Axis Nova, Kratos Analytical. Ltd./ GB) was performed on the laser micro-structured area as well as on the reference surface to measure the concentration of the chemical components. XPS is a surface-sensitive quantitative spectroscopic technique based on the photoelectric effect that can identify the elements that exist within a material (elemental composition) or are covering its surface, as well as their chemical state and the overall electronic structure and density of the electronic states in the material.

In this thesis, the following conditions of measurements were used. The working pressure was lower than 10^{-8} mbar in the analyzing chamber. Since it is reported that the vacuum chamber has changed the CA, it is necessary to set the same experimental conditions of measurements. In order to measure the chemical properties of all kinds of samples at the same time and same vacuum condition, all samples were inserted inside the analyzing vacuum chamber of the XPS at the same time. The sample was stored while all other sample was measured. The storage time is 24 hours, including the time of vacuuming and venting.

Table 3.4: The comparison of technique of chemical components

method	XPS	EDX	Raman
probe	photoelectron	X-ray	laser
measurement material	chemical element chemical bond	chemical element	molecular structure
sensitivity	0.1 at%	1 at%	1 wt%
detection depth	few nm	few μm	μm
minimum field of measurement	few 100 μm ϕ	few μm^2	few μm^2

From the peak area of photoelectron lines, relative concentrations of the elemental species at the surface were determined. Carbon, oxygen, nitrogen, chromium, iron, calcium, magnesium, nickel, and silicon were detected on the sample surface. In addition, different chemical binding states of the dominant elements like carbon, oxygen, nitrogen, chromium, and iron were identified via the chemical shift of their most prominent photoelectron line by high-resolution core-level spectra. By a detailed deconvolution of the atomic lines, quantitative ratios of the contributing chemical binding states were derived. The example of a profile of XPS is shown in fig. 3.7. In tab. 3.5, the employed electron binding energies for the chemical binding states of detected elements are summarized.

Table 3.5: Used electron binding energies for the deconvolution of atomic core level spectra, according to different chemical binding states [64, 65].

chemical component	electron binding energies	detected elements
Carbon C 1s	285.0eV	C-C(C-H)
	286.5eV	COC
	288.5eV	O=C-O, O-C-O
Oxygen O 1s	530eV	FeO, Fe_2O_3, CrO_3
	531.5eV	Cr_2O_3
	532.8eV	Org. O*=C-O, Org. C-O, C-OH, O=C-O*
Nitrogen N 1s	369.8eV	Metal Nitrides
	400eV	C-N, C-NH_2
Chromium Cr 2p	574eV	Metal
	577eV	Cr_2O_3
	579eV	CrO_3
Iron Fe 2p	707eV	Metal
	709.4eV - 710.8eV	Oxide

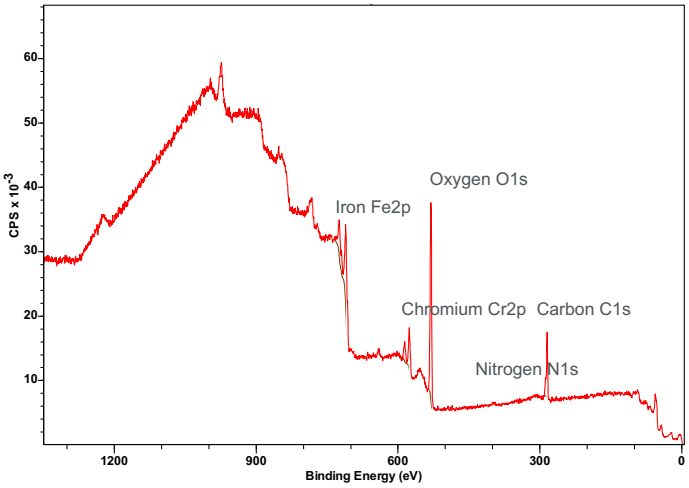

(a) The XSP spectra from 0 to 1300 eV: including the peak of Fe 2P, Oxygen O 1s, Chromium Cr 2p, Nitrogen N 1s, Carbon C 1s

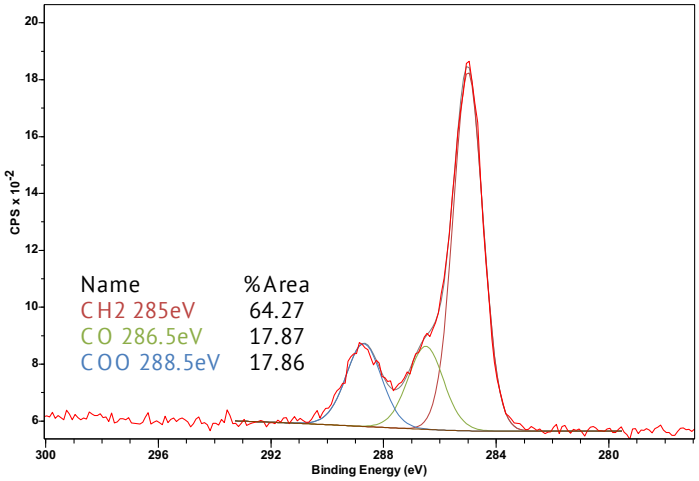

(b) High-resolution core-level spectra of carbon C 1s

Figure 3.7: The example of XPS spectra

3.6 Characterization of wettability

3.6.1 Contact angle

CA is measured by an image from the drop of a liquid on the sample surface by a drop shape analyzer device (DSA30, Krüss GmbH) with the liquid of droplet of 4 μl. The image of the liquid on the sample is shown in fig. 3.8. From this image, the boundary of the drop shape is detected by the software, and the contact angle is calculated. The measurements were taken 3 times in the same area. CA for different kinds of liquid was used for investigating the polar part and dispersive part of SFE as it is shown in chapter 2. In this study, water, diiodo-methane, and ethylene-glycol were used. These liquids were chosen due to their known and very

different dispersive and polar part of SFE. The dispersive and polar part of water are 21.8 mN/m and 51.0 mN/m [48], dispersive and polar part of diiodo-methane are 50.8 mN/m, 0 mN/m [66] dispersive and polar part of ethylene-glycol are 26.4 mN/m, and 21.3 mN/m [66].

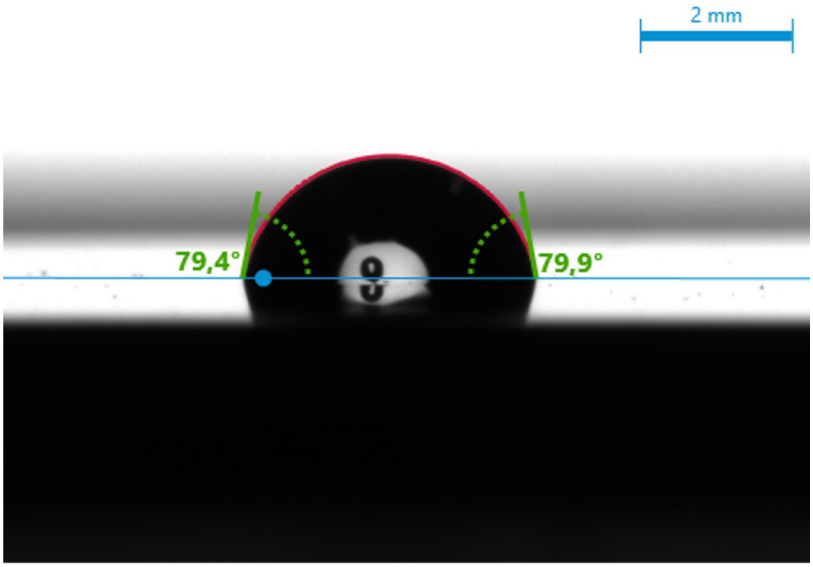

Figure 3.8: The image of drop shape by analyzer device: The blue line is the surface height, the red line is the contour of the droplet, the green line is the contact angle.

Chapter 4

Physical properties by USP laser processing

The model developed in section 2.4 requires multiple physical surface topographies and chemical surface states to know the chemical effects of time variation of CA. As a physical surface topography, the sponge-like structure is of interest because CA on sponge-like structures can be super-hydrophobic from super-hydrophilic over time. While for creating sponge-like structures in industrial applications (e.g., wires for medical devices), heat accumulation should be avoided to prevent the bending of the sample.

However, the growth mechanism of a sponge-like structure is still under debate and roughly divided into two groups (caused by reflection or heat accumulation) as shown in section 2.1.3. Regarding the boundary of the growth mechanism of a sponge-like structure, Zuhlke et al. [32] suggest that laser fluence is one of the indicators. This is because when the laser fluence is high with the same pulse repetition rate, heat accumulation is more likely to happen.

However, the heat accumulation can be low even if in the high fluence when the pulse repetition rate is low. Thus, the boundary of the growth mechanism of sponge-like structures is not well known yet.

Therefore, for aiming to create sponge-like structures on industrial applications, knowing the boundary of this growth mechanism of sponge-like structures is needed. In this study, in order to see the boundary of the growth mechanism of a sponge-like structure, the fluence is varied, and heat accumulation is varied by changing the time interval of pulses with the same spatial pulse overlap.

4.1 Experiment

The material in this section is the stainless steel plate which was described in chapter 3. Before and after of laser process, the sample was cleaned by isopropyl alcohol.

The experimental setup for creating morphology is described in chapter 3. The laser process area is 1x1 mm^2.

To divide the experimental condition as a heat accumulation condition and non-heat accumulation condition, the time interval of pulses and peak fluence (pulse energy) are varied. The time interval of pulses is changed by changing the repetition rate of the laser. Prior to the experiment, the range of the repetition rate is chosen from the calculation results of the time profile of the temperature at the center point of the beam after a single pulse is irradiated on the surface. fig. 4.1 shows the time profile of increased temperature (ΔT) at the center point of the beam after a single pulse is irradiated on the surface at two different pulse energies. The light blue horizontal line is the range of temperature where loses the strength of stainless steel (c.a. 300 K). According to fig. 4.1, ΔT decreases over time. Therefore, as one of the conditions not for heat accumulation, the time interval of pulses was set to 25 μs, which corresponds to the experimental condition of 40 kHz of the repetition rate of the laser. On the other hand, if the time duration after the laser pulse is short, ΔT remains high temperature, even over the temperature where loses the strength of stainless steel. Therefore, as the conditions for heat accumulation, 2.5 μs and 1 μs (as an extreme condition for it) were set, which correspond to the experimental condition of 400 kHz and 1000 kHz of repetition rate. In order to see the effect of the time interval of pulses even in the same range of total energy per area, the number of pulses per area (or spatial pulse overlap) was kept the same at each repetition rate by changing the scanning speed.

Additionally, according to fig. 4.1, when the pulse energy is low, even at a short time interval of pulses, increased temperature ΔT is low (c.a. 50 K). Therefore, to divide the heat accumulation condition and non-heat accumulation condition, various pulse energy (peak fluence) was also examined. The detail of the experimental condition is summarized in tab. 4.1. After creating the surface, the morphology was measured by SEM.

4.2 Results and discussion

The morphologies measured by SEM at different laser conditions are summarized in fig. 4.2, 4.3, and 4.4 for time intervals of pulses of 1 μs, 2.5 μs, and 25 μs,

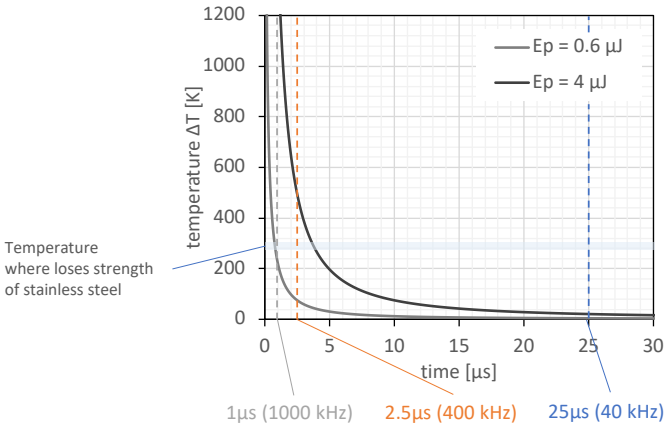

Figure 4.1: The time profile of increased temperature from a single pulse irraditation at the center point of the beam

Table 4.1: Experimental conditions

time interval of pulses	25 μs	2.5 μs	1 μs
repetition rate of laser	40 kHz	400 kHz	1000 kHz
scan speed	100 mm/s	1000 mm/s	2500 mm/s
pulse overlap	72.5 %		
peak fluence	0.4 to 30.6 J/cm^2		
scan number	1 to 101		

respectively. The vertical axis shows each fluence and the horizontal axis shows the scan number. According to fig. 4.2, 4.3, and 4.4, at all conditions with high peak fluence and high scan number, the bumpy structure appeared.

To see the relationship between heat accumulation conditions and morphology, the saturation temperatures (T_{sat}) at the center point in the laser scanning area for each laser condition were calculated. To obtain saturation temperatures for each experimental condition, a model described in section 2.1.3 was used. Additionally, the critical saturation temperature for forming a bumpy structure at stainless steel (T_{crit}) was referred from the same paper and is set to 607 °C. Fig. 4.5 shows the calculated results of saturation temperature at each laser condition. The blue horizontal line is the critical saturation temperature for bumpy structures. According to fig. 4.5, for conditions of all time intervals of pulses, when the peak fluence is small (lower than the green vertical dashed line), there is no bumpy structure formed. On the other hand, in the high peak fluence range (higher than the green vertical dashed line), the bumpy structures were formed. However, the heat accumulation condition is different from each time interval of pulses' conditions. According to fig. 4.5, the saturation temperature at the condition of the time interval of pulses of 1 μs and 2.5 μs exceeds the critical saturation temperature for bumpy structures. How-

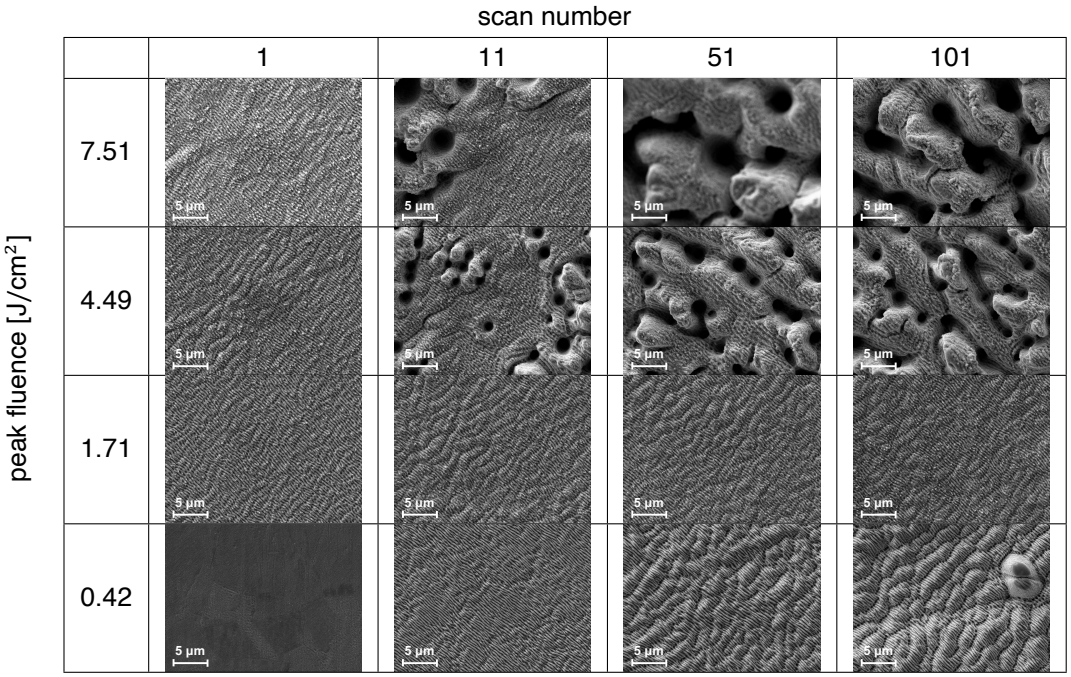

Figure 4.2: SEM image of each experimental condition at repetition 1 μs

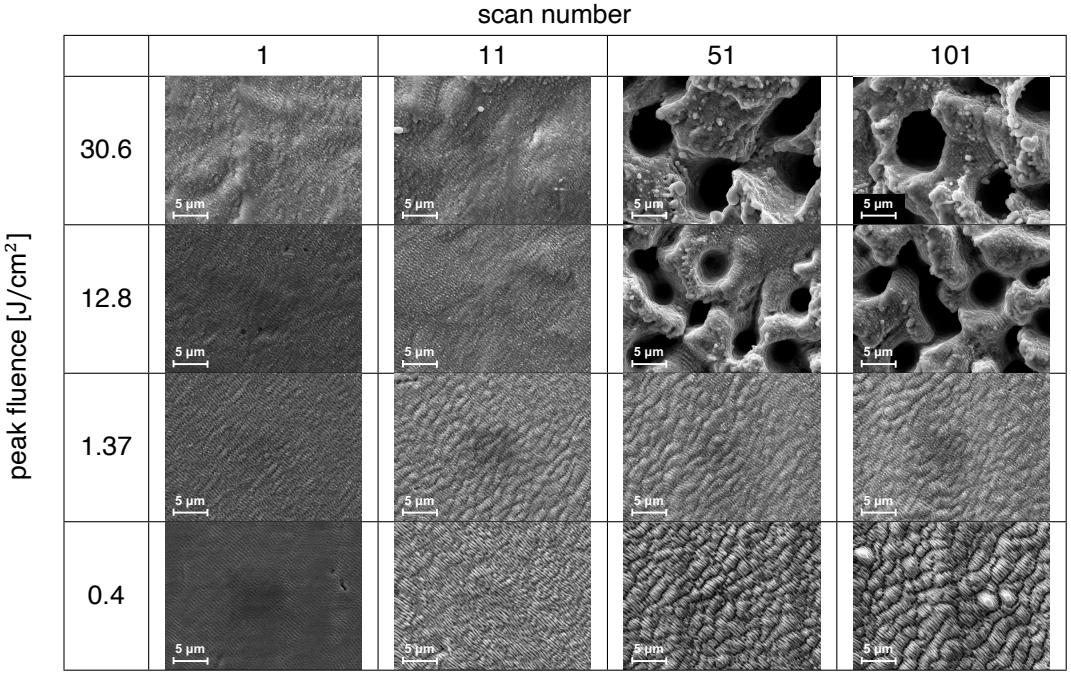

Figure 4.3: SEM image of each experimental condition at 2.5 μs

ever, the saturation temperatures at the conditions with the time interval of pulses of 25 μs do not exceed the critical saturation temperature for bumpy structures. These results suggest that there is another explanation is needed for the formation of the bumpy structure instead of critical saturation temperature. According to fig. 4.2, 4.3, and 4.4, when the bumpy structure at the time interval of pulses of 25 μs is compared to the one at time interval of pulses of 2.5 μs and 1 μs, lots of debris on

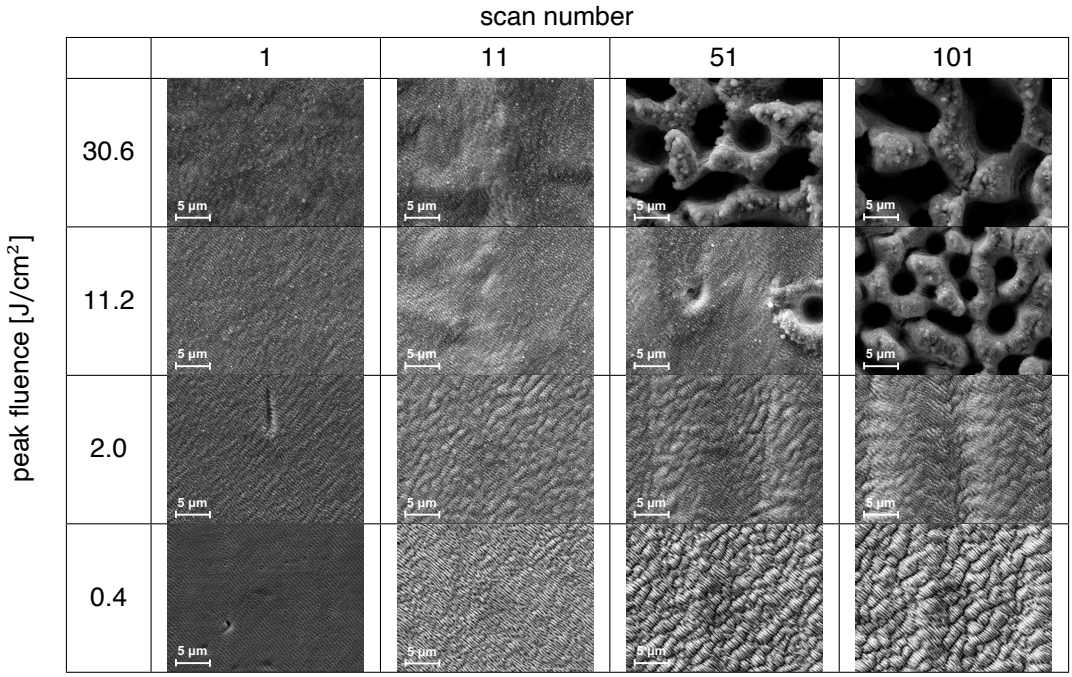

Figure 4.4: SEM image of each experimental condition at 25 μs

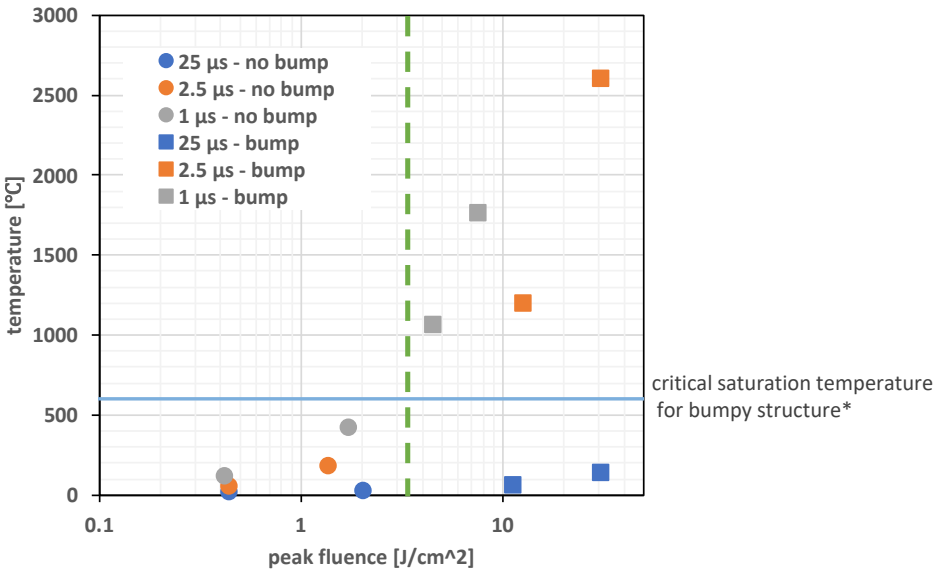

Figure 4.5: The results of saturation temperature at each experimental condition. Circle points show the condition for not bumpy structures, and square points show the conditions for bumpy structures. The critical saturation temperature for the bump is shown in the blue line and referred from the paper [23] The green line is the approximate fluence value for the generation of a sponge-like structure in this experiment condition.

top of the bumpy structure can be seen at the time interval of pulses of 25 μs. On the other hand, there is less debris, and LIPSS can be seen on the top of the bumpy structure at time interval of pulses of 2.5 μs and 1 μs. This result suggests that the growth mechanism of a bumpy structure is different at the time interval of pulses of 25 μs and at the time interval of pulses of 2.5 μs and 1 μs. For the future, further

experiments are needed, for example, the cross-section image cut by a focused ion beam (FIB), and then the oxidation states of bumpy structures are needed to be studied.

One of the ideas of the indicator for the boundary of the growth mechanism of a sponge-like structure is to use analogies of the mechanism of incubation effect in laser-induced damage threshold. The incubation effect is that the laser-induced damage threshold can be changed depending on the pulse train condition, such as the number of pulses per area and the time interval between laser pulses (pulse repetition rate of the laser). According to Sun et al. [67], the incubation effect occurs through two different mechanisms. One is absorption changes caused by the formation of surface ripples. Another one is critical energy changes caused by heat accumulation. According to the results from Sun et al. [67], the dominance of either mechanism can be changed by changing the time interval of pulses at the same spatial pulse overlap. Therefore, one of the hints for discussing the boundary of the mechanism for bumpy structure might be the incubation effect in different time interval of pulses' conditions. Therefore, which incubation mechanism is dominant at the different time interval of pulses is studied. To obtain the dominance of the incubation mechanism, the equation from Sun et al. [67] was used. The equation for the model is shown in eq. (4.1).

$$F_{th,Sun(N_a)} = \frac{F_{th,N_a=1} - \left[F_{th,N_a=1} - F_{th,N_a\to\infty}\left(1+\frac{\alpha}{\alpha_0}\right)\right]\left[1-e^{-\gamma F(N_a-1)}\right]}{1+\frac{\alpha}{\alpha_0}\left[1-e^{-\beta F(N_a-1)}\right]} \quad (4.1)$$

where N_a is the number of pulses per area, $F_{thN_a=1}$, is the damage threshold at a single pulse, $F_{th,N_a\to\infty}$ is the damage threshold at high numbers of pulses per area, α is the absorption coefficient during pulse train, α_0 is initial absorption coefficient, γ is a coefficient for the pulse induced change of critical energy density, β is a coefficient for the pulse induced change of absorption coefficient. When the experimental results are fitted by eq. (4.1), fitting parameters are α/α_0, γ and β. When $\gamma > \beta$, the incubation mechanism is absorption dominant, and when $\gamma < \beta$, the incubation mechanism is heat accumulation dominant. Therefore, the laser-induced damage threshold at each time interval of pulses conditions is obtained by the method given by Liu et al. [68]. In order to obtain fitting parameters in eq. (4.1), laser-induced damage threshold at different numbers of pulses per area was examined. In this experiment, the number of pulses per area was varied by changing the scan speed, as shown in eq. (4.2).

$$N_a = \frac{1}{1-\frac{PO}{100}} \quad (4.2)$$

where PO is spatial pulse overlap. The detail of the experimental condition is summarized in tab. 4.2.

Table 4.2: Experimental conditions for incubation

time intervals of pulses	25 μ m	2.5 μ m	1 μ m
repetition rate	40 kHz	400 kHz	1000 kHz
number of pulse per area	1 to c.a. 1000		
(spatial pulse overlap)	(single, PO 56% to 99.9%)		
peak fluence	0 to over 10 J/cm^2		

The results of damage threshold vs number of pulses per area at the different time interval of pulses' conditions are shown in fig. 4.6. After having experimental data, data were fitted with eq. (4.1). The parameters after fitting are shown in tab. 4.3.

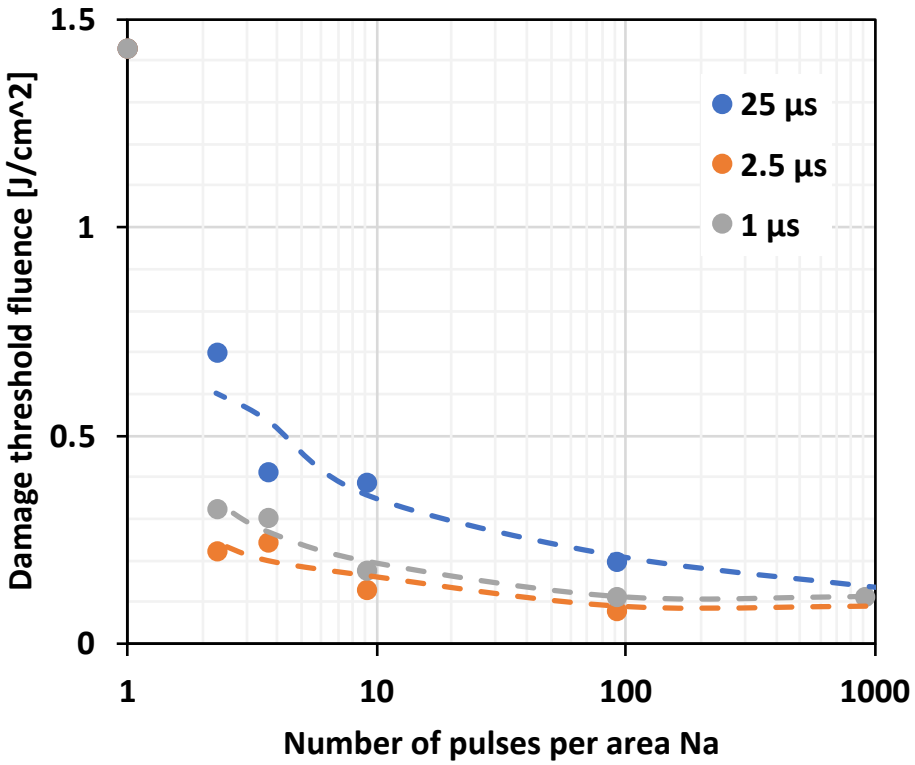

Figure 4.6: The results of laser-induced damage threshold at different numbers of pulses per area. Experimental data (dots) are fitted with the incubation model from Sun et al. [67](dashed line)

According to tab. 4.3, at only the time interval of the pulse of 25 μ m, γ is larger than β. In this time interval of pulses' range, the incubation mechanism is the absorption dominant. While at the time interval of pulses of 2.5 μs and 1, γ is smaller than β. Therefore, in this time interval of pulses' range, the incubation mechanism is the heat accumulation dominant. The trend in the difference in the dominance of

Table 4.3: The results of fitting parameters in the model based on Sun et al. [67].

time intervals of pulses	25 μm	2.5 μm	1 μm
$\Delta\alpha/\alpha_0$	2.29	3.95	2.17
γ	1.77	0.92	0.97
β	0.04	80.5	80.5
	$\gamma > \beta$	$\gamma < \beta$	$\gamma < \beta$

the incubation mechanism is the same as the trend in the difference of saturation temperature (below or above critical saturation temperature). Therefore, this result gives an idea that the boundary of the mechanism for bumpy structures might be predictable by the incubation model. For a better understanding of the mechanism of creating a bumpy structure at 25 μs, further experiments are needed.

The results give an idea of the boundary of the heat accumulation temperature model and also give an idea of process windows for sponge-like structures. With using this knowledge, in further experiment, sponge-like structures will be created.

4.3 Conclusion

In this chapter, as a physical surface topography, the sponge-like structure is of interest because CA on sponge-like structures can be super-hydrophobic from super-hydrophilic over time. For aiming to create sponge-like structures in industrial applications in the future, knowing the boundary of this growth mechanism of sponge-like structures is needed. In this study, in order to see the boundary of the growth mechanism of a sponge-like structure, the fluence is varied, and heat accumulation is varied by changing the time interval of pulses with the same spatial pulse overlap.

In the end, the process windows of the sponge-like structure were discussed. From this experiment, to obtain the sponge-like structure, the results that the peak intensity needs to be in the phase explosion range were found.

In addition, The boundary of the growth mechanism of a sponge-like structure is discussed with the idea of laser damage threshold incubation model. The trend in the difference in the dominance of the incubation mechanism is the same as the trend in the difference of saturation temperature conditions. Therefore, this result gives an idea that the boundary of the mechanism for bumpy structures might be predictable by the incubation model.

Chapter 5

Chemical properties by USP laser processing

The aim of this chapter is to investigate the change of CA over time on laser micro-structured surfaces. To discuss the change of CA over time, the existing studies have made simple comparisons of chemical components and CA and have been limited to qualitative discussions. The details of the existing research are shown in section 2.3. Despite various studies, one of the issues in previous studies is that few models in previous studies have considered the effects of multiple chemical components. Therefore, the challenge of this work is, in order to investigate the reason for the change of CA, first, to create a relational equation that directly relates CA to multiple chemical components. In this study, the model that shows the relationships between CA and multiple chemical components was developed and the detail of the model is shown in section 2.4. In this chapter, at first, the model is validated using the surfaces immediately after laser micro-structuring by using several liquids. Then, to understand the reason for the change of CA, then the long-term stability was discussed with this model.

5.1 The chemical effect immediate after laser processing

To validate the model, at first approximate value of square roots of SFE is obtained by conducting experiments for having several data set of different chemical properties surface. In detail, several data set of roughen surface and chemical surface was obtained experimentally. Then multiple regression analysis was conducted. Then, with different liquids which is not used for generating the model, the model was verified.

5.1.1 Experiments

The sample and experimental setup that is used for generating the model is explained in section 3.2. In this study, to consider the topography effect, two different rough structures were created on the surface. The surfaces were structured by the laser using a bidirectional hatching pattern, varying the process parameters as shown in tab. 5.1 to create different roughness values on the surfaces. The sponge-like structures, which have a high roughness, were created. This sponge-like structure is a combination of bumps and holes with typical diameters of the structures of several μm and a depth or height of up to several tenths of μm. The SEM image of this type of structure and its cross-section is shown in tab. 5.1. This kind of structure is known for getting super-hydrophobic for several days after the laser process [56]. As for another structure, small roughness structures were created on stainless steel. This small roughness structure has a few μm periodic shallow structures and nanoparticles, as seen in the SEM image and cross-section image in tab. 5.1. The structure parameters r, f were obtained by the way explained in section 3.4.3. The structure parameters are measured at 3 different positions and have deviations. Since measured CA exceeds $120°$ at only sponge-like structure, Cassie-Baxter state is only realized in sponge-like structures. Therefore structure parameter f was obtained only at sponge-like structure.

Table 5.1: Summary of structure and experimental condition and structure parameter.

	sponge-like structure	small roughness structure	reference
SEM	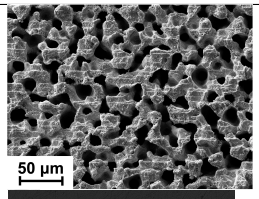	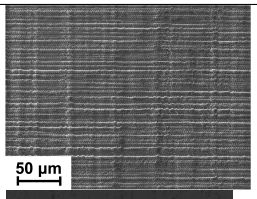	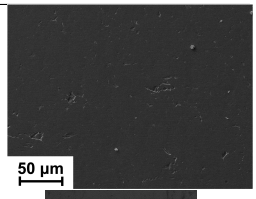
cross-section image	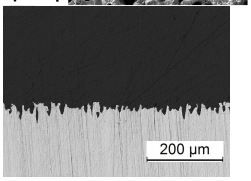	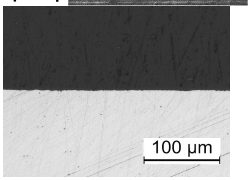	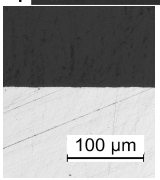
laser power	9.6 W	1.7 W	/
pulse repetition rate	500 kHz	200 kHz	/
burst pulse	1	10	/
pulse overlap	72.5 %	93.1 %	/
hatching distance	5 μm	2.5 μm	/
scan times	16	8	/
r	3.73 ± 0.27	1.12 ± 0.02	1.00 ± 0.00
f	0.23 ± 0.05	/	/

For considering the chemical properties effect, different post-processes and

storage conditions were examined. In this study, 2 different post-processes and 2 different storage conditions for each structure were examined. The post-process condition and storage conditions are explained in subsection 3.3. The summary of different experimental conditions is shown in tab. 3.2. In the end, surfaces with12 different physical and chemical properties were created.

For the chemical properties evaluation, XPS was performed on the laser micro-structured area as well as on the reference surface to measure the concentration of the chemical components, which means examining a_i in eq. (2.30) to eq. (2.32).

For the later multiple regression analysis, only elements relevant at the surface were considered. So metallic bulk materials were neglected for the multiple regression analysis since the metallic bulk is oxidized as soon as metallic bulk is at the air. The image of the surface is shown in fig. 5.1.

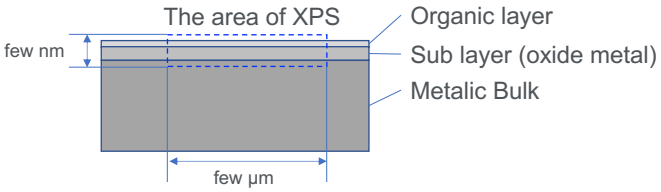

Figure 5.1: cross-section image of surface and area of XPS

After omitting the bulk-specific metal components, to get representative concentrations for the sample surface, the sum of concentrations for all surfaces relevant species was normalized to 100 %. After that, trace elements with very small concentrations were neglected for multiple regression analysis. Moreover, in multiple regression analysis, it is also important to consider the correlation between the explanatory variables. To avoid multicollinearity in the multiple regression analysis, some of the chemical concentrations which are correlated with each other were omitted. In this study, when the correlation coefficient of each chemical is over 0.65, it is assumed as a correlation. For example, when hypothetical chemical 1 and chemical 2 are perfect linearity relations, the eq.(2.31) will be changed as shown in eq.(5.2).

$$\text{when} \quad a_2 = \alpha_2 a_1 + \beta_2 \tag{5.1}$$

$$\begin{aligned} S_p &= a_1\sqrt{\sigma_{S_1}^P} + a_2\sqrt{\sigma_{S_1}^P} + a_3\sqrt{\sigma_{S_3}^P} + \cdots \\ &= a_1(\sqrt{\sigma_{S_1}^P} + \alpha_2\sqrt{\sigma_{S_1}^P}) + a_3\sqrt{\sigma_{S_3}^P} + \cdots + \beta_2\sqrt{\sigma_{S_1}^P} \\ &= a_1\sqrt{\sigma_{S_1}^P}' + a_3\sqrt{\sigma_{S_3}^P} + \cdots + \text{Cost.} \end{aligned} \tag{5.2}$$

This means the most impact variables of the chemical components (e.g. $\sqrt{\sigma_{S_1}^P}'$) is

the sum of the effect from other chemical components which are correlated to each other (e.g. chemical 1 and chemical 2). In the end, chemical components of carbon-(C-C(C-H)), carbon-(polar), oxygen-(metal oxide), oxygen-(layer), chromium oxide-(Cr_2O_3), and iron oxide were used in multiple regression analyses as shown in tab. 5.2. In tab. 5.2, nitrogen, calcium, magnesium, nickel, and silicon are not shown since these elements are either metallic or trace elements.

Table 5.2: Summary of the elements for multiple regression analysis after considering metallic bulk material, trace elements and multicollinearity.

elements	binding states	reason for omitting	indication at this study
carbon	C-C(C-H)	/	carbon-(C-C(C-H))
carbon	COC,O=C-O,O-C-O	/	carbon-(polar)
oxygen	FeO, Fe_2O_3, CrO_3	/	oxygen-(metal oxide)
oxygen	Org. O=C-O, C-O, C-OH, Cr_2O_3	/	oxygen-(layer)
chromium	Cr metal	metallic bulk material	/
chromium	Cr_2O_3	/	chromium oxide-(Cr_2O_3)
chromium	CrO_3	trace elements	/
iron	iron Metal	metallic bulk material	/
iron	iron Oxid	/	Iron oxide

For the surface properties evaluation, the CA for different kinds of liquid were measured. The measurements were taken 3 times in the same area. In this study, water and diiodo-methane were used.
For multiple regression, within the prepared data set, data from small roughness structures and reference surfaces were used for the multiple regression analysis to predict the solid SFE for the polar part and dispersive parts. While conducting multiple regression analysis, the backward elimination method was used to eliminate the effect of randomness. This means starting with all candidate variables and deleting the variable, if any, whose loss gives the most statistically insignificant deterioration of the model fit. In this study, variables whose P-value was larger than 5% were deleted. This process was repeated until no further variables could be deleted without a statistically insignificant loss of fit.

5.1.2 Results and discussion

The measurement results of the CA of each surface are shown in fig. 5.12. According to fig. 5.12, the CAs of laser-processed surfaces were very small as reported in several literatures [3, 69, 37].

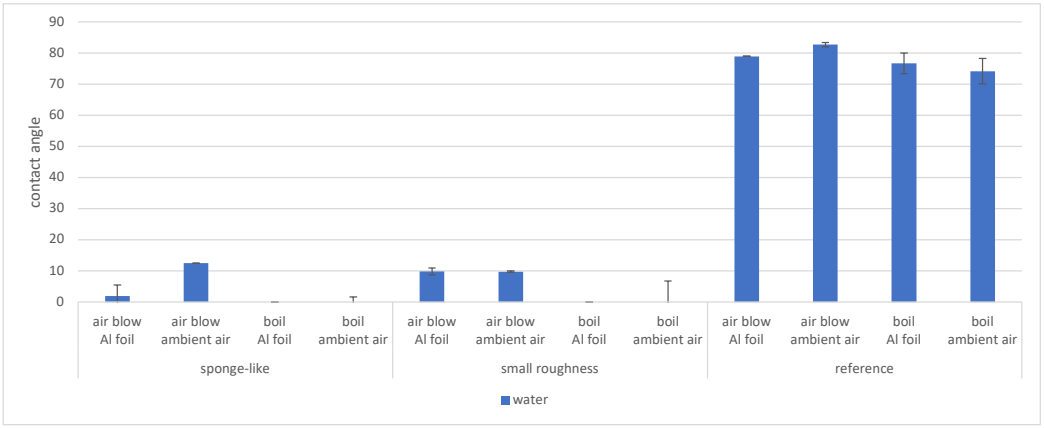

(a) CA of water

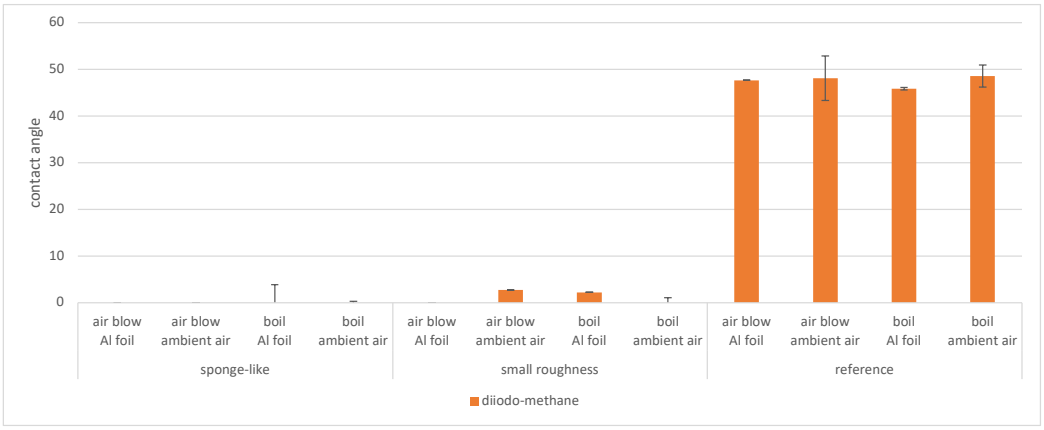

(b) CA of diiodo-methane

Figure 5.2: CA for each post process

By using these results of the CA and eq. (2.14), eq. (2.15), and eq. (2.30), the value of S_p and S_d, were obtained for the different structured surfaces and storage conditions or rather post processes as shown in fig. 5.3. According to fig. 5.3, the results show that S_p and S_d at reference surfaces have low values compared to the processed surfaces. This means that the laser process has changed the surface chemical from the reference surface. According to the C.Y. Cui et al. [70] after laser micro-structured stainless steel surface becomes iron oxide Fe_2O_3 and chromium oxide Cr_2O_3. Therefore, this oxide layer might lead to this surface chemical change.

The concentrations of these components for each condition measured by XPS are summarized in fig. 5.4. According to fig. 5.4, there was a trend that iron oxide at the reference surface was lower than iron oxide at the laser processed surface. Additionally, there was the trend that carbon-(C-C(C-H)) at the laser process surface was lower than that of the reference surface. For the evaluation of the deviation of each chemical concentration, further experiments were conducted. At one of each structured area (sponge-like structure, small roughness structure, reference structure), XPS was conducted in five different positions in the same structured area.

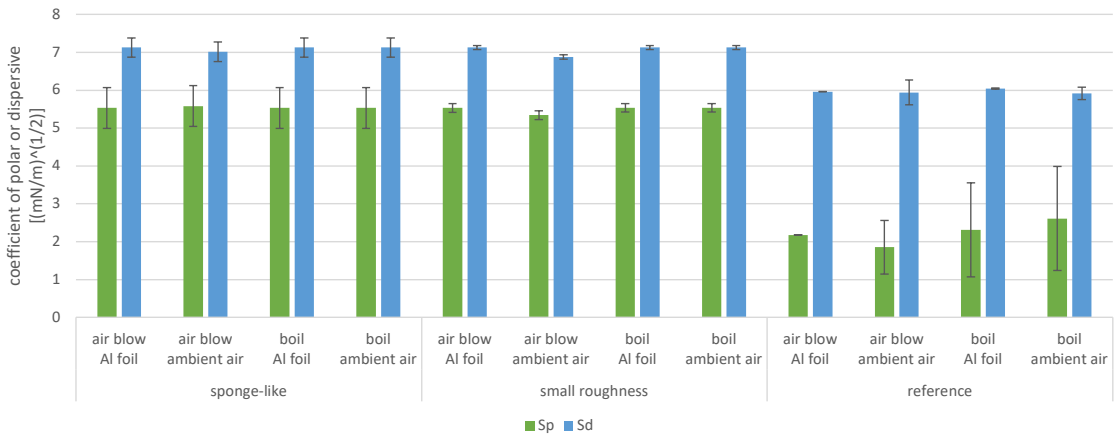

Figure 5.3: Coefficient of polar and dispersive (S_p, S_d) for each surface

The deviation of each chemical concentration was shown in the bar in fig. 5.4. These results showed that the 12 data set, which has different physical and chemical properties, were prepared by changing structure, post-processes, and storage conditions.

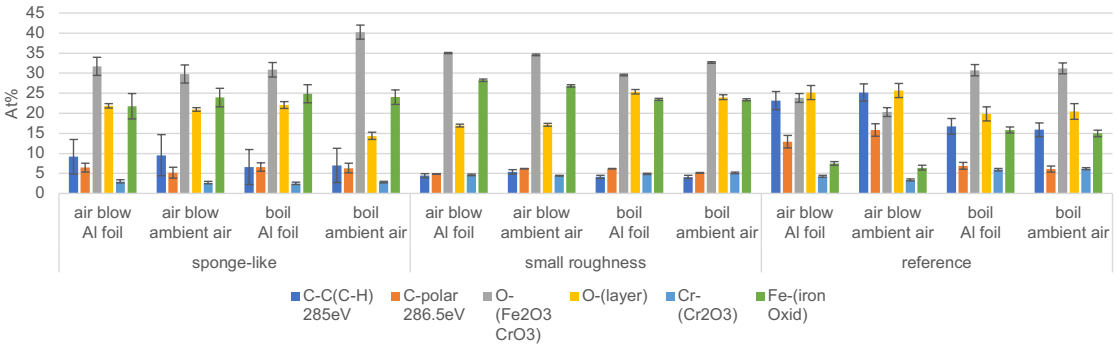

Figure 5.4: Concentration of components used for multiple regression analysis for different experimental conditions.

Since it is difficult to see the reason of the difference of CA by comparing the chemical components' concentration and CA, multiple regression analysis was conducted.

For multiple regression, within the prepared data set, data from small roughness structures and reference surfaces were used for the multiple regression analysis to predict the solid SFE for the polar part and dispersive parts. The results of multiple regression analysis was shown in tab. 5.3.

The chemical components column shows the intercept and kinds of chemical components which remained after multiple regression analysis. The coefficients column shows the intercept value and the coefficient value of each chemical component. The standard error column shows the standard deviation value of each

Table 5.3: SFE of each chemical component

(a) polar part

chemical components	coefficients mN/m	standard error mN/m
Intercept	-6.30	0.31
carbon-(C-C(C-H))	-19.16	2.02

(b) dispersive part

chemical components	coefficients mN/m	standard error mN/m
Intercept	5.34	0.24
iron oxide	6.37	1.15

chemical component in the model. For the coefficient of the polar part (S_p), the adjusted R square was 0.93. The value of R square shows how well the model replicated the results. This model is well described when this value is closer to 1. The carbon-(C-C(C-H)) had a very low P-value (0.008%), which means these chemical correlate well to S_p. From these results, S_p might negatively correlate to dispersive part of carbon-C-C(C-H). For the coefficient value of the dispersive part (S_d), the adjusted R square was 0.81. The iron oxide had a very low P-value (0.1%), which means these chemicals correlate well to S_d. From these results, S_d might correlate to dispersive chemical binding states such as the dispersive part of iron oxide. This result fits the other literature [56] that shows CA is related to carbon and oxide. Other chemical components did not appear in this multiple regression analysis results. It might be because the effect of other chemical components was small compared to shown chemical components or because the effect of chemicals was random, or the data set was not so enough to predict the effect of the other parameter for this time.

To verify this model, the CA of water and diiodo-methane for all structures, including sponge-like structures, were calculated from the concentrations of chemical components by using this model. These calculated CA were compared to the measured CA of water or diiodo-methane. The results are shown in fig. 5.5 fig. 5.6. Standard deviation on the vertical axis was calculated from the standard deviation from the coefficient value, structure parameter (r, f), and local distribution of chemical concentration (a_i). The standard deviation on the horizontal axis comes from the deviation of the CA measurement. From these results, calculated CAs were well-predicted of measured CA.

In addition, to verify this model for another liquid that is not used for the prediction of the polar part and dispersive part of SFE for solid, the CA of ethylene-glycol (the dispersive and polar part of ethylene-glycol are 26.4 mN/m, and 21.3 mN/m [66]) were calculated from the same model and compared it with the measured CA of ethylene-glycol. CA of ethylene-glycol was also measured by a drop shape ana-

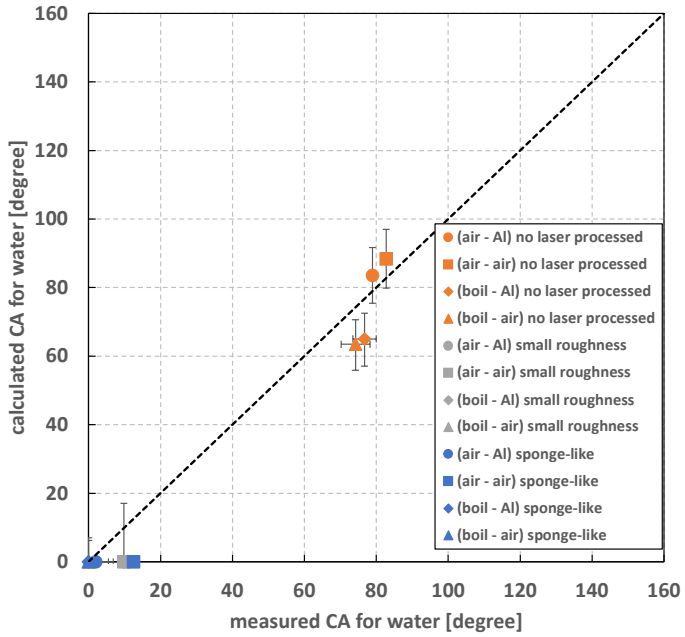

Figure 5.5: Comparison of measured CA and calculated CA for water. The color difference shows the type of structures. (light blue, gray, and orange symbols represent sponge-like, small roughness, and reference structure, respectively.) The shape difference shows the type of post-process and storage conditions. (circle (○), square (□), diamond (◇), triangle △), represent No.1, No.2, No.3, and No.4 of experimental conditions in tab. 3.2)

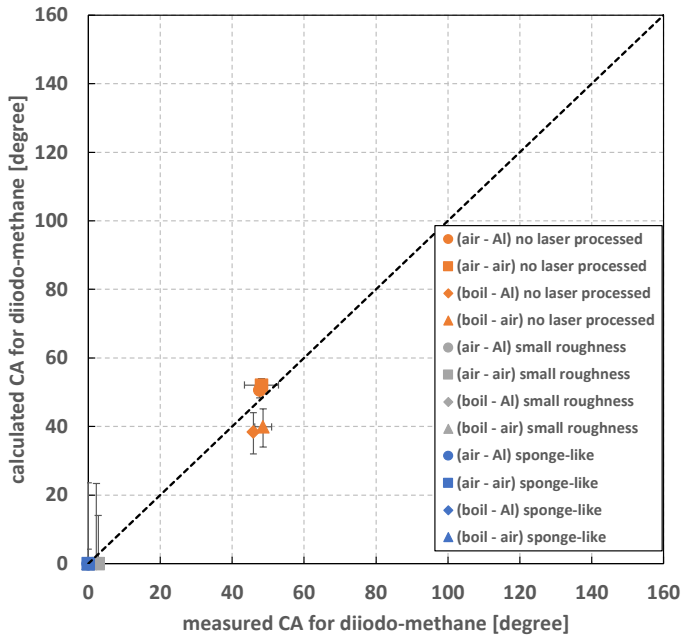

Figure 5.6: Comparison of measured CA and calculated CA for diiodo-methane. The color difference shows the type of structures. (light blue, gray, and orange symbols represent sponge-like, small roughness, and reference structure, respectively.) The shape difference shows the type of post-process and storage conditions. (circle (○), square (□), diamond (◇), triangle △), represent No.1, No.2, No.3, and No.4 of experimental conditions in tab. 3.2)

lyzer device (DSA30, Krüss GmbH) with the liquid of droplet of 4 μ l. The results are shown in fig. 5.7 fig. 5.8 and showed a nice correlation between measured CA and calculated CA for all surfaces. (the deviation of the difference between measured CA and calculated CA is $7.2°$) From these experiments, the model developed in this study was verified with various liquids.

Comparison with the different model

To compare the results of our model and becker's model described in eq. 2.21, $\cos\theta_0$ was converted to the CA on each surface (sponge-like structure, small roughness structure, reference). The results are shown in fig. 5.9, fig. 5.10, and fig. 5.11. The deviations of the difference between measured CA and calculated CA for the results from Becker's model were $5.6°$, $9.7°$, and $8.3°$ for water, diiodo-methane, and ethylene-glycol, respectively.

And the deviations for the results from the presented model here were $5.1°$, $3.1°$, and $7.2°$ for water, diiodo-methane, and ethylene-glycol, respectively. The presented model here showed a nice correlation between measured CA and calculated CA than Becker's model. On other points, the result from Becker et al. showed that CA for water was a relatively nice correlation between measured CA and calculated CA, but CA for diiodo-methane and ethylene-glycol was not a good correlation. On the other hand, the presented model had a nice correlation for all of the tested liquids. The proposed model shows more detailed chemical components' effect not only on total SFE of solid but also on the polar and dispersive part of SFE for solid, separately. Therefore, this model has the potential to provide insight for understanding chemical components' effect on any kind of laser micro-structured material. The change of CA on laser micro-structured over time is explained in next section.

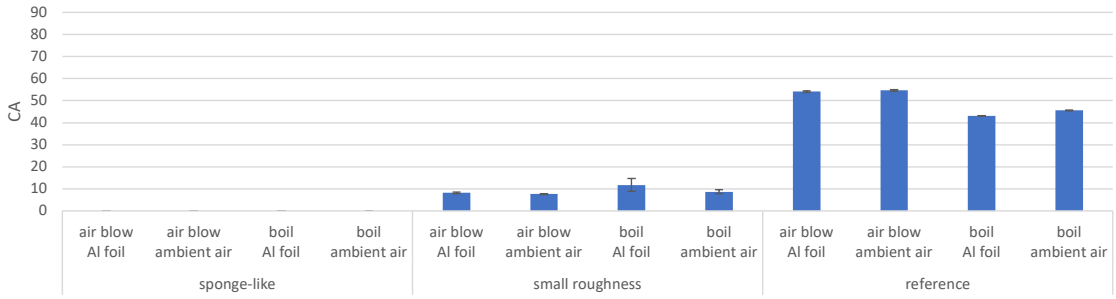

Figure 5.7: CA for ethylene-glycol

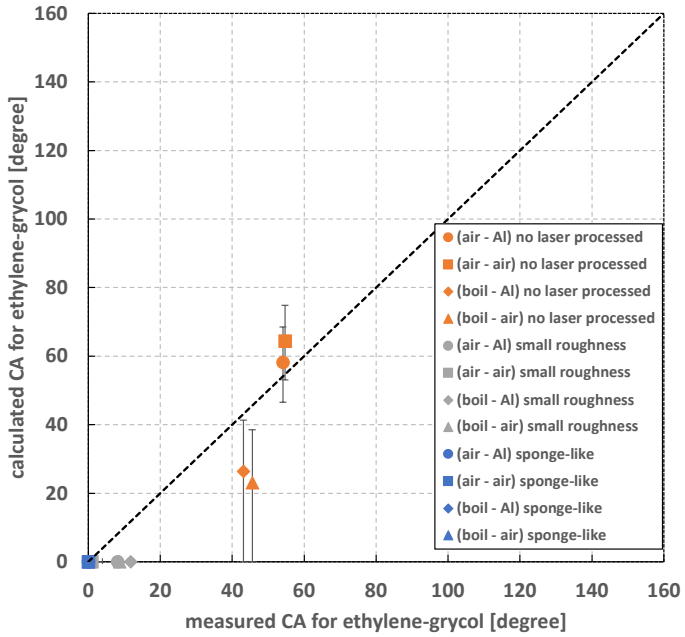

Figure 5.8: Comparison of measured CA and calculated CA for ethylene-glycol. The color difference shows the type of structures. (light blue, gray, and orange symbols represent sponge-like, small roughness, and reference structure, respectively.) The shape difference shows the type of post-process and storage conditions. (circle (○), square (□), diamond (◇), triangle △), represent No.1, No.2, No.3, and No.4 of experimental conditions in tab. 3.2)

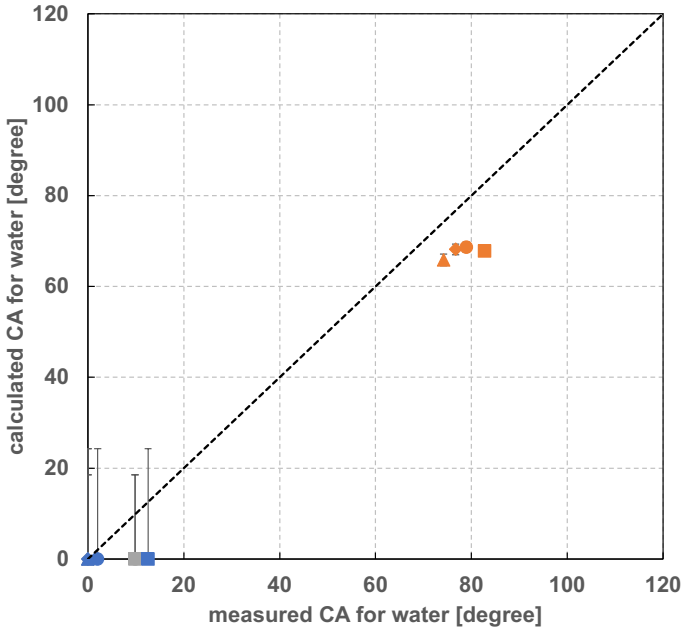

Figure 5.9: Comparison of measured CA and calculated CA from Becker's model for water. The color difference shows the type of structures. (light blue, gray, and orange symbols represent sponge-like, small roughness, and reference structure, respectively.) The shape difference shows the type of post-process and storage conditions. (circle (○), square (□), diamond (◇), triangle (△), represent No.1, No.2, No.3, and No.4 of experimental conditions in tab. 3.2)

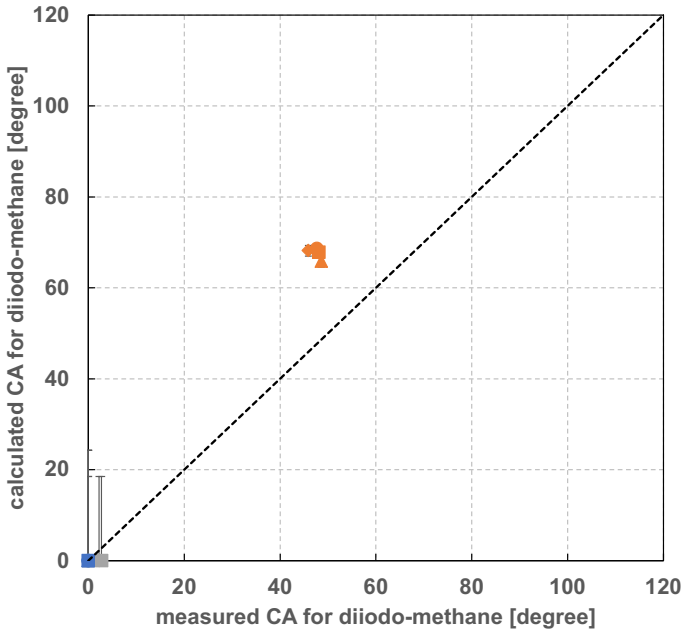

Figure 5.10: Comparison of measured CA and calculated CA from Becker's model for diiodo-methane. The color difference shows the type of structures. (light blue, gray, and orange symbols represent sponge-like, small roughness, and reference structure, respectively.) The shape difference shows the type of post-process and storage conditions. (circle (○), square (□), diamond (◇), triangle (△), represent No.1, No.2, No.3, and No.4 of experimental conditions in tab. 3.2)

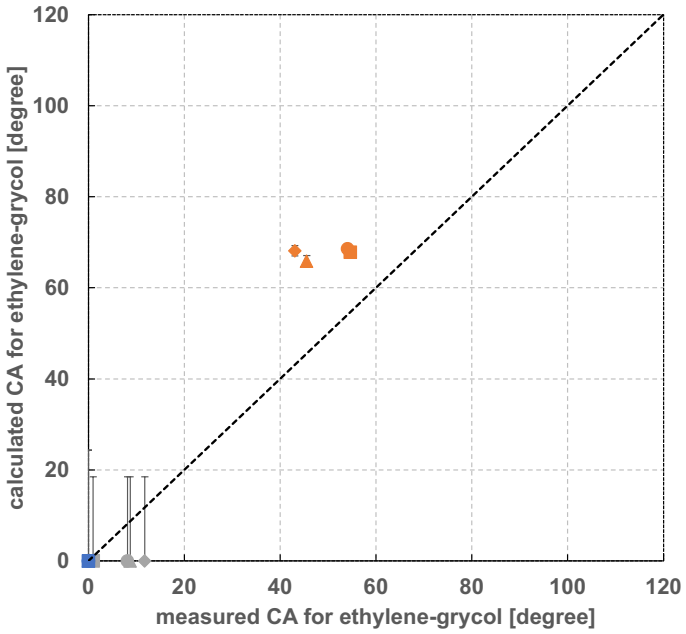

Figure 5.11: Comparison of measured CA and calculated CA from Becker's model for ethylene-glycol. The color difference shows the type of structures. (light blue, gray, and orange symbols represent sponge-like, small roughness, and reference structure, respectively.) The shape difference shows the type of post-process and storage conditions. (circle (○), square (□), diamond (◇), triangle (△), represent No.1, No.2, No.3, and No.4 of experimental conditions in tab. 3.2)

5.2 The chemical effect for long term

In this section, in order to know the reason for changing CA over time, the effect of each chemical component on the effective CA for a flat but chemically heterogeneous surface θ_{0c} was discussed.

5.2.1 Experiment

Material and laser micro-structuring

The kinds of samples used in this long term experiment is shown in previous section.

Characterization for long term

To investigate the change of CA over time, 2 sets of 12 different surfaces were created. All these samples were stored in each condition for over 80 days. For each set of different surfaces, CA was measured at 40 days and 80 days after the laser process. To characterize the chemical composition of the surface and its adsorbate, XPS was performed on the laser micro-structured area and the reference surface to measure the concentration of the chemical components, which means examining a_i. Each set of the different surfaces was measured by XPS at 40 and 80 days after laser structuring. Therefore, one set of 12 samples was measured at 40 days, and another set of 12 samples was measured at 80 days.

To get S_p, S_d, in eq. 2.31, eq. 2.32, the CAs for different kinds of liquid were measured after XPS by a drop shape analyzer device (DSA30, Krüss GmbH) with the liquid droplet of 4 μl. In this study, water and diiodo-methane were used. The measurements were taken 3 times in the same area.

5.2.2 Results and discussion

To have a relationship of CA and chemical components, it is need to perform multiple regression analysis and obtain the influential variables of the chemical components ($\sqrt{\sigma_{Si}^P}$, $\sqrt{\sigma_{Si}^D}$) in the statistical model (eq. (2.30)). In this section, followings results are shown.

- The data of CA of water and diiodo-methane.
- From these CA data, as a characterize the wettability properties, the coefficients of the polar and dispersive part of SFE (S_p, S_d).
- The chemical components of the surface measured by XPS.

- The influential variables of the chemical components ($\sqrt{\sigma_{Si}^{P}}$, $\sqrt{\sigma_{Si}^{D}}$) determined by performing multiple regression analysis.
- After determining the variables, the influences of chemical components on the change of CA over were examined by calculating D in the eq. (2.42).

Contact angle

At first, in order to see the change of the surface properties over time, the results of CA of water and diiodo-methane are shown in fig. 5.12 The upper side of fig. 5.12 shows the change of the CA of water over time, and the lower side of fig. 5.12 shows the change of the CA of diiodo-methane over time.

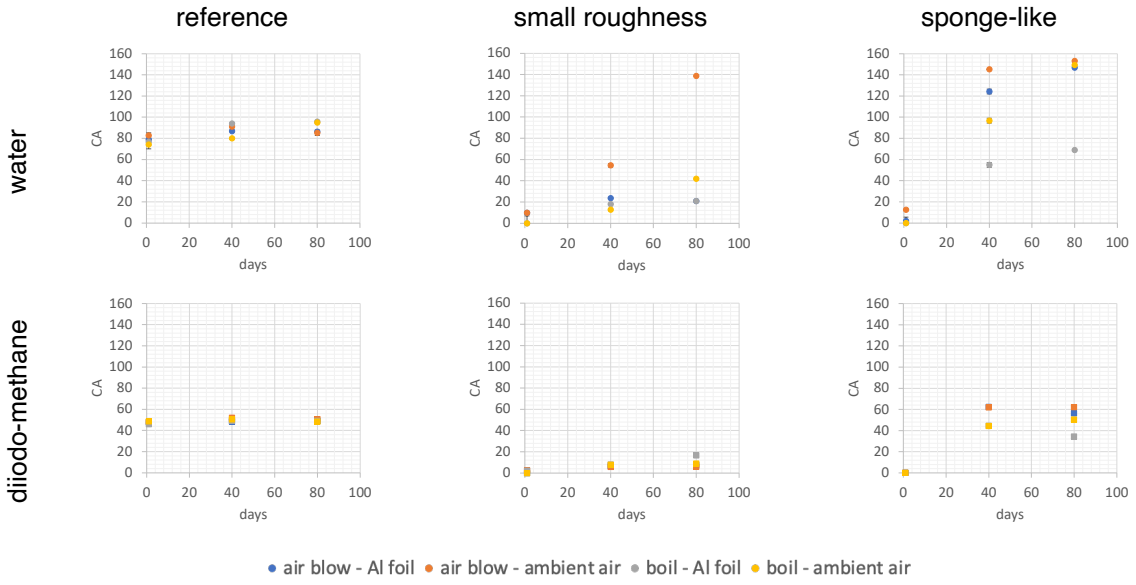

Figure 5.12: CA change over time

First of all, it can be seen that the CA of water on the laser-microstructured surface tends to decrease immediately after processing and increases over time. In contrast, it can be seen that there is little change with respect to time on the reference surface.

Second, diiodo-methane tends to have a lower CA, overall, compared to water. As same as water, there is little change with time on the reference surface. The small roughness surface also shows less variation with time than the reference. On the other hand, sponge-like, as same as water, tends to decrease immediately after processing and increase with time. This is probably because the effect of the change in chemical components is more enhanced by the topography in the sponge-like structure.

The color of each point in fig. 5.12 indicates differences in post-processing

and storage conditions. Regarding reference surface, there is little difference between each post-processing and storage condition. On the other hand, regarding laser micro-structured surfaces, the tendency of CA is different from each post-processing and storage condition. In particular, the structure of sponge-like, which is sensitive to chemical components, shows that the gray-colored condition (boil - Al foil) has a smaller CA for long term. Therefore, in the following discussion, the difference between the blue-colored condition (air blow - Al foil) and the gray-colored condition (boil - Al foil) is focused on in order to consider the temporal effects of the chemical components. Other data are shown in the appendix chapter 8.

Wettability properties: Coefficient of polar and dispersive

To evaluate the wettability properties, the coefficient of polar and dispersive part in eq. (2.30) (S_p,S_d) is calculated. Fig. 5.13 shows the calculated results of the coefficient of polar S_p and dispersive S_d. The green bar shows the polar part, and the blue bar shows the dispersive part.

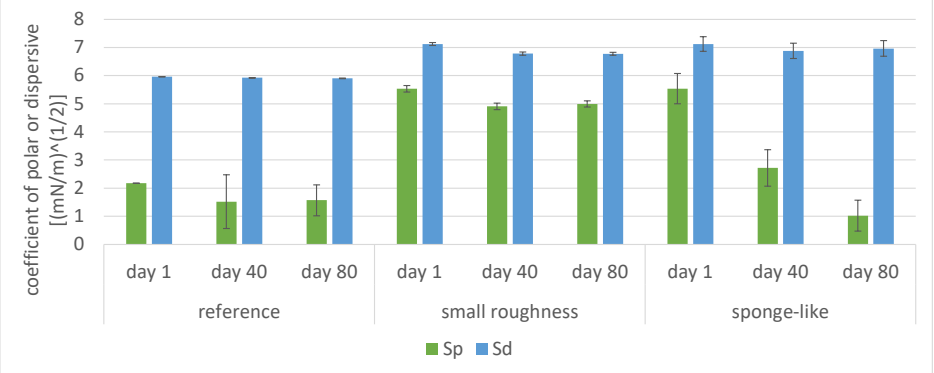

(a) air blow - Al foil

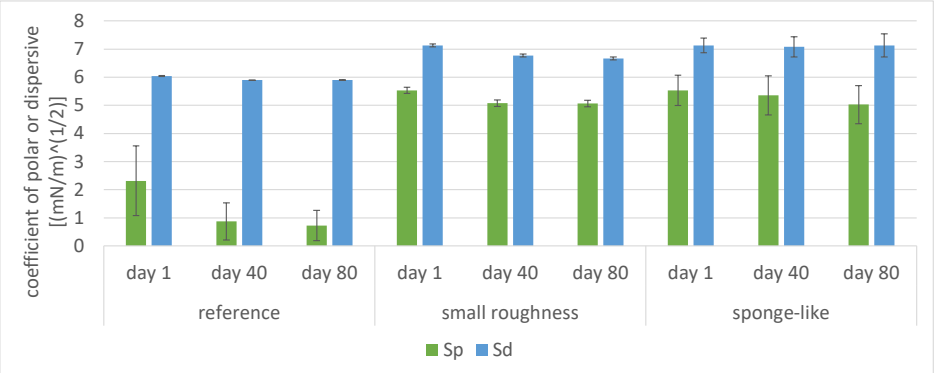

(b) boil - Al foil

Figure 5.13: S_p and S_d change over time

According to fig. 5.13, as a general trend, the dispersive part does not change significantly over time. In addition, the dispersive part of the laser micro-structured surface is higher than that of the reference surface. On the other hand, the polar

part of laser micro-structured surface is initially high but generally decreases over time.

As mentioned in the previous subsection, the sponge-like structure's condition (air blow - Al foil) and the conditions (boil - Al foil) are focused on for discussion. As for the dispersive part, no significant difference can be observed between the condition (air blow - Al foil) and the condition (boil - Al foil). On the other hand, with respect to the polar part, the coefficient of polar part decreases with time in the condition (air blow - Al foil), while it remains large in the condition (boil - Al foil). The difference is shown in the CA of water in fig. 5.12, where the CA is large under the condition (air blow - Al foil) and remains small under the condition (boil - Al foil). From this, it can be inferred that the polar part is a factor that significantly changes the CA.

Chemical ratio

In order to understand the reason of the change of polar part and dispersive part of SFE, the ratios of surface chemical components were examined at each time point. Fig.5.14 shows the results of the concentration of each chemical component measured by XPS. After measuring the chemical components, for the multiple regression analysis, only elements relevant at the surface, which were shown in tab. 5.2, were considered. In fig. 5.14, each item of the radar chart shows the concentration of each chemical component measured by XPS and each color shows that time of measurements. The indicators on the axes show the ratio of each chemical species as a percentage.

According to fig. 5.14, as a general trend, carbon-(C-C(C-H)) increases over time. In addition, laser-micro-structured surface contains more oxygen-(metal oxide) and iron oxide than that of the reference surface. As a general trend, the chemical components for small roughness structures are similar to that of sponge-like structures. Since it is difficult to mention the relationship between CA (or wettability properties) and chemical components from only a comparison between CA and XPS data, in order to obtain the influential variables of the chemical components ($\sqrt{\sigma_{Si}^{P}}$, $\sqrt{\sigma_{Si}^{D}}$), multiple regression analysis is conducted in the next subsection.

Multiple regression analysis

In order to obtain direct relationship between CA and chemical components, and to obtain the influential variables of the chemical components ($\sqrt{\sigma_{Si}^{P}}$, $\sqrt{\sigma_{Si}^{D}}$), multiple regression analysis was conducted. The trends of CA over time of the reference surface were different from the laser-micro-structured surface (small-roughness and

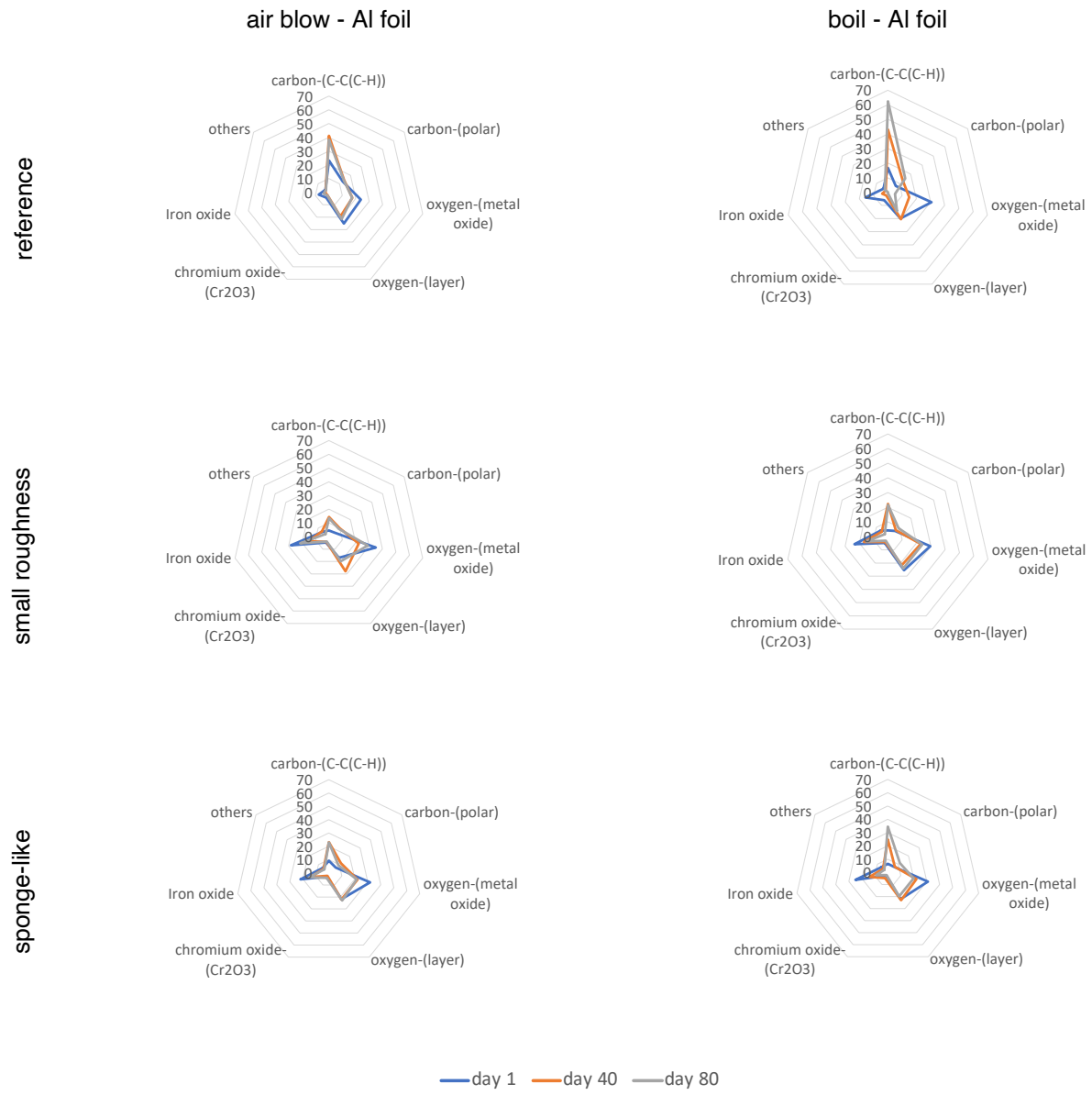

Figure 5.14: Chemical components ratio change over time: The indicators on the axes show the ratio of each chemical species as a percentage.

sponge-like structure), multiple regression analyses for the reference surface and laser-micro-structured surface (small-roughness and sponge-like structure) were done separately. In addition, since the trend of increase of CA is different from each post process and storage condition as shown in fig. 5.12, multiple regression analysis is done at each post process and storage condition. The results are summarized in tab. 5.4. The row of the table shows the coefficient of polar and dispersive for each chemical component. The intercept row shows the effect of the omitted chemicals.

According to tab. 5.4, for polar parts of laser micro-structured surface are negatively correlated to the carbon-(C-C(C-H)). This is reasonable since it is said that

Table 5.4: Multiple regression analysis for each condition

(a) polar

chemical components	laser processed surface air blow - Al foil coefficients $(mN/m)^{1/2}$	laser processed surface boil - Al foil coefficients $(mN/m)^{1/2}$	reference coefficients $(mN/m)^{1/2}$
Intercept	7.42	5.60	0.68
carbon-(C-C(C-H))	-22.2	-1.71	-
carbon-(polar)	-	-	-
oxygen-(metal oxide)	-	-	-
oxygen-(layer)	-	-	-
chromium oxide-(Cr_2O_3)	-	-	27.7

(b) dispersive

chemical components	laser processed surface air blow - Al foil coefficients $(mN/m)^{1/2}$	laser processed surface boil - Al foil coefficients $(mN/m)^{1/2}$	reference coefficients $(mN/m)^{1/2}$
Intercept	7.42	6.67	6.05
carbon-(C-C(C-H))	-	-	-
carbon-(polar)	-5.41	-	-1.22
oxygen-(metal oxide)	-	1.23	-
oxygen-(layer)	-	-	-
chromium oxide-(Cr_2O_3)	-	-	-

carbon-(C-C(C-H)) is assumed a non-polor chemical component. Therefore, when carbon-(C-C(C-H)) increase, polar coefficient S_p decrease. Note that the effect of carbon-(C-C(C-H)) is different from each post-process and storage condition. The polar coefficient of condition (bold - Al foil) is lower than that of conditions (air blow - Al foil). Regarding the dispersive part, for conditions (air-blow-Al foil), dispersive parts are negatively correlated to the carbon-(polar). On the other hand, for condition (boil - Al foil), dispersive parts are not correlated to carbon-(polar).

For reference surface, the polar coefficient correlated to chromium oxide-(Cr_2O_3), and the dispersive coefficient negatively correlated to carbon-(polar). Stainless steel that has not been laser micro-structured (reference surface) has a passive film, consisting of chromium oxide. If that passive film is present, the polar part is expected to be affected by the ratio of the passive film, or at least the effect of carbon-(C-C(C-H)) is not strong.

To discuss why the value of carbon-(C-C(C-H)) of condition (boil - Al foil) is lower than that of the condition (air blow - Al foil), the correlation of each chemical component was considered, since the correlation of each chemical components changes

the results of multiple regression analysis as it described in eq. (5.2).

Table 5.5: Correlation coefficient for carbon-(C-C(C-H))

	laser processed surface	
	air blow - Al foil	boil - Al foil
	carbon-(C-C(C-H))	carbon-(C-C(C-H))
carbon-(polar)	0.86	0.76
oxygen-(metal oxide)	-0.92	-0.99
oxygen-(layer)	0.41	0.67
chromium oxide-(Cr_2O_3)	-0.54	-0.38

The correlation coefficient for carbon-(C-C(C-H)) is also shown in tab. 5.5. The value in the cell shows the correlation coefficient of carbon-(C-C(C-H)) and each chemical component. According to tab. 5.5, for condition (air blow - Al foil), carbon-(C-C(C-H)) correlates with carbon-(polar) and oxygen-(metal oxide). On the contrary, for condition (boil - Al foil), carbon-(C-C(C-H)) correlates with carbon-(polar) and oxygen-(metal oxide) and oxygen-(layer). Therefore, the reason for the low value for condition (boil - Al foil) might be the effect of oxygen-(layer), which includes Organic O=C-O, C-O, C-OH, and Cr_2O_3, is increased by boiling and remained for long term because of the Al foil covering.

Change of chemical components over time

For analyzing the effect of chemical components on CA over time, the model described in subsection 2.4.2 was used. By using the quantitative value of the contribution of each chemical species in CA ($D_{m(\alpha-\beta)(i)}$ in eq. (2.42)), the effect of each chemical component in the changes between day 40 and day 1, day 80 and day 1 were calculated. The results are shown in fig. 5.15. The green bar shows the difference of measured CA at a flat surface on each days. The right side of the green bar is the stacked bar of each chemical component which is calculated CA at a flat surface.

According to fig. 5.15 the effects of each chemical component were shown in the unit of angle degree. At first, most of the calculated differences of CA correspond to the measured difference of CA. The standard deviation of the difference between the measured difference of CA and the calculated difference of CA is 20.1 degree. The large difference between the measured and calculated one is seen on the sponge-like structure. This is might because since the sponge-like structure has deep holes and very rough surface, the contamination from air reach to each surface differently. This leads to the chemical composition might different from the

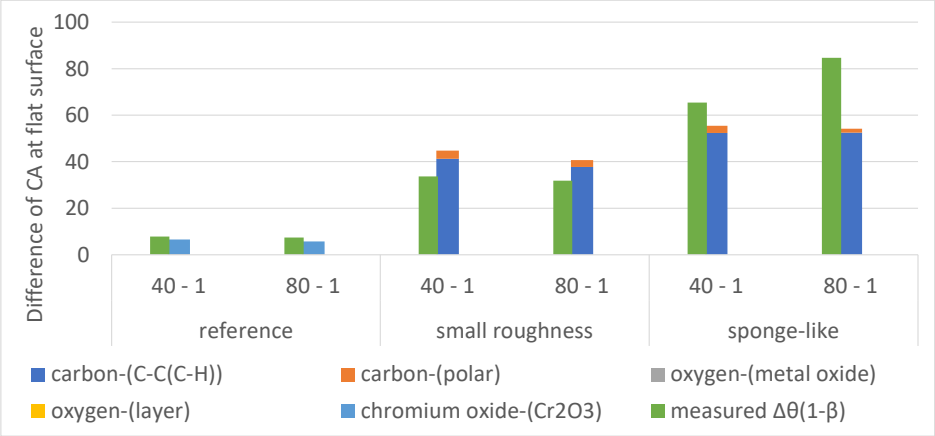

(a) air blow - Al foil

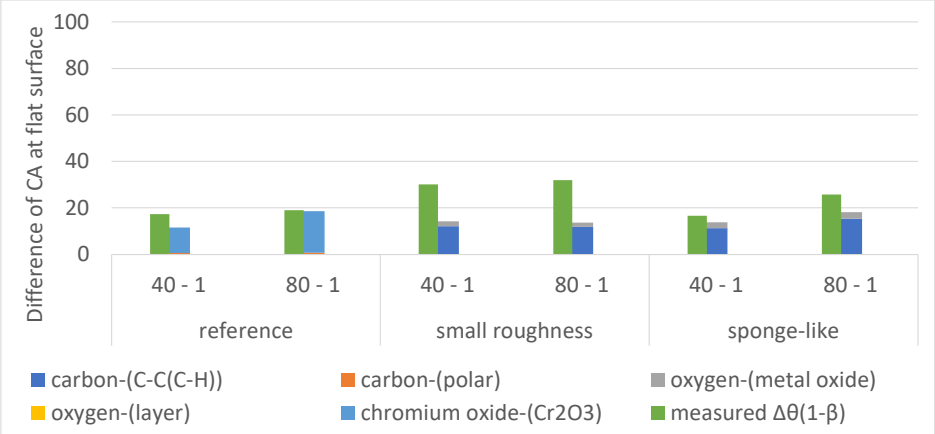

(b) boil - Al foil

Figure 5.15: CA difference at flat surface over time

top of the structure and the bottom of the holes. In the future, more investigation is needed for more detailed explanations. From this calculation, most of the reason of the increase of CA over time can be described by the chemical concentration of carbon-(C-C(C-H)) for the laser-micro-structured surface (small roughness and sponge-like structure). Note, as it is discussed in the previous subsection, within this effect of carbon-(C-C(C-H)) including the effect from other correlated chemicals.

In the end, from the multiple regression analysis (tab. 5.4), the correlation coefficient of each chemical component (tab. 5.5) and CA difference analysis (fig. 5.15), at first, the reason for the change of CA for laser micro-structured surface (small roughness and sponge-like) from the CA of reference surface is that the effect of chromium oxide-(Cr_2O_3) becomes less but the effects of carbon-(C-C(C-H)) (which include the effect of carbon-(polar) and oxygen-(metal oxide)) becomes much. In addition, the reason for the CA becomes high for condition (air blow - Al foil) comes from carbon-C-C(C-H), and carbon-(polar) and oxygen-(metal oxide). Moreover, the reason for the CA remains low for condition (boil - Al foil) comes from the ef-

fect of oxygen-(layer), which includes Organic O=C-O, C- O, C-OH, and Cr_2O_3, is increased by boiling and remain for the long term by storing in Al foil.

5.3 Conclusion

In order to investigate the reason for the change of CA, the challenge of this work is to create a relational equation that directly relates CA (or surface free energy) to multiple chemical components. Therefore, at first, a model that can treat multiple chemical compositions was developed in chapter 2. The approach was done by extending Dupre's model and Owen's model to the chemically heterogeneous model and evaluating the value by multiple regression analysis. This model is validated for several structures such as sponge-like structures and small roughness structures and reference structures, and also different liquids. From the results, calculated CAs were well-predicted of measured CA. Therefore, these results show that the proposed model can be used for prediction of CA.

The other challenge of this work is,to understand the reason for the change of CA, the long-term stability was discussed with the developed model. To investigate the long-term effect of the model for the long term was also developed in chapter 2. From this calculation, the reason for the change of CA for laser micro-structured surface (small roughness and sponge-like) from the CA of reference surface is that the effect of chromium oxide-(Cr_2O_3) becomes less but the effects of carbon-(C – C(C – H)) (which include the effect of carbon-(polar) and oxygen-(metal oxide)) becomes much. In addition, the reason for the CA becomes high for condition (air blow - Al foil) is carbon-C – C(C – H), and carbon-(polar) and oxygen-(metal oxide). Moreover, the reason for the CA remains low for condition (boil - Al foil) is the effect of oxygen-(layer), which includes Organic O = C – O, C – O, C – OH, and Cr_2O_3, is increased by boiling and remain for the long term by storing in Al foil.

In addition, the benefits of the model developed by this study include the following. It was shown that more detailed causes of time variation can be determined.Thus, the cause of time variation can be considered from the effects of multiple chemical components. It was shown that the model can be applied to ethylene glycol other than water and diiodomethane. It was shown to be applicable to other liquid and adhesive substances. Since the model deals with polar and non-polar nature of SFE, it may be useful for different metals as well.

Chapter 6

Application example

In this chapter, by using what I have learned in the process of conducting this research, examples of surface functionalization of real-world applications is described. The first is a study on reducing the resistance of devices (thin metal wires) in medical devices. The second is a study on increasing the bonding strength between composite materials and metals.

6.1 The effect of wettability on controlling friction

In the previous section 5, the effect of chemical properties was discussed. In this section, the effect of wettability on the friction reduction is discussed.

As an application, the medical guide wires in surgeons are focused. The image of medical guide wires which are used by surgeons is shown in fig. 6.1. This wire is for example used in blood vessels. Therefore one of the demands of medical wires is reducing the friction between guide wires and the inner wall of the vascular system so that preventing injuries.

Figure 6.1: The image of guide wire: the image was taken from the webpage of Epflex [71]

It is known that friction force reduction is an interaction between surface chemistry and realized micro/nanostructures on the surface by laser texturing [37]. Regarding to micro/nano-structures, one of the candidate structures to reduce friction is the dimple structure [72]. Etsion et al. reported that textured surfaces covered with micro dimples were suitable for reducing friction in hard materials around the year 2000 [73, 74, 75].

However, in contrast to most other papers, in this application, one of the two surfaces is very easily and reversibly deformable. In addition, only one of the two surfaces, the metal wire, is available for functionalization. Due to these limitations, the results of other investigations could not be applied on a one-to-one basis.

Therefore, the effect of the dimple structure of the medical guide wire on friction reduction was investigated. Due to that this friction reduction in dimple structured surface is related to hydrodynamics, it is known that the friction reduction depends on chemistry properties and structure dimensions of dimple such as the size of the dimple and depth of the hole and area coverage ratio [76, 77]. Regarding the effect of the size of the dimple, the aspect ratio of the dimple, and the area coverage ratio are also investigated by us [78]. Regarding the effect of the chemical properties, the wettability of the surface is expected to have a large impact on its effects. For example, if an extremely hydrophobic state is reached within the dimple, it can be assumed that no more water will be found in these areas. Underwater, small air cushions form inside the dimple, and their positive effect on friction is eliminated. If, on the other hand, the surface is hydrophilic, the air is displaced from the dimples when they are immersed in the water, and the dimple is filled with liquid. In this state, the dimples can fully develop their effect, and the frictional forces can be significantly reduced.

Thus, in this study, the effect of wettability properties on the friction of the dimple-structured medical guide wire in the aqueous environment was investigated. For these investigations, the tissue of the vascular system was represented by silicone pads. The aqueous environment present during surgery was represented by water for the tests.

6.1.1 Experiments

Materials and preparation

To investigate the technical feasibility of friction reduction, flat stainless steel 304 wires were used. The width of the wires was 800 μm, and their thickness was 200 μm. Before and after micro-structuring, the wires were cleaned by wiping

them five times with cleanroom wipes soaked in isopropanol. Before surface micro-structuring, this cleaning was necessary to prevent interference of contaminants to the laser process. After surface micro-structuring, this was needed to clean debris to partially cover the surface close to the individual dimples.

Laser process

These dimples were structured on both sides of the wires by using a five-axis laser material processing system as shown in chapter 3. To create a dimple, the laser spot was positioned at the desired location on the sample material using the axes and the scanner. This position is then irradiated with several laser pulses until the desired depth is reached. The dimple structure made by laser is shown in fig. 6.2.

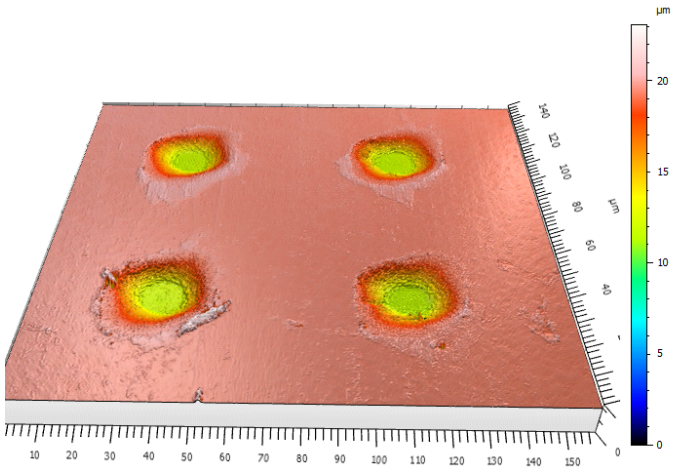

Figure 6.2: Confocal image of dimple textured surface

After optimizing the size of the dimple from our previous study [78], the aspect ratio of the dimple, and the area coverage ratio, the dimples with a diameter of 17 μ m and a depth of 10 μ m were introduced into the surface in a square arrangement and at a dimple spacing of 75 μ m. This results in an area coverage of the dimples of 4 %. A summary of the dimple structures with the process parameters used to create them can be found in tab. 6.1.

post-process

For chemical properties, since the friction reduction is based on hydrodynamic flows within the dimples, the wettability of the surface was expected to have a great influence on the frictional forces. To establish a hydrophilic state the samples were put into boiling water after the structuring and cleaning process. To establish a hydrophobic state the samples were put into a vacuum chamber.

Table 6.1: The process parameters used for dimples.

dimple diameter	17 um
dimple depth	10 um
wavelength	532 nm
focus length	100 mm
spot diameter	10 um
pulse repetition	20 kHz
power of laser	0.24 W
pulse numbers	400
dimple spacing	75 um

Characterization of surface morphology and topography

The morphology and topography of the textured surfaces were studied by using optical microscopy (Axio Imager, Carl Zeiss AG) and confocal microscopy (Zeiss smart proof 5, Carl Zeiss AG). Fig. 6.2 shows a confocal image as an example with a dimple textured surface.

Characterization of wettability

For the characterization of the wettability of selected textured samples, a drop shape analyzer system (DSA30, Krüss GmbH) was used.

Characterization of friction

For the friction measurement, the stainless steel samples were pulled through two silicone pads that were pressed together with a force of 3 N by a 3-D printed clamp as shown in fig. 6.3.

The contact area between a silicone pad and the stainless steel was 16 mm^2 (width of the silicone = 20 mm times the width of the stainless steel flat wires = 800 μ m), resulting in an average pressure between the silicone pads and the stainless steel wire of approx. 1,9 bar. To determine the maximum occurring frictional forces, the following measuring procedure was used. One end of the stainless steel samples was fixed to the digital force gauge (Digital Force Gauge Series 3, Mark-10). From there the wire hung downwards between the silicone pads. For simulating the aqueous environment in the application, the silicone pads were submerged under water. By moving the digital force gauge with the motorized linear stage, the stainless steel sample was pulled with a speed of 2 mm/s through the silicone pads.

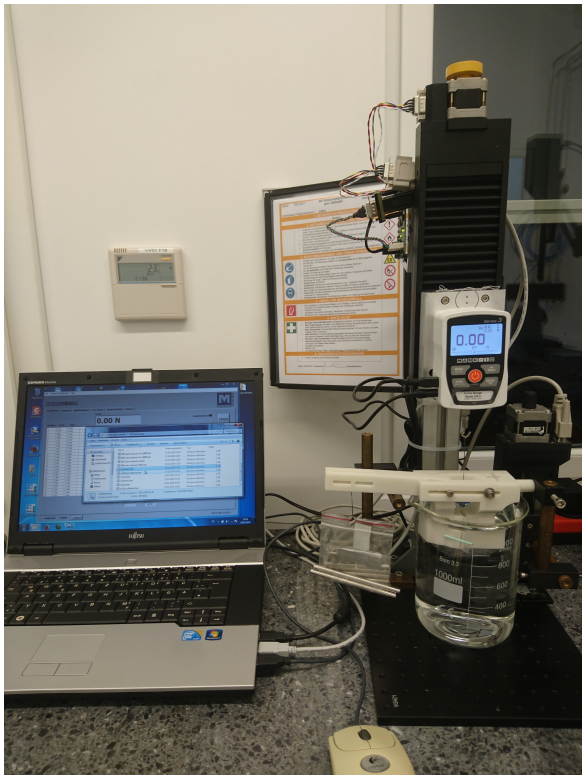

Figure 6.3: Experimental setup for tribological characterization

While this was happening, the digital force gauge measured the force that was necessary to overcome the friction between the steel sample and the silicone. This process was repeated 25 times per sample. Afterward, the maximum force for each round was measured, and an average value for F_{max} for the sample was calculated. A reference value was determined by applying this procedure to various unstructured samples.

The mean value for F_{max} for these samples was at 2.5 N with a standard deviation of 0.25 N. This gives a reference range from 2.25 N to 2.75 N which will be marked green in the following diagrams when presenting the experimental results in section 6.1.2.

6.1.2 Results and discussion

To demonstrate the wettability effect experimentally, wires with two different wettability properties were examined. The results of the friction measurements are shown in fig. 6.4. The values of the hydrophobically conditioned wires are all within the green reference range and can thus hardly be distinguished from unstructured wires on the basis of friction. The hydrophilically conditioned wires show significantly reduced friction measurement values. Compared with the average reference value of 2.5 N, the hydrophilic wires achieve an average friction reduction of slightly more

than 30%. As it can be seen that the friction reduction effect of the dimples only took place for the hydrophilic surfaces when the dimples were filled with lubricant. According to the considerations and measured values described here, the wettability of the surface has a significant effect on the friction reduction by the dimples. In this context, conditioning the surface to a hydrophilic state can permanently preserve the positive effects of the dimple structure. In contrast, hydrophobic conditioning of the surface state can completely prevent the friction-reducing effect of the dimple. Accordingly, a targeted adjustment of the surface wettability is urgently required to obtain a permanent and reproducible friction reduction on the guide wires.

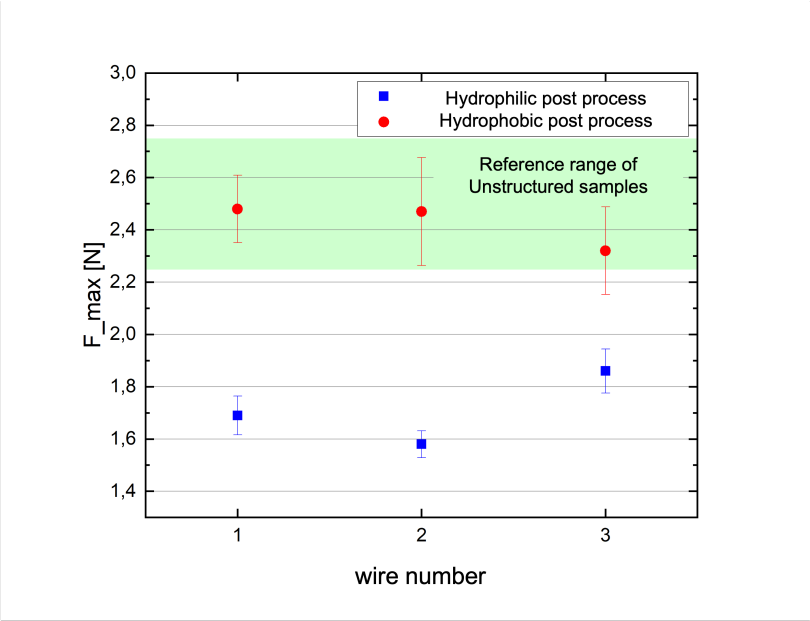

Figure 6.4: Effect of wettability to friction force

6.2 The effect of sponge-like structure on joining

In this section, the effect of sponge-like structure on the application example is discussed. As an application, multi-material joining is focused on. In recent years, multi-material joining by induction welding [79, 80] has been expected to use in the industrial field since it enables new approaches to lightweight production by using the suitable material in the right spot. It is said that the adhesion between the surfaces of multi-material joining are derived from two types of adhesion: specific adhesion, which is based on chemical and physical bonds, and mechanical adhesion, which results from the adhesive. The sponge-like structure is expected to increase mechanical adhesion when the counterpart of multi-material fills in the hole of sponge-like structure. As a counterpart of metal, fiber-reinforced thermoplastic (FRP) is chosen since it is one of the promising materials for reducing weight

and keeping mechanical strength. Therefore, in this section, the joint strength between sponge-like structured stainless steel and FRP is focused on.

There are several kinds of research about joint strength between sponge-like structured stainless steel and FRP. K.van der Streaten et al. [81] shows that sponge-like structured stainless steel plate and polyamide 6 (PA6) with glass fiber were joined and measured shear force. They have shown when the sponge-like structure is properly made, the shear strength becomes strong. On the other hand, there is some research that shows the opposite results. K.van der straeten et al. [82] made several rough surfaces including sponge-like structures by changing the scanning number of laser scan, then joined the stainless steel and the polyamide 6 (PA6) with glass fiber. They have shown that the more sponge-like structures were made on the sample, the less shear strength was between stainless steel and PA6 with glass fiber. Thus even the effect of a sponge-like structure on the joining strength is not well-known.

While it is said that it is essential to have a complete filling of the microstructures with molten polymer to achieve high joint strength. And one of the parameters for controlling the filling of the molten polymer is wettability. Regarding the effect of wettability, K.van der straeten et al. [82] studied the effect of wettability comes from physical properties, on the joint strength between stainless steel and glass fiber-reinforced plastics such as polyamide 6 (PA6) with glass fiber and polypropylene (PP) with glass fiber. In their research, they changed wettability by roughing the morphology of stainless steel but not by chemical treatment. In the results, for the joining of a combination between stainless steel and PA6, when the stainless steel surfaces were wettable, which means the surfaces were relatively smooth, the joint strengths were strong, and when the stainless surface was not wettable, which means the surface relatively rough, the joint strength between them was weak. On the other hand, the joining of a combination of stainless steel and PP still had strong joining strength for both smooth and rough surfaces. From these results, they showed that the effect of wettability which comes from roughness is low. However, up to now, the effect of wettability derived from the chemical effect of sponge-like structure on the multi-material joining is not well studied yet.

Therefore, in this study, to see the effect of sponge-like structure on the multi-material joining, non-laser processed surface and the sponge-like structure were examined. In addition, to see the effect of wettability comes from the chemical effect, the sponge-like structures with different wettability surfaces were created by different post-processing. Especially, within the wettability, the effect of the polar part of SFE is discussed. This is because in the previous section 5, post-processing can change the polar part of the SFE of the sponge-like structure without signifi-

cantly changing the dispersive part of the SFE. In addition, the polymer such as polyamide 6 (PA6) has both the polar part of surface tension and the dispersive part of surface tension [83]. Therefore, as a first study, the effect of changing the polar part of the SFE was considered. After creating a sponge-like structure on stainless steel, FRP with different plastic was jointed with an induced welding technique. Finally, the shear strengths were examined in all of the samples.

6.2.1 Experiment

Stainless steel sample

In this study, stainless steel sheets (SUS 304L, Hans-Erich Gemmel & Co. GmbH) with a dimension of 100 x 25 mm and a thickness of 1 mm were used. The dimension of the micro-structured area was 25 x 15 mm as shown in fig. 6.5.

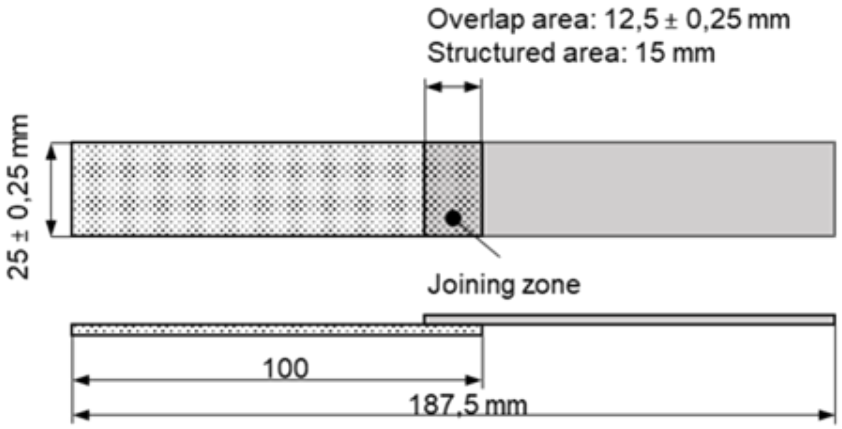

Figure 6.5: Stainless steel sample size and structured area

Laser process for stainless steel

In this study, sponge-like structures and non-laser structured surfaces (hereafter, it is called referenced surfaces) were examined. For creating sponge-like structures, the stainless steel samples were micro-structured with an experimental set up which is explained in chapter 3. To create sponge-like structure, it is need to have high peak fluence (over around 4 J/cm^2) as it shown in chapter 4. Peak fluence was set over 4 J/cm^2. Other experimental conditions to create a sponge-like structure were summarized in the tab. 6.2.

Table 6.2: Summary of structure and experimental condition and structure parameter.

parameter	value
laser power	9.6 W
pulse repetition rate	500 kHz
fluence	25.9 J/cm^2
scan speed	1000 mm/s
spatial pulse overlap	79.3 %
heat accumulation temperature (simulation)	over 6000 °C
hatching distance	5 μm
scan times	16

Topography characterization for stainless steel

The morphology and topography of the textured surfaces were studied by using an SEM and measured confocal microscope. The prepared sample's morphology and roughness (Sa) are shown in tab. 6.3. According to the tab.6.3, this sponge-like structure is a combination of bumps and holes with typical diameters of the structures of several μm and a depth or height of up to several tenths of μm. Compared to the reference surface, the sponge-like structure has relatively high roughness.

Table 6.3: Summary of structure and experimental condition and structure parameter.

	sponge-like structure	reference
SEM	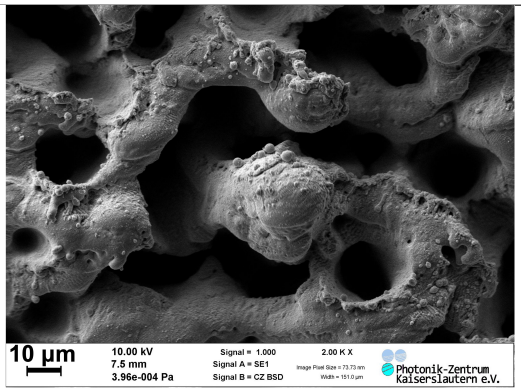	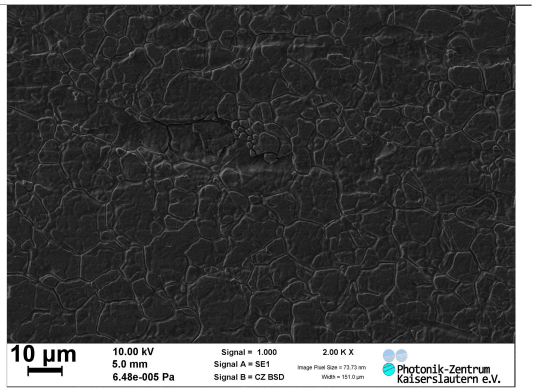
Sa	11.94 μm	0.38 μm

Post-process for stainless steel

After creating the micro-structure, all structured samples were cleaned just after the laser process with air blow and cleaned with distilled water with an ultrasonic device. After that, the samples were covered in aluminum (Al) foil to prevent contamination

in the air. For different wettability, different post-processes were conducted. For creating a hydrophobic surface, the sample was stored in the vacuum chamber of SEM for 72 days. For creating a hydrophilic surface, the sample was boiled in hot water for 8 hours. For reference surface, the post process was not conducted.

Wettability characterization for stainless steel

The wettability of the surface was measured by the Drop shape analyzer with 4 μm of distilled water. The wettabilities (the polar part of SFE of solid), which were measured by the CA for water for each post-processed sample, were shown in the tab. 6.4. According to the tab. 6.4, the CA of a sponge-like structure for the one stored in a vacuum chamber has high CA. On the other hand, the one boiled has a low CA. Therefore the same structure but a different wettability surface was created by the experiments. For reference surface, CA was $87°$. In the end, 3 types of stainless steel surface was prepared. For the further shear force test, 7 samples of each condition were created.

Table 6.4: Summary of wettability of the prepared sample

post-process	sponge-like structure
vacuum 72 hours	$143°$
boiling 8 hours	$0°$

Composite materials sample

The composite materials samples were prepared by Leibniz-Institut für Verbundwerkstoffe GmbH (IVW). In this study, 2 different glass fiber-reinforced thermoplastics composites (TP-FRPC) were joined to surface micro-structured stainless steel using discontinuous induction welding. Glass fiber-reinforced polyamide 6 (GF-PA6, semi-crystalline) and glass fiber reinforced (GF-PC, amorphous) was used. The other details of the difference of these composite materials are summarized in tab. 6.5.

Induction joining experimental setup

The stainless steel sample and the composite materials were joined by induction welding methods. Note that this induction welding experiments were conducted by IVW. The experimental setup is shown in fig. 6.6. Induction welding uses an

Table 6.5: Used TP-FRPC

name	GR-PA6	GF-PC
Manufactures	BondLaminates-Tepex Dynalite 102 RG600(4)	IVW-production
Matrix	PA6	Bayer-Makrofol DE6-2
Fabric	Twill 2/2; 600g/m^2	Twill 2/2; 600g/m^2
Thickness	2 mm	2mm
Specimen preparation	Drying: 8 h, 80°C Decreasing with isopropanol before joining	Drying: 8 h, 80°C Decreasing with isopropanol before joining

inverter in combination with an induction coil to generate an alternating electromagnetic field. This electromagnetic field induces eddy currents in an electrically conductive material, such as metal, which then heats up due to resistive losses. Additional heat is generated by magnetic hysteresis if the metal is magnetic. The electromagnetic field transmits electrical power without touching and generates heat directly in the metal. When enough power has been induced into the metal, it reaches the joining temperature which is above the melting point of the thermoplastic polymer matrix. In the molten state, the polymer wets the treated metal surface and forms the joining mechanisms after cooling. In hybrid induction welding of metals with glass-fiber reinforced thermoplastics, the TP-FRPC does not heat directly by induction, since the material is not electroconductive. If carbon fiber-reinforced polymers are welded, the fibers can be used as heating elements, since they are electrically conductive. Within a material combination, the joining parameters were not changed to determine the influences of the surface pretreatment clearly. The joining parameters are also shown in the tab. 6.6

Table 6.6: Joining parameters

name	GR-PA6/steel	GF-PC/steel
consolidation force	100 N	100 N
Generator Current	17.5 A	17.5 A
Holding time	10 s	10 s
Joining Temperature	290 °C	255°C

Shear force experiment setup

After joining the sample with induction joining, the shear strength of joining was examined by mechanical testing. Note that the shear strength of joining tests were conducted by IVW. The experimental setup for mechanical strength is shown in

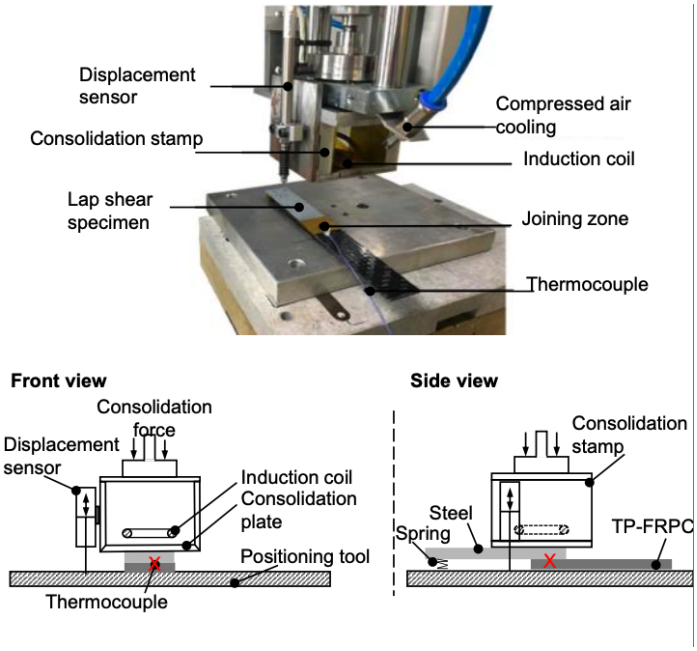

Figure 6.6: Experimental set up for induction joining: the image was taken from [79]

fig. 6.7. The joint strength was then determined by lap shear tests according to DIN 1465. The test force was measured on the crosshead and hydraulic clamping devices was used.

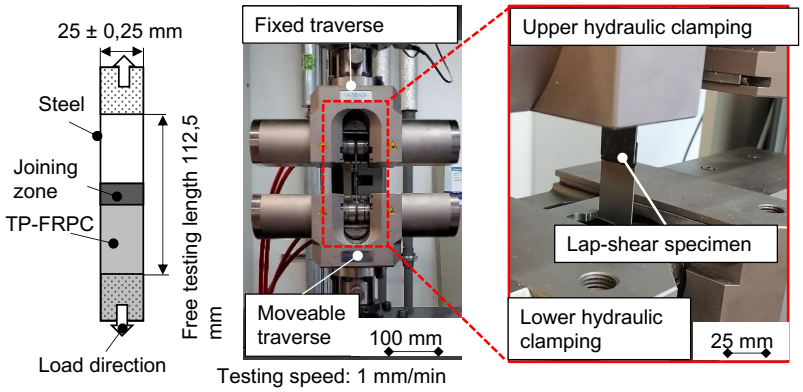

Figure 6.7: Experimental set up for shear strength test

6.2.2 Results and Discussion

Shear strength

The shear strength was measured and the results were shown in fig. 6.8. Note that this experimental results were taken by IVW.

According to fig. 6.8, at both combinations of material (GF-PC/stainless steel, GF-PA6/stainless steel), the shear strength of the sponge-like structure was improved compared to the reference surface. However, there was no influence of

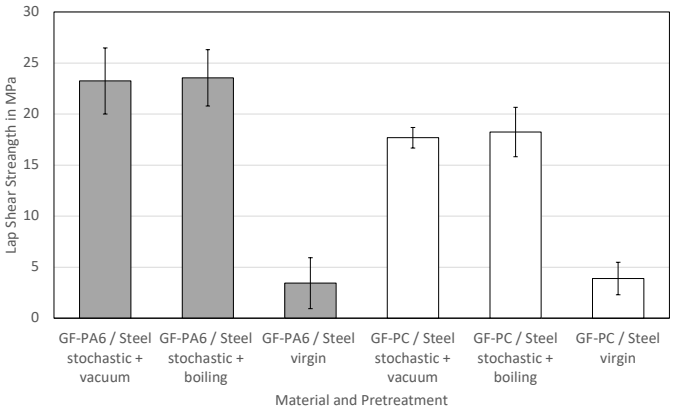

Figure 6.8: Shear strength with different setup

type of post-process	boil	vacuum
GF-PC / steel	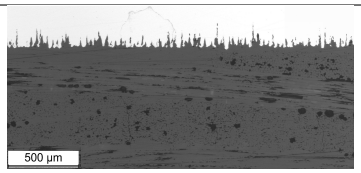	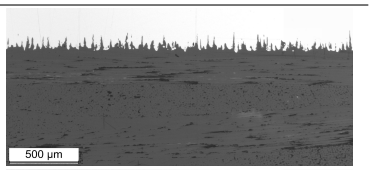
GF-PA6 / steel	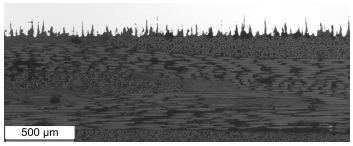	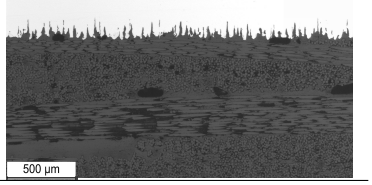

Table 6.7: Cross-section image of each joining

hydrophobic or hydrophilic effects detectable. To see the detail of the connection, the cross-section images were taken and shown in fig. 6.7. According to the 6.7, at both combinations of material (GF-PC/stainless steel, GF-PA6/stainless steel), the polymer fills the holes of the sponge-like structure. Since mechanical adhesion is one of the parameters for increasing the shear strength, this might be one of the reasons that the shear strength of the sponge-like structure was improved. In addition, there is no difference in the fill rate of polymer between the boiled one and the vacuum one, even though there is a big difference in polar part of SFE. This might be because 1.the wettability at process temperature and pressure might differ from the one at room temperature and atmospheric pressure, since how the liquid fills into the hole depends on the surface tension of the solid and the environmental pressure or 2.dispersive part of SFE is also important for glass fiber-reinforced thermoplastics composites. Therefore, as a future perspective, 1.it is need to investigate the how the wettability change by the high temperature and high pressure and 2.it is necessary to develop a post-process that allows dispersive part of SFE changes.

Chapter 7

Conclusion and Outlook

In this thesis, regarding the change of CA over time, the effect of chemical components is focused on. One of the problems is that there are few studies that can quantitatively discuss the effect of chemical components since there is few model which can predict CA from multiple chemical components. Therefore, in this study, at first, a model that can treat multiple chemicals and is usable for predicting different kinds of liquids on the laser-micro-structured surface was developed. In addition by using this model, the change of the CA over time was analyzed. Moreover, prior to this chemical effect experiments, a feature of the physical properties of laser micro-structuring is also investigated.

In chapter 2, the model that shows the relationship between CA and multiple chemical components was developed. The novelty of this model is followings.

- In order to treat multiple chemical components, the adhesive force model was expaned to treat multiple chemical components.
- In order to obtain the unknown variants (square roots of SFE($\sqrt{\sigma_{Si}^{P}}$,$\sqrt{\sigma_{Si}^{D}}$)), the variants was obtained by multiple regression analysis. The multiple regression analysis can be used because the coefficient of the polar part and dispersive part for solid (S_p and S_d) can be expressed as the linear combination of the square roots of SFE($\sqrt{\sigma_{Si}^{P}}$,$\sqrt{\sigma_{Si}^{D}}$). The coefficient of the polar part and dispersive part for solid (S_p and S_d) can be obtained by experiments.
- To conduct multiple regression analysis, several data set of the experiments (e.g. structure parameters, CA with different liquids, the ratio of chemical components by XPS) are needed.
- After having the approximated square root SFE, by having the ratio of each chemical component by XPS, the CA can be predictable.

In chapter 4, the model developed above requires several topographies and chemical surface states to know the chemical effects of time variation of CA. As a topography, the sponge-like structure is of interest because CA on sponge-like structures can be super-hydrophobic from super-hydrophilic over time. However, the boundary of the growth mechanism of sponge-like structures is not well known yet. Therefore, for aiming to create sponge-like structures on industrial applications, knowing the boundary of this growth mechanism of sponge-like structures was investigated.

In this study, in order to see the boundary of the growth mechanism of a sponge-like structure, the fluence is varied, and heat accumulation is varied by changing the time interval of pulses with the same spatial pulse overlap. According to the results, this study found followings.

- For conditions of all time intervals of pulses (25μs, 2.5μs, 1μs) when the peak fluence is small (lower than c.a.4 J/cm^2), there is no bumpy structure formed. On the other hand, in the high peak fluence range (higher than c.a.4 J/cm^2), bumpy structures were formed.

- The saturation temperatures at the conditions with the time interval of pulses of 25 μs do not exceed the critical saturation temperature for bumpy structures. However, at high peak fluence, there were sponge-like structure is occur.

- This result suggests that the growth mechanism of a bumpy structure is different at the time interval of pulses of 25 μs and at the time interval of pulses of 2.5 μs and 1 μs.

- To discuss the boundary of growth mechanism, one of the ideas of the indicator for the boundary of the growth mechanism of a sponge-like structure is to use analogies of the mechanism of incubation effect in laser-induced damage threshold. The experiments results show that the trend in the difference in the dominance of the incubation mechanism is the same as the trend in the difference of saturation temperature (below or above critical saturation temperature). Therefore, this result gives an idea that the boundary of the mechanism for bumpy structures might be predictable by the incubation model.

The results give an idea of the boundary of the heat accumulation temperature model and also give an idea of process windows for sponge-like structures.

In chapter 5, the model developed in chapter 2 is validated for several structures such as sponge-like structures and small roughness structures and reference

structures, and also different liquids. According to the results, this study found followings.

- From the results, calculated CAs were well-predicted of measured CA for all kinds of liquids (water, diiodo-methane, and ethylene-glycol). Therefore, these results show that the proposed model can be used for the prediction of CA.

The other challenge of this work is, to understand the reason for the change of CA, the long-term stability was discussed with the developed model. According to the results, this study found followings.

- From this calculation, the reason for the change of CA for laser micro-structured surface (small roughness and sponge-like) from the CA of reference surface is that the effect of chromium oxide-(Cr2O3) becomes less but the effects of carbon-(C-C(C- H)) (which include the effect of carbon-(polar) and oxygen-(metal oxide)) becomes much.
- In addition, the reason for the CA becomes high for condition (air blow - Al foil) is carbon-C-C(C-H) (which include the effect of carbon-(polar) and oxygen-(metal oxide)).
- Moreover, the reason for the CA remains low for condition (boil - Al foil) is the effect of oxygen- (layer), which includes Organic O=C-O, C- O, C-OH, and Cr2O3, is increased by boiling and remain for the long term by storing in Al foil.

In the end, the benefits of the model developed by this study include the following.

- It was shown that more detailed causes of time variation can be determined.
- Thus, the cause of time variation can be considered from the effects of multiple chemical components.
- It was shown that the model can be applied to ethylene glycol other than water and diiodomethane.
- It was shown to be applicable to other liquid and adhesive substances. Since the model deals with polar and non-polar nature of SFE, it may be useful for different metals as well.

In chapter 6, by using what I have learned in the process of conducting this research, examples of surface functionalization of real-world applications is described. The first is a study on reducing the resistance of devices (thin metal

wires) in medical devices. The reduction of frictional forces or an improvement of the sliding properties between hard metal and elastic material by means of laser micro-structuring was examined. This study showed followings.

- The dimple structures can not only be used to reduce the friction between two non-deformable surfaces, but also to reduce the friction between one solid, and non-deformable surface and one elastically deformable surface.
- For our system of a stainless steel surface and a silicone surface, the optimal friction reduction took place for a dimple diameter of 17 μm and a surface coverage of 4 %.
- Due to the elasticity of the silicone surface, the optimum aspect ratio of the dimples was found to be 0.32.
- If the steel surface had hydrophilic properties due to post-treatment, a friction reduction of 30 % could be achieved

The second is a study on increasing the bonding strength be- tween composite materials and metals. The connection of metal and other materials, such as a fiber-reinforced polymer (FRP) was examined. In this study, the stainless steel surfaces were laser micro-structured and conducted different post-processing for changing wettability. After creating stainless steel sample, FRP with different plastic was joined with an induction joining technique. And the shear stress was examined in all of the samples. This study showed followings.

- As a result, this study found that a significant effect of surface activation on the properties of the joined specimen could not be identified.
- However, a specimen that is a sponge-like structure has higher shear stress than that of the reference surface.

In this study, research was conducted with respect to the causes of time variation in CA. Future work should be based on the results of this analysis to develop how to change the chemical components on the surface.

Chapter 8

Appendix

Table 8.1: Multiple regression analysis for each conditions

(a) polar

chemical	air blow - Al foil coefficients	air blow - ambient air coefficients	boil - Al foil coefficients	boil - ambient air coefficients
Intercept	7.42	7.61	5.60	6.48
carbon-(C-C(C-H))	-22.2	-32.4	-1.71	-16.2
carbon-(polar)	-	-	-	-
oxygen-(metal oxide)	-	-	-	-
oxygen-(layer)	-	-	-	-
chromium oxide-(Cr_2O_3)	-	-	-	-

Table 8.2: Multiple regression analysis for each conditions

(a) dispersive

chemical	air blow - Al foil coefficients	air blow - ambient air coefficients	boil - Al foil coefficients	boil - ambient air coefficients
Intercept	7.42	7.90	6.67	7.60
carbon-(C-C(C-H))	-	-	-	-
carbon-(polar)	-5.41	-13.46	-	-
oxygen-(metal oxide)	-	-	1.23	-
oxygen-(layer)	-	-	-	-2.70
chromium oxide-(Cr_2O_3)	-	-	-	-

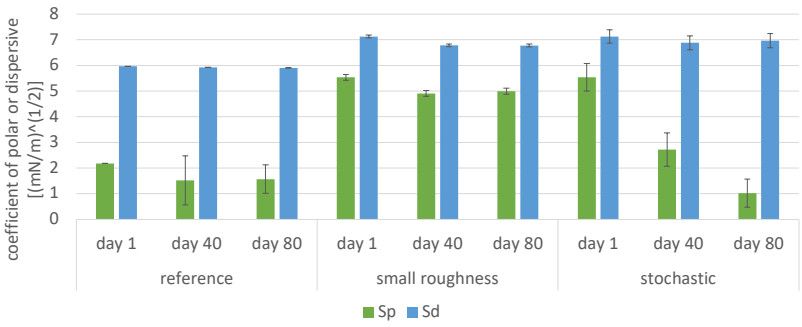

(a) air blow - Al foil

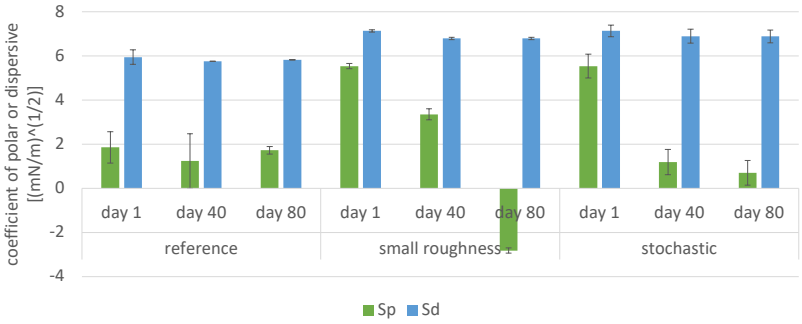

(b) air blow - ambient air

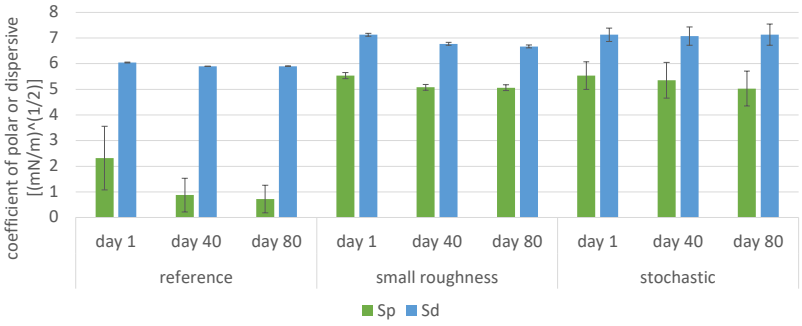

(c) boil - Al foil

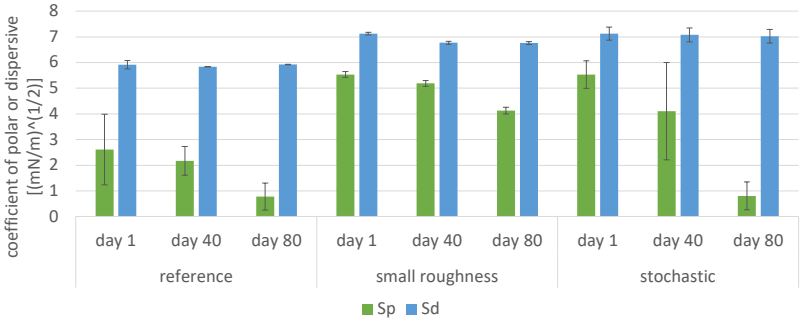

(d) boil - ambient air

Figure 8.1: S_p and S_d change over time

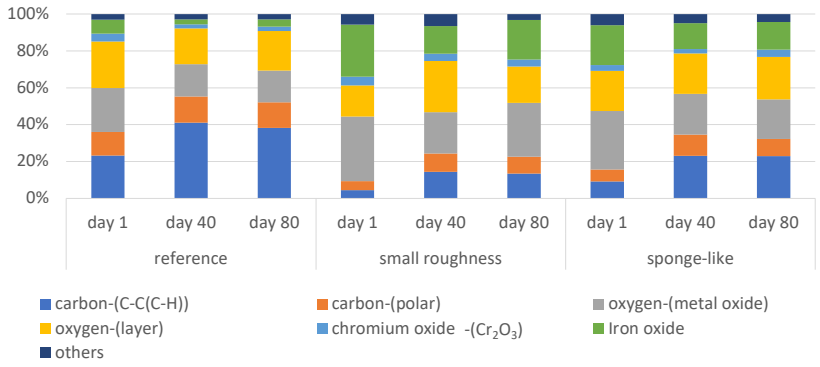

(a) air blow - Al foil

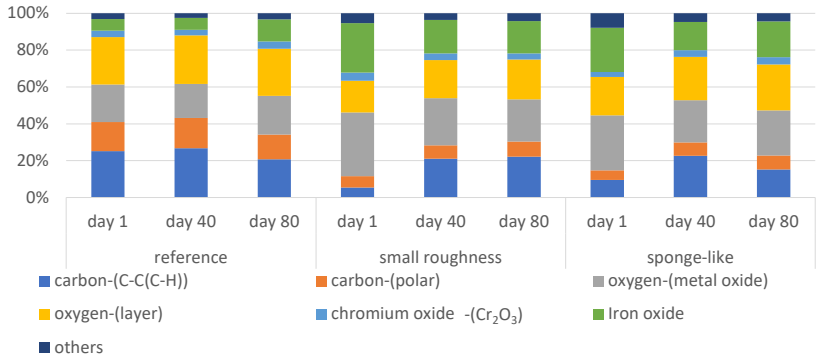

(b) air blow - ambient air

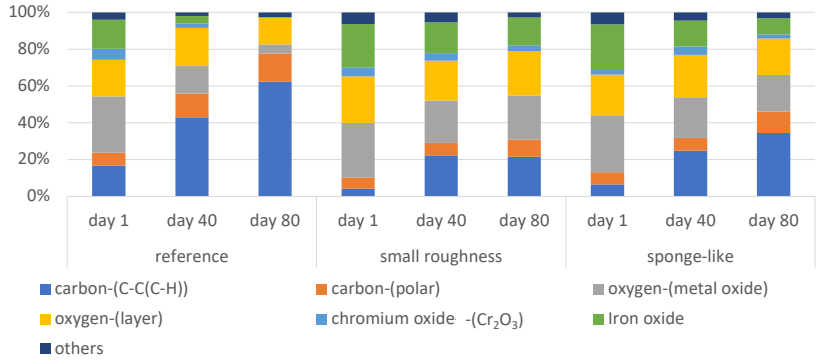

(c) boil - Al foil

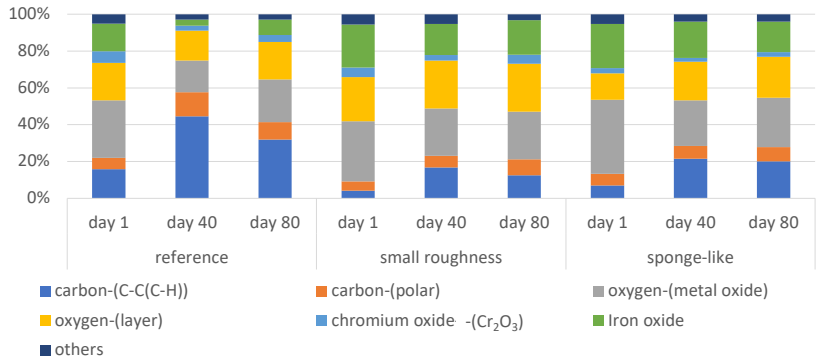

(d) boil - ambient air

Figure 8.2: XPS change over time

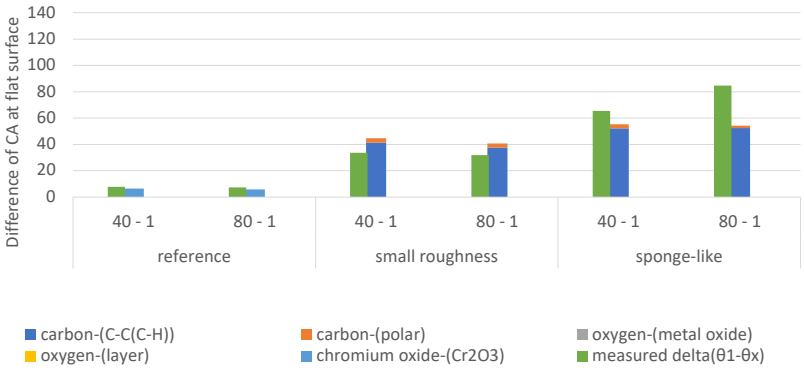

(a) air blow - Al foil

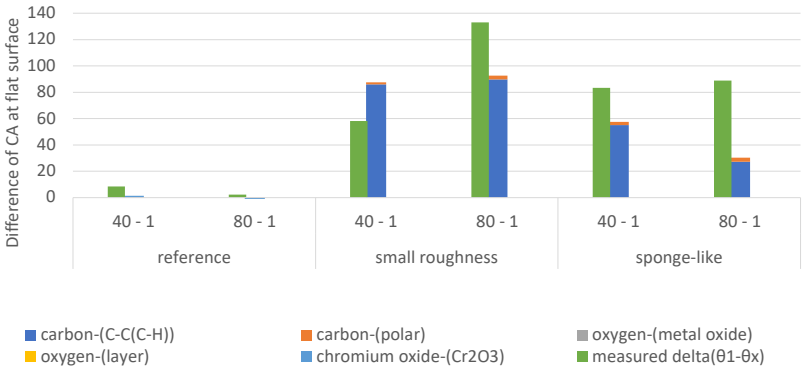

(b) air blow - ambient air

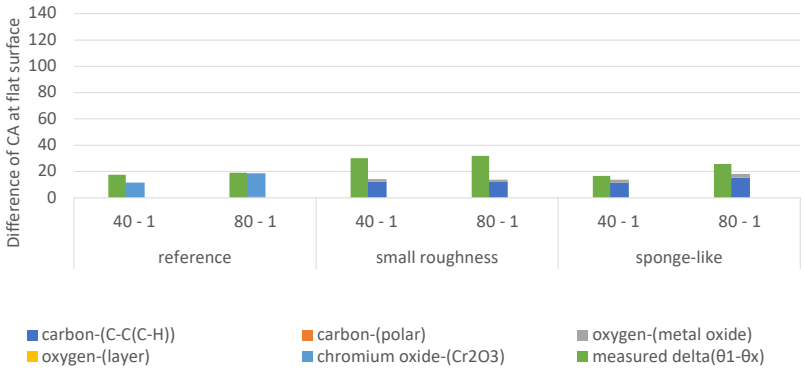

(c) boil - Al foil

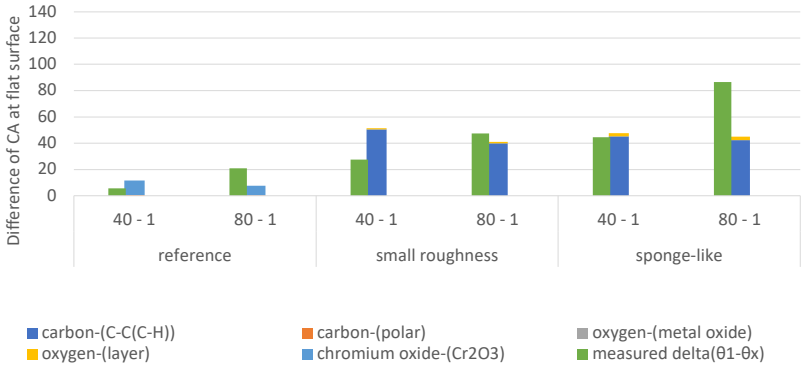

(d) boil - ambient air

Figure 8.3: CA difference at flat surface over time

Bibliography

[1] C. Florian, S. V. Kirner, J. Krüger, and J. Bonse, “Surface functionalization by laser-induced periodic surface structures,” Journal of Laser Applications, vol. 32, no. 2, p. 022063, 2020. [Online]. Available: https://doi.org/10.2351/7.0000103

[2] J. Yong, F. Chen, Q. Yang, J. Huo, and X. Hou, “Superoleophobic surfaces,” Chem. Soc. Rev., vol. 46, pp. 4168–4217, 2017. [Online]. Available: http://dx.doi.org/10.1039/C6CS00751A

[3] A.-M. Kietzig, S. G. Hatzikiriakos, and P. Englezos, “Patterned superhydrophobic metallic surfaces,” Langmuir, vol. 25, no. 8, pp. 4821–4827, 2009.

[4] Z. Yang, X. Liu, and Y. Tian, “Insights into the wettability transition of nanosecond laser ablated surface under ambient air exposure,” Journal of Colloid and Interface Science, vol. 533, pp. 268–277, Jan. 2019. [Online]. Available: https://www.sciencedirect.com/science/article/pii/S0021979718310051

[5] D.-M. Chun, C.-V. Ngo, and K.-M. Lee, “Fast fabrication of superhydrophobic metallic surface using nanosecond laser texturing and low-temperature annealing,” CIRP Annals, vol. 65, no. 1, pp. 519–522, 2016. [Online]. Available: https://www.sciencedirect.com/science/article/pii/S0007850616300191

[6] Beer, “Bestimmung der absorption des rothen lichts in farbigen flüssigkeiten,” Annalen der Physik, vol. 162, no. 5, pp. 78–88, 1852. [Online]. Available: https://onlinelibrary.wiley.com/doi/abs/10.1002/andp.18521620505

[7] B. Rethfeld, D. S. Ivanov, M. E. Garcia, and S. I. Anisimov, “Modelling ultrafast laser ablation,” Journal of Physics D: Applied Physics, vol. 50, no. 19, p. 193001, apr 2017. [Online]. Available: https://dx.doi.org/10.1088/1361-6463/50/19/193001

[8] M. E. Povarnitsyn, V. B. Fokin, and P. R. Levashov, “Microscopic and macroscopic modeling of femtosecond laser ablation of metals,” Applied

Surface Science, vol. 357, pp. 1150–1156, 2015. [Online]. Available: https://www.sciencedirect.com/science/article/pii/S0169433215022254

[9] M. E. Povarnitsyn, K. V. Khishchenko, and P. R. Levashov, "Phase transitions in femtosecond laser ablation," Applied Surface Science, vol. 255, no. 10, pp. 5120–5124, 2009, laser and Plasma in Micro- and Nano-Scale Materials Processing and Diagnostics. [Online]. Available: https://www.sciencedirect.com/science/article/pii/S0169433208018059

[10] C. Wu and L. V. Zhigilei, "Microscopic mechanisms of laser spallation and ablation of metal targets from large-scale molecular dynamics simulations," Applied Physics A, vol. 114, no. 1, pp. 11–32, 2014. [Online]. Available: https://doi.org/10.1007/s00339-013-8086-4

[11] W. J. Keller, N. Shen, A. M. Rubenchik, S. Ly, R. Negres, R. N. Raman, J.-H. Yoo, G. Guss, J. S. Stolken, M. J. Matthews, and J. D. Bude, "Physics of picosecond pulse laser ablation," Journal of Applied Physics, vol. 125, no. 8, p. 085103, 2019. [Online]. Available: https://doi.org/10.1063/1.5080628

[12] X. Li and Y. Guan, "Theoretical fundamentals of short pulse laser–metal interaction: A review," Nanotechnology and Precision Engineering, vol. 3, no. 3, pp. 105–125, 2020. [Online]. Available: https://aip.scitation.org/doi/abs/10.1016/j.npe.2020.08.001

[13] R. Fabbro, C. Max, and E. Fabre, "Planar laser-driven ablation: Effect of inhibited electron thermal conduction," The Physics of Fluids, vol. 28, no. 5, pp. 1463–1481, 1985. [Online]. Available: https://aip.scitation.org/doi/abs/10.1063/1.864982

[14] K. Eidmann, J. Meyer-ter Vehn, T. Schlegel, and S. Hüller, "Hydrodynamic simulation of subpicosecond laser interaction with solid-density matter," Phys. Rev. E, vol. 62, pp. 1202–1214, Jul 2000. [Online]. Available: https://link.aps.org/doi/10.1103/PhysRevE.62.1202

[15] P. Drude, "Zur elektronentheorie der metalle," Annalen der Physik, vol. 306, no. 3, pp. 566–613, 1900. [Online]. Available: https://onlinelibrary.wiley.com/doi/abs/10.1002/andp.19003060312

[16] S. Katayama, Handbook of Laser Welding Technologies. Woodhead Publishing, 2013.

[17] D. J. Förster, B. Jäggi, A. Michalowski, and B. Neuenschwander, "Review on experimental and theoretical investigations of ultra-short pulsed laser ablation

of metals with burst pulses," Materials, vol. 14, no. 12, 2021. [Online]. Available: https://www.mdpi.com/1996-1944/14/12/3331

[18] N. A. Inogamov, V. V. Zhakhovskii, S. I. Ashitkov, Y. V. Petrov, M. B. Agranat, S. I. Anisimov, K. Nishihara, and V. E. Fortov, "Nanospallation induced by an ultrashort laser pulse," Journal of Experimental and Theoretical Physics, vol. 107, no. 1, pp. 1–19, 2008. [Online]. Available: https://doi.org/10.1134/S1063776108070017

[19] M. Agranat, S. Anisimov, S. Ashitkov, V. Zhakhovskii, N. Inogamov, K. Nishihara, Y. Petrov, V. Fortov, and V. Khokhlov, "Dynamics of plume and crater formation after action of femtosecond laser pulse," Applied Surface Science, vol. 253, no. 15, pp. 6276–6282, 2007, proceedings of the Fifth International Conference on Photo-Excited Processes and Applications. [Online]. Available: https://www.sciencedirect.com/science/article/pii/S0169433207001547

[20] J. Hermann, E. Axente, V. Craciun, A. Taleb, and F. Pelascini, "Evaluation of pressure in a plasma produced by laser ablation of steel," Spectrochimica Acta Part B: Atomic Spectroscopy, vol. 143, pp. 63–70, 2018. [Online]. Available: https://www.sciencedirect.com/science/article/pii/S058485471730616X

[21] R. E. Russo, X. Mao, J. J. Gonzalez, V. Zorba, and J. Yoo, "Laser ablation in analytical chemistry," Analytical Chemistry, vol. 85, no. 13, pp. 6162–6177, 07 2013. [Online]. Available: https://doi.org/10.1021/ac4005327

[22] D. W. Gregg and S. J. Thomas, "Momentum transfer produced by focused laser giant pulses," Journal of Applied Physics, vol. 37, no. 7, pp. 2787–2789, 1966. [Online]. Available: https://doi.org/10.1063/1.1782123

[23] F. Bauer, A. Michalowski, T. Kiedrowski, and S. Nolte, "Heat accumulation in ultra-short pulsed scanning laser ablation of metals," Opt. Express, vol. 23, no. 2, pp. 1035–1043, Jan 2015. [Online]. Available: http://opg.optica.org/oe/abstract.cfm?URI=oe-23-2-1035

[24] K.-H. Leitz, B. Redlingshöfer, Y. Reg, A. Otto, and M. Schmidt, "Metal ablation with short and ultrashort laser pulses," Physics Procedia, vol. 12, pp. 230–238, 2011, lasers in Manufacturing 2011 - Proceedings of the Sixth International WLT Conference on Lasers in Manufacturing. [Online]. Available: https://www.sciencedirect.com/science/article/pii/S1875389211002070

[25] K. T. Ahmmed, E. J. Y. Ling, P. Servio, and A.-M. Kietzig, "Introducing a new optimization tool for femtosecond laser-induced surface texturing

on titanium, stainless steel, aluminum and copper," Optics and Lasers in Engineering, vol. 66, pp. 258–268, 2015. [Online]. Available: https://www.sciencedirect.com/science/article/pii/S0143816614002504

[26] F. Fraggelakis, G. Mincuzzi, J. Lopez, I. Manek-Hönninger, and R. Kling, "Texturing metal surface with mhz ultra-short laser pulses," Opt. Express, vol. 25, no. 15, pp. 18 131–18 139, Jul 2017. [Online]. Available: http://opg.optica.org/oe/abstract.cfm?URI=oe-25-15-18131

[27] J. Bonse, M. Munz, and H. Sturm, "Structure formation on the surface of indium phosphide irradiated by femtosecond laser pulses," Journal of Applied Physics, vol. 97, no. 1, p. 013538, 12 2004. [Online]. Available: https://doi.org/10.1063/1.1827919

[28] P. Bizi-Bandoki, S. Benayoun, S. Valette, B. Beaugiraud, and E. Audouard, "Modifications of roughness and wettability properties of metals induced by femtosecond laser treatment," Applied Surface Science, vol. 257, no. 12, pp. 5213–5218, 2011, e-MRS 2010 Spring Meeting Symposium R. "Laser Processing and Diagnostics for Micro and Nano Applications". [Online]. Available: https://www.sciencedirect.com/science/article/pii/S0169433210018180

[29] F. Nyenhuis, P. N. Terekhin, T. Menold, B. Rethfeld, A. Michalowski, and J. A. L'huillier, "Fundamentals of scanning surface structuring by ultrashort laser pulses: From electron diffusion to final morphology," Advanced Photonics Research, vol. 3, no. 9, p. 2200045, 2022. [Online]. Available: https://onlinelibrary.wiley.com/doi/abs/10.1002/adpr.202200045

[30] M. Chijiiwa, N. Berger, M. Schäfer, R. Merz, M. Kopnarski, P. Mitschang, and J. A. L'huillier, "Multiple regression analysis of the chemical components effect on wettability at ps laser micro-structured surfaces on stainless steel 304," Applied Surface Science, vol. 607, p. 154852, 2023. [Online]. Available: https://www.sciencedirect.com/science/article/pii/S0169433222023807

[31] S. Moradi, S. Kamal, P. Englezos, and S. G. Hatzikiriakos, "Femtosecond laser irradiation of metallic surfaces: effects of laser parameters on superhydrophobicity," Nanotechnology, vol. 24, no. 41, p. 415302, sep 2013. [Online]. Available: https://dx.doi.org/10.1088/0957-4484/24/41/415302

[32] C. A. Zuhlke, T. P. Anderson, and D. R. Alexander, "Formation of multiscale surface structures on nickel via above surface growth and below surface growth mechanisms using femtosecond laser pulses," Opt.

Express, vol. 21, no. 7, pp. 8460–8473, Apr 2013. [Online]. Available: http://opg.optica.org/oe/abstract.cfm?URI=oe-21-7-8460

[33] E. J. Y. Ling, J. Saïd, N. Brodusch, R. Gauvin, P. Servio, and A.-M. Kietzig, "Investigating and understanding the effects of multiple femtosecond laser scans on the surface topography of stainless steel 304 and titanium," Applied Surface Science, vol. 353, pp. 512–521, 2015. [Online]. Available: https://www.sciencedirect.com/science/article/pii/S0169433215014841

[34] S. Faas, U. Bielke, R. Weber, and T. Graf, "Prediction of the surface structures resulting from heat accumulation during processing with picosecond laser pulses at the average power of 420 w," Applied Physics A, vol. 124, no. 9, p. 612, 2018. [Online]. Available: https://doi.org/10.1007/s00339-018-2040-4

[35] K. C. Mills, Y. Su, Z. Li, and R. F. Brooks, "Equations for the calculation of the thermo-physical properties of stainless steel," ISIJ International, vol. 44, no. 10, pp. 1661–1668, 2004.

[36] [Online]. Available: https://tpds.db.aist.go.jp/tpds-web/index.aspx

[37] A. Samanta, Q. Wang, S. K. Shaw, and H. Ding, "Roles of chemistry modification for laser textured metal alloys to achieve extreme surface wetting behaviors," Materials & Design, p. 108744, 2020.

[38] K.-Y. Law, "Definitions for hydrophilicity, hydrophobicity, and superhydrophobicity: Getting the basics right," The Journal of Physical Chemistry Letters, vol. 5, no. 4, pp. 686–688, 02 2014. [Online]. Available: https://doi.org/10.1021/jz402762h

[39] S. Wang and L. Jiang, "Definition of superhydrophobic states," Advanced Materials, vol. 19, no. 21, pp. 3423–3424, 2007. [Online]. Available: https://onlinelibrary.wiley.com/doi/abs/10.1002/adma.200700934

[40] T. Young, "Iii. an essay on the cohesion of fluids," Philosophical Transactions of the Royal Society of London, vol. 95, pp. 65–87, 1805. [Online]. Available: https://royalsocietypublishing.org/doi/abs/10.1098/rstl.1805.0005

[41] C. E. Cansoy, H. Y. Erbil, O. Akar, and T. Akin, "Effect of pattern size and geometry on the use of cassie–baxter equation for superhydrophobic surfaces," Colloids and Surfaces A: Physicochemical and Engineering Aspects, vol. 386, no. 1, pp. 116–124, 2011. [Online]. Available: https://www.sciencedirect.com/science/article/pii/S0927775711004390

[42] B. Luo, P. Shum, Z. Zhou, and K. Li, “Surface geometrical model modification and contact angle prediction for the laser patterned steel surface,” Surface and Coatings Technology, vol. 205, no. 7, pp. 2597–2604, 2010. [Online]. Available: https://www.sciencedirect.com/science/article/pii/S0257897210010029

[43] M. H. Kwon, H. S. Shin, and C. N. Chu, “Fabrication of a super-hydrophobic surface on metal using laser ablation and electrodeposition,” Applied Surface Science, vol. 288, pp. 222–228, 2014. [Online]. Available: https://www.sciencedirect.com/science/article/pii/S0169433213018588

[44] R. N. Wenzel, “RESISTANCE OF SOLID SURFACES TO WETTING BY WATER,” Industrial & Engineering Chemistry, vol. 28, no. 8, pp. 988–994, Aug. 1936, publisher: American Chemical Society. [Online]. Available: https://doi.org/10.1021/ie50320a024

[45] A. B. D. Cassie and S. Baxter, “Wettability of porous surfaces,” Transactions of the Faraday Society, vol. 40, no. 0, pp. 546–551, Jan. 1944, publisher: The Royal Society of Chemistry. [Online]. Available: https://pubs.rsc.org/en/content/articlelanding/1944/tf/tf9444000546

[46] H. Hu, V. V. Swaminathan, M. R. Z. Farahani, G. Mensing, J. Yeom, M. A. Shannon, and L. Zhu, “Hierarchically structured re-entrant microstructures for superhydrophobic surfaces with extremely low hysteresis,” Journal of Micromechanics and Microengineering, vol. 24, no. 9, p. 095023, aug 2014. [Online]. Available: https://dx.doi.org/10.1088/0960-1317/24/9/095023

[47] A. Dupre and P. Dupre, Theorie mecanique de la chaleur. Gauthier-Villars Paris, 1869.

[48] D. K. Owens and R. C. Wendt, “Estimation of the surface free energy of polymers,” Journal of Applied Polymer Science, vol. 13, no. 8, pp. 1741–1747, 1969, _eprint: https://onlinelibrary.wiley.com/doi/pdf/10.1002/app.1969.070130815. [Online]. Available: https://onlinelibrary.wiley.com/doi/abs/10.1002/app.1969.070130815

[49] F. M. Fowkes, “ATTRACTIVE FORCES AT INTERFACES,” Industrial & Engineering Chemistry, vol. 56, no. 12, pp. 40–52, Dec. 1964, publisher: American Chemical Society. [Online]. Available: https://doi.org/10.1021/ie50660a008

[50] [Online]. Available: https://www.kruss-scientific.com/en/know-how/glossary/owens-wendt-rabel-and-kaelble-owrk-method

[51] Y. C. Guan, F. F. Luo, G. C. Lim, M. H. Hong, H. Y. Zheng, and B. Qi, "Fabrication of metallic surfaces with long-term superhydrophilic property using one-stop laser method," Materials & Design, vol. 78, pp. 19–24, Aug. 2015. [Online]. Available: https://www.sciencedirect.com/science/article/pii/S0261306915001971

[52] C.-V. Ngo and D.-M. Chun, "Fast wettability transition from hydrophilic to superhydrophobic laser-textured stainless steel surfaces under low-temperature annealing," Applied Surface Science, vol. 409, pp. 232–240, Jul. 2017. [Online]. Available: https://www.sciencedirect.com/science/article/pii/S016943321730689X

[53] P. Pou, J. del Val, A. Riveiro, R. Comesaña, F. Arias-González, F. Lusquiños, M. Bountinguiza, F. Quintero, and J. Pou, "Laser texturing of stainless steel under different processing atmospheres: From superhydrophilic to superhydrophobic surfaces," Applied Surface Science, vol. 475, pp. 896–905, May 2019. [Online]. Available: https://www.sciencedirect.com/science/article/pii/S0169433218335979

[54] F. H. Rajab, Z. Liu, and L. Li, "Long term superhydrophobic and hybrid superhydrophobic/superhydrophilic surfaces produced by laser surface micro/nano surface structuring," Applied Surface Science, vol. 466, pp. 808–821, Feb. 2019. [Online]. Available: https://www.sciencedirect.com/science/article/pii/S0169433218328551

[55] G. Giannuzzi, C. Gaudiuso, R. Di Mundo, L. Mirenghi, F. Fraggelakis, R. Kling, P. M. Lugarà, and A. Ancona, "Short and long term surface chemistry and wetting behaviour of stainless steel with 1D and 2D periodic structures induced by bursts of femtosecond laser pulses," Applied Surface Science, vol. 494, pp. 1055–1065, Nov. 2019. [Online]. Available: https://www.sciencedirect.com/science/article/pii/S0169433219321622

[56] C. Sciancalepore, L. Gemini, L. Romoli, and F. Bondioli, "Study of the wettability behavior of stainless steel surfaces after ultrafast laser texturing," Surface and Coatings Technology, vol. 352, pp. 370–377, Oct. 2018. [Online]. Available: https://www.sciencedirect.com/science/article/pii/S025789721830851X

[57] S. Becker, R. Merz, H. Hasse, and M. Kopnarski, "Solvent cleaning and wettability of technical steel and titanium surfaces," Adsorption Science & Technology, vol. 34, no. 4-5, pp. 261–274, Jun.

2016, publisher: SAGE Publications Ltd STM. [Online]. Available: https://doi.org/10.1177/0263617416645110

[58] A. B. D. Cassie, “Contact angles,” Discussions of the Faraday Society, vol. 3, no. 0, pp. 11–16, Jan. 1948, publisher: The Royal Society of Chemistry. [Online]. Available: https://pubs.rsc.org/en/content/articlelanding/1948/df/df9480300011

[59] [Online]. Available: https://www.gemmel-metalle.de/

[60] C.-V. Ngo and D.-M. Chun, “Control of laser-ablated aluminum surface wettability to superhydrophobic or superhydrophilic through simple heat treatment or water boiling post-processing,” Applied Surface Science, vol. 435, pp. 974–982, 2018.

[61] J. van den Brand, S. Van Gils, P. Beentjes, H. Terryn, and J. de Wit, “Ageing of aluminium oxide surfaces and their subsequent reactivity towards bonding with organic functional groups,” Applied Surface Science, vol. 235, no. 4, pp. 465–474, 2004. [Online]. Available: https://www.sciencedirect.com/science/article/pii/S0169433204005999

[62] S. D. Ann Y. Watson, M. D. Richard R. Bates, and P. D. Donald Kennedy, Eds., Air Pollution, the Automobile, and Public Health. Washington, DC: The National Academies Press, 1988. [Online]. Available: https://nap.nationalacademies.org/catalog/1033/air-pollution-the-automobile-and-public-health

[63] [Online]. Available: https://imagej.nih.gov/ij/index.html

[64] J. Moulder and J. Chastain, Handbook of X-ray Photoelectron Spectroscopy. Physical Electronics Division, Perkin-Elmer Corporation, 1992. [Online]. Available: https://books.google.de/books?id=A_XGQgAACAAJ

[65] G. Beamson, D. Briggs, and SurfaceSpectra Ltd., “The XPS of polymers database.” 2000, iSBN: 0953784843 9780953784844 Place: Manchester.

[66] C. Rulison, “Two-component surface energy characterization as a predictor of wettability and dispersability,” KRUSS Application note AN213, pp. 1–22, 2000.

[67] Z. Sun, M. Lenzner, and W. Rudolph, “Generic incubation law for laser damage and ablation thresholds,” Journal of Applied Physics, vol. 117, no. 7, p. 073102, 2015.

[68] J. M. Liu, “Simple technique for measurements of pulsed gaussian-beam spot sizes,” Opt. Lett., vol. 7, no. 5, pp. 196–198, May 1982. [Online]. Available: http://opg.optica.org/ol/abstract.cfm?URI=ol-7-5-196

[69] X. Wang, H. Zheng, Y. Wan, W. Feng, and Y. C. Lam, “Picosecond laser surface texturing of a stavax steel substrate for wettability control,” Engineering, vol. 4, no. 6, pp. 816–821, 2018. [Online]. Available: https://www.sciencedirect.com/science/article/pii/S2095809918303862

[70] C. Y. Cui, X. G. Cui, X. D. Ren, M. J. Qi, J. D. Hu, and Y. M. Wang, “Surface oxidation phenomenon and mechanism of AISI 304 stainless steel induced by Nd:YAG pulsed laser,” Applied Surface Science, vol. 305, pp. 817–824, Jun. 2014. [Online]. Available: https://www.sciencedirect.com/science/article/pii/S0169433214007880

[71] [Online]. Available: https://www.epflex.com/

[72] Z. Wang, C.-W. Wang, M. Wang, and Q.-Z. Zhao, “Manipulation of tribological properties of stainless steel by picosecond laser texturing and quenching,” Tribology International, vol. 99, pp. 14–22, 2016. [Online]. Available: https://www.sciencedirect.com/science/article/pii/S0301679X16001365

[73] I. Etsion and L. Burstein, “A model for mechanical seals with regular microsurface structure,” Tribology Transactions, vol. 39, no. 3, pp. 677–683, 1996. [Online]. Available: https://doi.org/10.1080/10402009608983582

[74] I. Etsion, Y. Kligerman, and G. Halperin, “Analytical and experimental investigation of laser-textured mechanical seal faces,” Tribology Transactions, vol. 42, no. 3, pp. 511–516, 1999. [Online]. Available: https://doi.org/10.1080/10402009908982248

[75] I. Etsion, “Improving tribological performance of mechanical components by laser surface texturing,” Tribology Letters, vol. 17, no. 4, pp. 733–737, 2004. [Online]. Available: https://doi.org/10.1007/s11249-004-8081-1

[76] C. Gachot, A. Rosenkranz, S. Hsu, and H. Costa, “A critical assessment of surface texturing for friction and wear improvement,” Wear, vol. 372-373, pp. 21–41, 2017. [Online]. Available: https://www.sciencedirect.com/science/article/pii/S0043164816307013

[77] K. Li, D. Jing, J. Hu, X. Ding, and Z. Yao, “Numerical investigation of the tribological performance of micro-dimple textured surfaces under hydrodynamic

lubrication," Beilstein journal of nanotechnology, vol. 8, no. 1, pp. 2324–2338, 2017.

[78] Friction reduction of stainless steel surfaces by laser microstructuring, Wissenschaftlichen Gesellschaft Lasertechnik und Photonik e.V. Wissenschaftlichen Gesellschaft Lasertechnik und Photonik e.V., 2021.

[79] S. Weidmann, M. Hümbert, and P. Mitschang, "Suitability of thickness change as process control parameter for induction welding of steel/tp-frpc joints," Advanced Manufacturing: Polymer & Composites Science, vol. 5, no. 2, pp. 55–68, 2019. [Online]. Available: https://doi.org/10.1080/20550340.2019.1592869

[80] S. Weidmann and P. Mitschang, "Influence of welding temperature and weathering on inductive welded hybrid joints made of steel and tp-frpc," in 22nd Symposium on Composites, ser. Key Engineering Materials, vol. 809. Trans Tech Publications Ltd, 8 2019, pp. 217–224.

[81] K. van der Straeten, I. Burkhardt, A. Olowinsky, and A. Gillner, "Laser-induced self-organizing microstructures on steel for joining with polymers," Physics Procedia, vol. 83, pp. 1137–1144, 2016, laser Assisted Net Shape Engineering 9 International Conference on Photonic Technologies Proceedings of the LANE 2016 September 19-22, 2016 Fürth, Germany. [Online]. Available: https://www.sciencedirect.com/science/article/pii/S1875389216302267

[82] K. van der Straeten, J. Sparla, A. Olowinsky, and A. Gillner, "Influence of self-organizing microstructures on the wettability of molten plastic on steel for hybrid plastic-metal joints," Welding in the World, vol. 63, no. 5, pp. 1431–1441, 2019. [Online]. Available: https://doi.org/10.1007/s40194-019-00765-6

[83] R. A. Ryntz and P. V. Yaneff, Coatings Of Polymers And Plastics. CRC Press, 2003.

Publication and conference contribution

Peer-reviewed journal paper

1. **Munehiro Chijiiwa**, Niklas Berger, Mareike Schäfer, Rolf Merz, Michael Kopnarski, Peter Mitschang, Johannes A. L'huillier, Multiple regression analysis of the chemical components effect on wettability at ps laser micro-structured surfaces on stainless steel 304, Applied Surface Science, Volume 607,2023,154852,

2. **Munehiro Chijiiwa**, Niklas Berger, Mareike Schäfer, Rolf Merz, Michael Kopnarski, Peter Mitschang, Johannes A. L'huillier, The chemical components effect of long-term contact angle change on laser micro-structured stainless steel 304, Surface & Coatings Technology, submitting.

Proceedings

1. **Munehiro Chijiiwa**,Niklas Berger, Mareike Schäfer, Peter Mitschang, Johannes A.L'huillier. The effect of temporal pulse overlaps to the morphology on stainless steel 304 at ps laser micro structuring. Lasers in Manufacturing Conference 2023,Munich, Germany, 2023

2. F. Sha, S. Liu, **M. Chijiiwa**, J.A. L'huillier, K. Fushinobu. Numerical study on ultrashort pulse laser processing of transparent material, ISTP32, Proc. ISTP32, Mar. 2022.

3. **Munehiro Chijiiwa**,Niklas Berger, Mareike Schäfer, Rolf Merz, Michael Kopnarski, Peter Mitschang, Johannes A. L'huillier, The effect of chemical components on wettability at ps laser micromachined surface on stainless steel 304, Lasers in Manufacturing Conference 2021, Munich, Germany, 2021

4. Niklas Berger, Benjamin Keim, **Munehiro Chijiiwa**, Hicham Derouach, Senta Schauer, Mareike Schäfer, Johannes A.L'huillier, Friction reduction of stain-

less steel surfaces by laser microstructuring, Lasers in Manufacturing Conference 2021,Munich, Germany, 2021

Review contribution

1. Asato Tamura, Takahiko Komorizono, Shota Kobashigawa, Kazuyoshi Fushinobu, ”Transfer characteristics for laser-induced forward transfer of stainless steel particle,” Opt. Eng. 61(7) 074104 (27 July 2022)

Supervised Theses

1. Niklas, Berger, Erzeugung reibungsreduzierender Mikrostrukturen auf Stahl mit Hilfe von UKP- Lasern für Anwendungen in der Medizin, Diploma thesis, Depertment of Technischer Physik, TU Kaiserslautern, 2020

Previous peer-reviewed journal paper

1. D.H. Doan, **M. Chijiiwa**, K. Fushinobu, K. Okazaki. “Investigation on the interaction among light, material and temperature Field in the transient lens effect, Propagation characteristics in 2D temperature field”, Thermal Science and Engineering,Vol. 19, No. 2, pp. 43-50, 2011

Previous proceedings

1. **M. Chijiiwa**, K. Fushinobu, K. Okazaki. “FDTD analysis of ultra short pulse laser propagation in transient lens effect part2”, AJTEC2011, Proc. AJTEC2011, Mar. 2011.

2. D.H. Doan, **M. Chijiiwa**, K. Fushinobu, K. Okazaki. “Investigation on the interaction among light, material and temperature field in the transient lens effect, Propagation characteristics in 2D temperature field”, The 47th National Heat Transfer Symposium, pp. 403-404, May. 2010.

3. **M. Chijiiwa**, K. Fushinobu, K. Okazaki. “FDTD analysis of ultra short pulse laser propagation in transient lens effect part1”, The 47th National Heat Transfer Symposium, pp. 405-406, May. 2010.

4. D.H. Doan, **M. Chijiiwa**, K.Yamazaki, K. Fushinobu, K. Okazaki. “Investigation on the interaction among light, material and temperature field in the transient lens effect part2”, The 46th National Heat Transfer Symposium Vol. 2, pp. 487-488, Jun. 2009.

5. **M. Chijiiwa**, K.Yamazaki, K. Fushinobu, K. Okazaki. “Investigation on the interaction among light, material and temperature field in the transient lens effect part1”, The 45th National Heat Transfer Symposium, Vol. 1, pp. 377-378, May. 2008.

Previous patent

1. **M.Chijiiwa**, Y.Fukumiya, A.Maeda, 2015. “Laser processing and substrate production method”, JP Patent P2015-96272A, filed November 15, 2013, and issued May 21,2015

2. A.Watanabe, **M.Chijiiwa**, “Laser processing of silicon wafer and production method of Ink jet head” (JP Patent pending)

3. D.H.Doan, K.Fushinobu, M.Tokushige, K.Yamazaki, **M.Chijiiwa**, Y.Akamine. 2012. “Fluidic optics and Laser source and Laser process machine”, JP Patent P2012-141515A, filed January 5, 2011, and issued July 26,2012

Curriculum Vitae

Personal Data

Name	Munehiro Chijiiwa
Nationality	Japanese

Education

11/2018-	PhD candidate in TU Kaiserslautern, Germany
04/2008-04/2011	Master of Mechanical Engineering, Tokyo Institute of Technology, Japan
09/2008-08/2009	Exchange program, KTH Royal Institute of Technology, Sweden
04/2004-03/2008	Bachelor of Engineering, Tokyo Institute of Technology, Japan

Work Experience

11/2018-	Photonik-Zentrum Kaiserslautern e.V., Kaiserslautern, Germany
04/2011-01/2018	Canon.Inc, Tokyo, Japan